UNIVERSITÀ DEGLI STUDI DI CATANIA

International PhD in Chemical Sciences - Cycle XXVIII

Salvatrice Millesi

Assembly of Functional Nanostructures for Optical, Electrical or Catalytic Systems

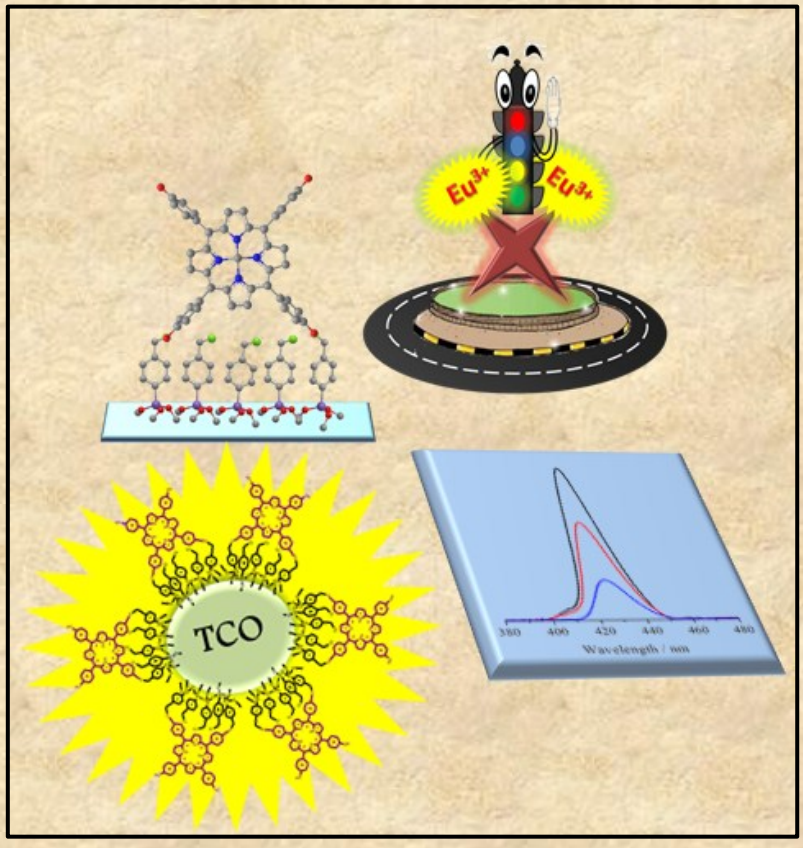

Tutor :
Prof. Antonino Gulino
Coordinator:
Prof. Salvatore Sortino

PhD Thesis

UNIVERSITÀ DEGLI STUDI DI CATANIA

International PhD in Chemical Sciences - Cycle XXVIII

Salvatrice Millesi

Assembly of Functional Nanostructures for Optical, Electrical or Catalytic Systems

Tutor :
Prof. Antonino Gulino
Coordinator:
Prof. Salvatore Sortino

PhD Thesis

A Niki,

ad Anita.

Le donne che hanno cambiato il mondo
non hanno mai avuto bisogno di mostrare nulla,
se non la loro intelligenza.

Rita Levi Montalcini

Contents

Preface

The aim of this PhD thesis is the fabrication and study of nanostructures showing optical, electrical or catalytic properties in the perspective of applications in different fields of the nanotechnology. An important aspect is represented by the method we used to manufacture these nanostructures. In fact, all synthesized systems are based on the covalent assembly of discrete molecules (organic molecules or inorganic complexes) on inorganic surfaces. The present molecules (building blocks) show interesting properties e.g. optical or catalytic activity, while the substrate materials are appropriate for applications of the final structures in the optoelectronic, microelectronic or catalytic industries.

Often, by changing just the inorganic substrate the same covalently assembled building blocks exhibit different properties and this is an evidence of the fact that single-molecules properties can be affected by the substrate nature upon anchoring. For example, anchoring of optically active molecules such as porphyrins to Si(100) substrates allows to exploit optoelectronic properties while the same porphyrin molecules on SnO_2 and TiO_2 nanocrystals provide electron injection on the semiconducting surfaces useful for photovoltaics.

Moreover, we also investigated optical active surfaces upon the self-assembly of porphyrin molecules functionalised with luminescent Eu(III) complexes in order to exploit the mutual interaction of systems whose luminescence is based on different mechanisms. In the same context, we functionalised a covalent polystirene film on a quartz substrates with an Eu(III) complex to examine the possibility to obtain tunable light emitting properties useful to transfer optical information.

The covalent assembly of porphyrins and Eu(III) complexes can be applied also to electroactive substrates as CdO, ITO, ZnO, etc. in the perspective of microelectronic applications. For this reason we optimized the deposition of high conducting CdO thin films by a metallorganic chemical vapour deposition route.

Finally, we studied the activity of some (salen)Mn(III) molecules covalently assembled on glass beads in the epoxidation of unfunctionalised prochiral olefins with the aim of increasing the catalytic behaviour upon heterogeneization thus obtaining huge turnover numbers.

In summary the most important achievement of this thesis is to have demonstrated that the covalent assembly of suitable molecules on appropriate inorganic surfaces allows the synthesis of molecular architectures showing unique properties appealing for future technologies.

Chapter 1

Nanotechnology and Nanomaterials

Nanotechnology refers to the research and technology development at atomic, molecular and macromolecular scales, which leads to the controlled manipulation and study of structures and devices with length scales in the range of 1-100 nanometers (nanostructures). In the last two decades, the research of nanotechnology has grown explosively thanks to the possibility to observe phenomena by far different than those observable studying similar systems of larger dimensions.[1] In fact, nanostructured materials show properties of exceptional interest such as unique architectures, tailored physicochemical characteristics, central roles in fabricating nanoelectronics, potential applications in bionanotechnology, etc. In recent years, a vast array of novel nanostructures has been manufactured and studied in the interdisciplinary fields of nanoscience, material science, biological science, etc..[2]

Nanodevices can be synthesized through two main approaches. The *top-down* method involves the construction of nanostructures starting from the miniaturization of macroscopic materials. These are generally based on lithography in which a scheme previously drawn is significantly shrunken and reported on the matrix of interest. Examples of such methodology are the fabrication of integrated circuits and the ion implantation.[3] Otherwise, the *bottom-up* approach involves the synthesis of nanomaterials and nanoobjects, using atoms and/or molecules as "molecular building blocks", which are assembled together by weak interactions (self-assembly).[4-7]

Actually the *bottom-up* approach appears to be the most promising for the fabrication of hybrid inorganic /organic systems constituted from organic molecules covalently bound to inorganic substrates such as silicon, quartz, metals and metal oxides.[8-9]

As a consequence, in this thesis it has been chosen to use the *bottom-up* method to anchor molecules on inorganic substrates (Si(100), quartz, glass beads, SnO_2, TiO_2).

1.1 Self-Assembled Monolayers (SAMs)

The self-assembly is a chemical process in which molecular systems self-assemble, that is form ordered structures. It has attracted significant attention since its introduction in 1980 by Sagiv.[10] Self-assembled monolayers (SAMs) are convenient and simple systems useful to tailor the interfacial properties of metals, metal oxides, and semiconductors. They are assemblies formed by the adsorption of molecular constituents from solution or gas phase onto solid surfaces or in regular arrays on the surface of liquids. Molecules that form SAMs have chemical functionalities, or "headgroups", with a specific affinity for the substrate surface and, once adsorbed, organize spontaneously in ordered structures (Figure 1.1).[11]

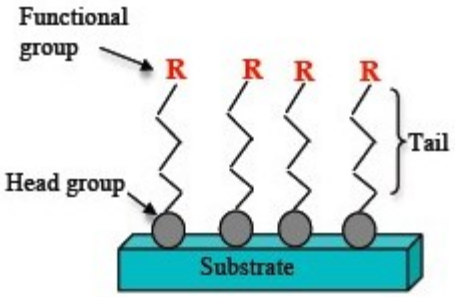

Figure 1.1. Representation of a SAM structure.

An important aspect of the SAM is that the structure and properties of assemblies are neither easily controlled nor governed by self-evident set of rules since they are governed from weak interactions such as π–π stacking, electrostatic, dipole–dipole or Van der Waals interactions, and other more complex forces.[12] Fabrication of SAMs with a controlled surface chemistry, high molecular organization and defined stoichiometry over relatively large areas have facilitated the study of molecular and cellular interactions, surface energetic, surface charge, or other interface properties. For example, SAMs can be used to obtain information on biological mechanisms such

as cell signalling, cell adhesion, protein interactions and to build molecular biosensors, etc..[13-14] Moreover, the ability to grow ordered organic materials directly on appropriate substrates has permitted their integration into semiconductor-based technologies[15] and electronic devices.[16]

1.2 Functionalization of Substrates

One of the techniques to create mono- or multilayers on surfaces is the Langmuir-Blodgett process.[17] In this method amphiphilic molecules, composed of a hydrophobic TAIL and a hydrophilic HEAD-GROUP, are dissolved in an easily evaporating solvent and placed at the air-water interphase (subphase). After solvent evaporation and upon compression of movable barriers, molecules interact each other and form a monolayer at the aqueous interface that causes a decrease of the surface tension at the subphase. This monolayer, if compressed to a chosen surface pressure, can be transferred onto an solid substrate (hydrophobic or hydrophilic) by immersing (or emersion) the solid substrate into (or from) the liquid (Figure 1.2). Depending on the nature of the used substrate, molecules orient differently on the solid surface. Performing the same procedure it is possible to transfer more monolayers onto the same solid surface. The transfer of successive layers does not depend on substrate-molecule interactions but on interactions between hydrophobic and hydrophilic parts of the amphiphile.

Despite the Langmuir-Blodgett technique allows to obtain easily monolayers on solid substrate, the final system could be not stable. In fact, molecules are bound to the substrate by means of weak electrostatic interactions easily destructible under the effect of mechanical action or by the dissolution in a solvent with greater affinity for the monolayer. As a consequence, nowadays different immobilization approaches exist to anchor covalently molecules to solid surfaces that can be planar or curved (nanoparticles).

Many surfaces can be used as substrates to fabricate monolayers and about a half of the published papers on this subject deals with thiol headgroups anchored to noble metals (Au, Pt, Pd) (Figure 1.3).

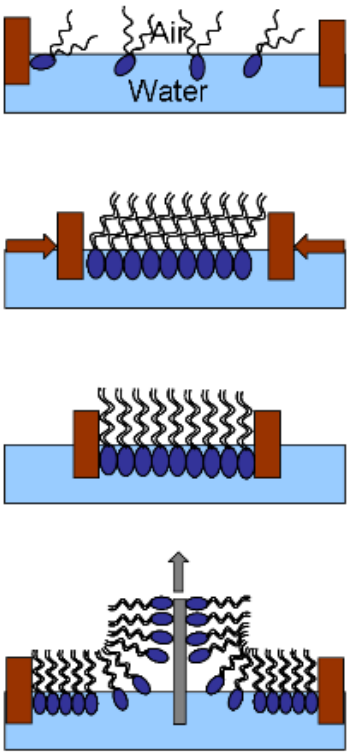

Figure 1.2. Schematic representation of the Langmuir-Blodgett technique.

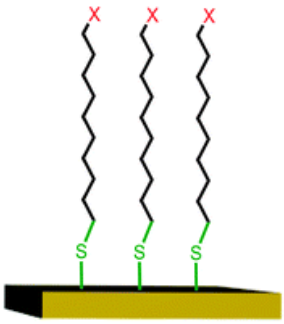

Figure 1.3. SAMs of alkanethiolates on Au. X= terminal functional group.

Despite the importance of the concerned theoretical aspects, these systems are of little practical application because of the poor temporal stability of the related metal–S bond.

One class of molecules, which attracted significant attention during the past decades, are silanes self-assembled on hydroxyl terminated substrates, e.g. silicon,

ITO, glass etc.. These systems are physically and chemically robust and can be applied in various fields of technology, e.g., electronics, sensors, optic, and others.

Excellent substrates to fabricate, through covalent bonding, mono- and multilayers are high purity crystal silicon surfaces, commercially available and relatively inexpensive due to their wide use in microelectronics. Upon exposure to air, single crystal silicon becomes rapidly coated with a thin, native oxide that can be chemically removed with HF or thermally under UHV conditions. In this thesis, substrates chosen are represented by Si(100), high quality fused silica (quartz), glass beads, and conducting metal oxides such as ITO (Sn-doped In_2O_3),[18] CdO, TiO_2, SnO_2.

Specifically, it was chosen to functionalize Si(100), high quality silica fused (quartz) and glass bead substrates with a covalent 4-$ClCH_2C_6H_4SiCl_3$ coupling agent (CA) that binds to the surface using the $–SiCl_3$ group and leaves a $–CH_2Cl$ group unreacted (Figure 1.4).[19-20]

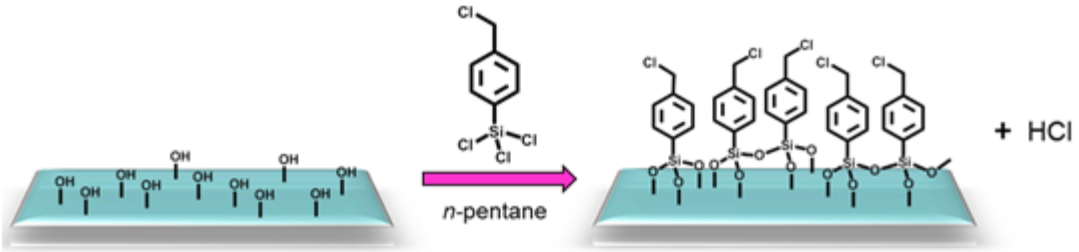

Figure 1. 4 Reaction between the coupling agent 4-$ClCH_2C_6H_4SiCl_3$ and the hydroxilated substrate surface. The unreacted $–CH_2Cl$ group allows a further functionalization.

Si(100) substrates, 2 x 0.8 cm, were first cleaned with "piranha" solution (conc. H_2SO_4 : 35% H_2O_2 70 : 30 v/v) at room temperature for 10 min, rinsed in double distilled water for 4 min, etched in 2.5% hydrofluoric acid for 100 s, washed with double distilled water and accurately dried with pre-purified N_2. Subsequently, they were treated for 5 min with ozone using an Ozon-Generator (Fisher 500) system in order to obtain a SiO_2 thin (about 10 Å) layer.[21-22] Freshly cleaned substrates were transferred to a glove box (system with a N_2 controlled atmosphere where H_2O and O_2 levels are less than 1ppm) and immersed, at room temperature for 20 min, in a 0.5 : 100 (v/v) n-pentane solution of 4-$ClCH_2C_6H_4SiCl_3$ silane to afford a monolayer of this

coupling agent. Subsequently, the chlorobenzyl-functionalised substrates were washed and sonicated in n-pentane for 10 min to remove any physisorbed CA.

A similar procedure was performed with quartz substrates which after treatment with "piranha" solution were immersed in a H_2O : 30% H_2O_2 : NH_3, 5 : 1 : 1 v/v/v solution at room temperature for 1 h.[23-24] Then after washing in double distilled water they underwent the previous glove box treatment.

In both cases the obtained structures are more stable than those obtained using alcanethiolate as coupling agent on metals surfaces. In fact, they strongly adhere to the substrates and it is not possible to remove them neither with prolonged sonication while heating in organic solvents nor using the Scotch-tape decohesion test.[25]

1.3 Properties of SAMs

SAM_S are often used for the development of memory devices, sensors, switches and, in general, as stimuli-responsive materials (SRMs). SRMs ideally undergo reversible changes in one or more properties (structure, phase morphology, electrical, magnetic and mechanical response, etc.) upon application/removal of an external stimulus, such as a change in temperature, ionic strength, pH, electric, magnetic or mechanical fields or by chemical, optical, or biological analytes (Figure 1.5). Such materials have potential smart applications in sensors, actuators, electro-optic devices, etc.. As a consequence, the control of molecular structure and dynamics is of major importance from the perspective of designing SRM-based devices. The combination of optically responsive materials and monolayer assembly is a rapidly emerging field because these materials are inexpensive, miniature, robust and easy to fabricate.[26]

A large variety of assemblies has been reported. As an example, diazonium salts have been used as coupling agents as initiators for surface-confined photopolymerization reactions.[27-28] Other systems have been based on silane-based chemistry or on metal–ligand coordination, where stimuli responsive molecules have been used as sensors for information processing, to generate assemblies that behave according to various logic schemes for molecular logics.

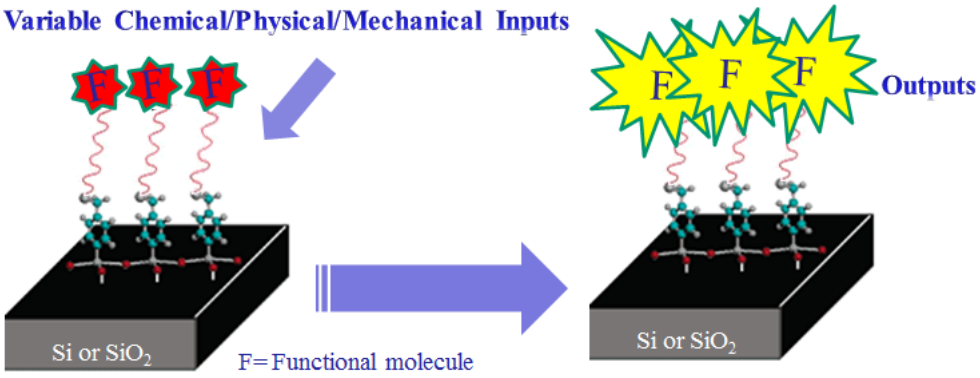

Figure 1.5. Schematic representation of Stimuli Responsive Materials (SRMs). The functional molecule (F) depending on particular stimuli (inputs) changes its properties giving measurable responses (outputs).

E. g., M. E. van der Boom and co-workers reported on a highly ordered molecular nanostructure, based on Os or Ru polypyridyl complexes of the type $[Os(bpy)_2(mbpy\text{-}py)][(PF_6)_2]$, covalently anchored to both quartz and ITO substrates (Figure 1.6) and useful to generate various logic gates.[29-30]

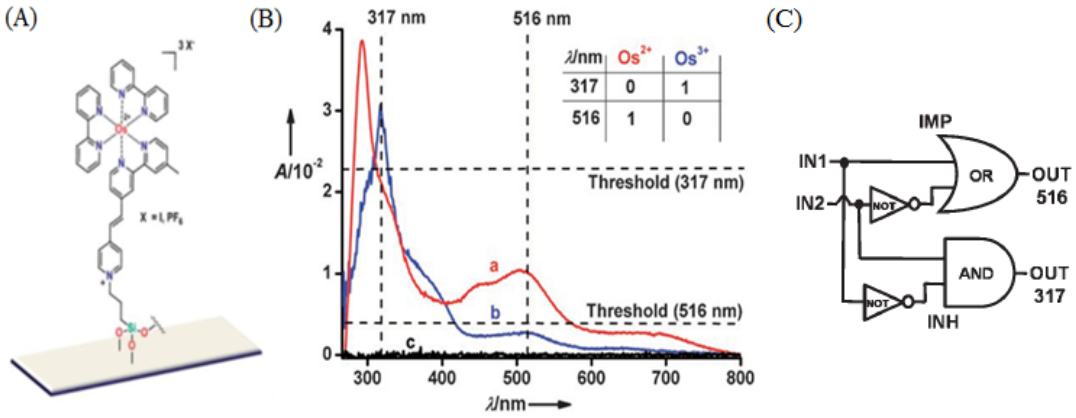

Figure 1.6. (A) Osmium complex object of study. (B) Representative absorption spectra of Os^{2+}/Os^{3+}-based monolayers: a) Os^{2+}, red line; b) Os^{3+}, blue line; c) baseline, black line. The absorption intensities at λ=317 and 516 nm were used as output. Inset: Truth table for the Boolean logic function upon the wavelength and metal oxidation state. (C) Logic circuit related to Os^{2+}/Os^{3+}system operating with two inputs (IN).

In addition to inorganic compounds, even largely flexible molecules as fullerenes, porphyrins, polymers, etc. covalently anchored to silicon or other conducting

substrates, can be pursued to build molecularly based responsive materials in the perspective of fabricating opto-electronic devices.[31] For instance it has been reported on the ability of fullerene monolayers covalently bound to functionalised SiO_2 substrates to act as photoluminescence sensor to oxygen.[32]

In this thesis porphyrins, metalloporphyrins, Eu(III) complexes, polymers such as polystyrene and (salen)Mn(III) molecules were used to fabricate nanostructured systems and investigate their stimuli responsive properties.

References

[1] J. Gao, B. Xu, *Nano Today*, **2009**, *4*, 37-51.

[2] a) C. Bae, H. Yoo, S. Kim, K. Lee, J. Kim, M. M. Sung, H. Shin, *Chem. Mater.* **2008**, *20*, 756–767. b) G. R. Patzke, F. Krumeich, R. Nesper, *Angew. Chem., Int. Ed.,* **2002**, *41*, 2446–2461. c) S. J. Hurst, E. K. Payne, L. Qin, C. A. Mirkin, *Angew. Chem., Int. Ed.* **2006**, *45*, 2672–2692. d) B. Tian, T. J. Kempa, C. M. Lieber, *Chem. Soc. Rev.*, **2009**, *38*, 16–24.

[3] de Ruiter, G.; van der Boom, M. E. *Acc. Chem. Res*. **2011**, *44*, 563-573.

[4] Mahouche-Chergui, S.; Gam-Derouich, S.; Mangeney, C.; Chehimi, M. M *Chem. Soc. Rev*. **2011**, *40*, 4143–4166.

[5] (a)Orski, S. V.; Poloukhtine, A. A.; Arumugam, S.; Mao, L.; Popik, V. V.; Locklin, J.; *J. Am. Chem. Soc*. **2010**, *132*, 11024–11026; (b) Palomaki, P. K. B.; Dinolfo, P. H. *Langmuir* **2010**, *26*, 9677–9685; (c) Lupo, F.; Gentile, S.; Ballistreri, F. P.; Tomaselli, G. A.; Fragalà, M. E.; Gulino, A. *Analyst*, **2010**, *135*, 2273-2279; (d) Chen, R.; Zhu, S.; Maclaughlin, S. *Langmuir* **2008,** *24*, 6889-6896; (e) Shi, F. N.; Cunha-Silva, L.; Sá Ferreira, R. A.; Mafra, L.; Trindade, T.; Carlos, L. D.; Almeida Paz, F. A.; Rocha, J. *J. Am. Chem. Soc*. **2008**, *130*, 150; (f) Massue, J.; Quinn, S. J.; Gunnlaugsson, T. *J. Am. Chem. Soc*. **2008**, *130*, 6900; (g) Yan, B.; Lu, H.-F. *Inorg. Chem*. **2008**, *47*, 5601; (h) Su, Y.; Li, L.; Li, G. *Chem. Commun*. **2008**, 4004; Altman, M.; Zenkina, O.; Evmenenko, G.; Dutta, P.; van der Boom, M. E. *J. Am. Chem. Soc*. **2008**, *130*, 5040.

[6] Gomar-Nadal, E.; Puigmarti-Luis, J.; Amabilino, D.B.; *Chem. Soc. Rev*. **2008**, *37*, 490-504.

[7] Crivillers, N.; Mas-Torrent. M.; Perruchas. S.; Roques, N.; Vidal-Gancedo, J.; Veciana, J.; Rovira, C.;Basabe-Desmonts, L.; Ravoo, B. J.; Crego-Calama, M.; Reinhoudt, D.N. *Angew. Chem. Int. Ed*. **2007**, *46*, 2215-2219.

[8] Mannini, M.; Pineider, F.; Danieli, C.; Totti, F.; Sorace, L.; Sainctavit, P.; Arrio, M. A.; Otero, E.; Joly, L.; Cezar, J. C.; Cornia, A.; Sessoli, R. *Nature* **2010**, *468*, 417-421.

[9] Wachowiak, A.; Yamachika, R.; Khoo, K. H.; Wang, Y.; Grobis, M.; Lee, D.-H.; Louie, S. G.; Cromie, M. F. *Science* **2005**, *310*, 468-470.

[10] J. Sagiv, *J. Am. Chem. Soc.*, **1980**, *102*, 92–98.

[11] J. C. Love, L. A. Estroff, J. K. Kriebel, R. G. Nuzzo, G. M. Whitesides, *Chem. Rev.* **2005**, *105*, 1103-1169.

[12] Shi, Y.; Zhang, C.; Zhang, H.; Bechtel, J. H.; Dalton, L. R.; Robinson, B. H.; Steier, W. H. *Science* **2000**, *288*, 119-122.

[13] Ciampi, S.; James, M.; Le Saux, G.; Gaus, K.; Justin, G.J. *J. Am. Chem. Soc.* **2012**, *134*, 844-847.

[14] J. J. Gooding, F. Mearns, W. Yang, J. Liu, *Electroanal.*, **2003**, *15*, 81-96.

[15] (a) Kim, C.; Facchetti, A.; Marks, T. J. *Science* **2007**, *318*, 76–80. (b) Burtman, V.; Hukic, G.; Ndobe, A. S.; Drori, T.; Vardeny, Z. V. *J. Appl. Phys.* **2007**, *101*, 054502–054507.

[16] Q. Y. Sun, L. C. P. M. de Smet, B. van Lagen, M. Giesbers, P. C. Thuene, J. van Engelenburg, F. A. de Wolf, H. Zuilhof, E. J. R. Sudhoelter, *J. Am. Chem. Soc.*, **2005**, *127*, 2514.

[17] Chen, X.; Lenhert, S.; Hirtz, M.; Lu, N.; Fuchs, H.; Chi, L. *Acc. Chem. Res., **2007**, 40*, 393–401.

[18] A. Gulino. *Anal Bioanal Chem.* **2013**, *405*, 1479–1495.

[19] S. L. Brandow, M. S. Chen, C. S. Dulcey, W. J. Dressick, *Langmuir*, **2008**, *24*, 3888.

[20] W. Lin, W. Lin, G. K. Wong and T. J. Marks, *J. Am. Chem. Soc.*, **1996**, *118*, 8034.

[21] A. Gulino, F. Lupo, M. E. Fragalà, S. L. Schiavo, *J. Phys. Chem. C*, **2009**, *113*, 13558.

[22] F. Lupo, M. E. Fragalà, T. Gupta, A. Mamo, A. Aureliano, M. Bettinelli, A. Speghini, A. Gulino, *J. Phys. Chem. C*, **2010**, *114*, 13459.

[23] A. Facchetti, L. Beverina, M. E. van der Boom, P. Dutta, G. Evmenenko, A. D. Shukla, C. E. Stern, G. A. Pagani, T. J. Marks, *J. Am. Chem. Soc*. **2006**, *128*, 2142.

[24] (a) R. Yerushalmi, A. Scherz, M. E. van der Boom,. *J. Am. Chem. Soc*. **2004**, *126*, 2700. (b) C. Haensch, S. Hoeppener, U. S. Schubert, *Chem. Soc. Rev.*, **2010**, *39*, 2323.

[25] A. D. Shukla, A. Das, M. E. van der Boom, *Angew. Chem., Int. Ed.*, **2005**, *44*, 3237.

[26] (a) G. Wen, J. Yan, Y. Zhou, D. Zhang, L. Mao, D. Zhu, *Chem. Commun.*, **2006**, 3016; (b) A. M. Moore, A. A. Dameron, B. A. Mantooth, R. K. Smith, D. J. Fuchs, J. W. Ciszek, F. Maya,Y. Yao, J. M. Tour, P. S. Weiss, *J. Am. Chem. Soc.*, **2006**, *128*, 1959; (c) P. A. Lewis, C. E. Inman, F. Maya, J. M. Tour, J. E. Hutchison, P. S. Weiss, *J. Am. Chem. Soc.*, **2005**, *127*, 17421; (d) Y. Liu, L. Mu, B. Liu, J. Kong, *Chem. Eur. J.*, **2005**, *11*, 2622; (e) Y. S. Chi, S. Hwang, B. S. Lee, J. Kwak, I. S. Choi, S.-g. Lee, *Langmuir*, **2005**, *21*, 4268; (f) K. Critchley, J. P. Jeyadevan, H. Fukushima, M. Ishida,

T. Shimoda, R. J. Bushby, S. D. Evans, *Langmuir*, **2005**, *21*, 4554; (g) S. Jiang, M. Liu, *Chem. Mater.*, **2004**, *16*, 3985; (h)

M. L. Bushey, T.-Q. Nguyen, C. Nuckolls, *J. Am. Chem. Soc.*, **2003**, *125*, 8264; (i) K. Tamada, H. Akiyama, T. X. Wei, *Langmuir*, **2002**, *18*, 5239; (j) E. W. Wong, C. P. CollierM. Be˘hloradsky´ , F. M. Raymo, J. F. Stoddart, J. R. Heath, *J. Am. Chem. Soc.*, **2000**, *122*, 5831; (k) I. Willner, B. Willner, *J. Mater. Chem.*, **1998**, *8*, 2543.

[27] S. M. Chergui, A Ledebt, F. Mammeri, F. Herbst, B. Carbonnier, H. B. Romdhane, M. Delamar, M. M. Chehimi *Langmuir* **2010**, *26*, 16115-16121.

[28] S. Gam-Derouich, B. Carbonnier, M. Turmine, P. Lang, M. Jouini, D. B. Hassen-Chehimi, M. M. Chehimi *Langmuir* **2010**, *26*, 11830-11840.

[29] T. Gupta, M. E. van der Boom, *Angew. Chem., Int. Ed.*, **2008**, *47*, 5322–5326.

[30] Altman, M.; Zenkina, O.; Evmenenko, G.; Dutta, P.; van der Boom, M. E. *J. Am. Chem. Soc*. **2008**, *130*, 5040.

[31] A. Gulino, T. Gupta, P. G. Mineo, M. E. van der Boom, *Chem. Commun.*, **2007**, 4878.

[32] A. Gulino, S. Bazzano, G. Condorelli, S. Giuffrida, P. Mineo, C. Satriano, E. Scamporrino, G.Ventimiglia, D.Vitalini, I. Fragalà *, Chem. Mater.,* **2005** *17*, 1079-1084.

Chapter 2

Porphyrin Nanostructures

Porphyrins exhibit several properties such as photo- and redox-chemistry, electron transfer reactions, luminescence, sensing capabilities, non-linear optical behaviours, biological roles, magnetic properties,[1] etc. Moreover they can be smartly modified by adding/changing the macrocycle peripheral substituents and/or by changing the oxidation state of the metal center. They show important redox characteristics as formation of π-cation radicals that are relatively stable under ambient conditions and exhibit multiple cationic states that are accessible at relatively low potentials. One important application of porphyrin nanostructures is that, when attached to an electroactive surface, information can be stored in the discrete redox states of these molecules and porphyrin properties afford the possibility of increased memory density (via multi-bit information storage) with decreased power consumption (low potentials and long charge-retention times), and thus molecular-based information storage materials.[3]

In addition well organized porphyrin molecules, covalently anchored to transparent substrates, act as highly sensitive systems to ppm levels of different analytes and then can be used as well-suited, fast and reversible optical sensors.[2]

Therefore we firstly studied the fabrication of well-ordered and densely packed porphyrin nanostructures on Si(100) surfaces.

The second study focused on the ability of nanostructured systems to chemically communicate with the surrounding environment. In particular, it was studied the ability of porphyrin molecules assembled on quartz substrates (hardware) to change chemical information with copper (II) solutions, representing external chemical stimuli. This study falls within the production of molecular based information storage materials.

Finally it was pursued the fabrication of some nanostructures based on the covalent bonding of a porphyrin or its copper complex on the surface of two metal oxides (SnO_2 and TiO_2) for the Dye Sensitised Solar Cells (DSSC) technology. In fact, it is well known that porphyrins and/or metallo-porphyrins assembled on nanostructured semiconducting metal oxides such as TiO_2 or SnO_2 play a fundamental role for the conversion of solar energy to electricity and for other optical applications,[4-14] as a consequence of an electron injection effect from the pophyrin levels to the metal oxide. The specific aim was to demonstrate how the electron injection property results increased if molecules are covalently bound (not physisorbed) to the inorganic oxide surfaces.

2.1 Ordered Porphyrin Nanostructures on Si(100)

Engineering of Si(100) with ordered porphyrin nanostructures represents an advanced method to manufacture hybrid organic/inorganic systems useful for different applications. To achieve a long range order it is important to control location, growth and shape of the forming nanostructures. The porphyrin used in this study is the 5,10,15,20-tetra(4-pyridyl)-21H,23H-porphine, P, (Figure 2.1.1) that possesses four pyridine groups available for surface grafting.[15]

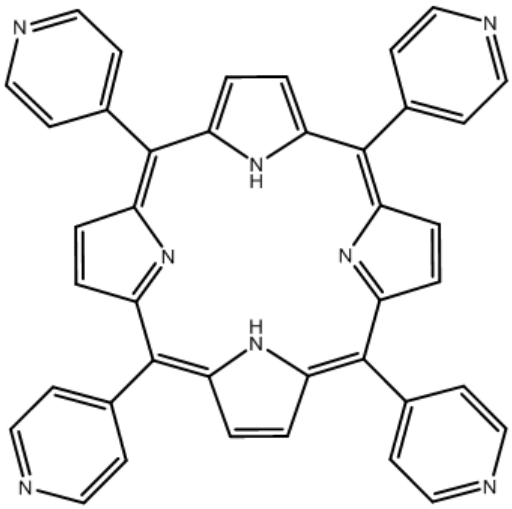

Figure 2.1.1 Structure of the 5,10,15,20-tetra(4-pyridyl)-21H,23H-porphine.

2.1.1 Synthesis of Porphyrin Nanostructures on Si(100)

Silanized Si(100) substrates, were loaded into glass pressure vessels under N_2, immersed in a freshly prepared 1.5 x 10^{-3} M toluene solution of 5,10,15,20-tetra(4-pyridyl)-21H,23H-porphine (Aldrich) and heated up to 90 °C for 75 h. Pyridil porphyrin molecules graft to the -CH_2Cl group of the silanized substrate through a quaternization reaction of the pyridine nitrogen. Then, the functionalised substrates bearing the covalently self-assembled porphyrin nanostructures (Scheme 2.1.1) were left to cool to room temperature and repeatedly washed and sonicated with toluene and dichloromethane to remove any residual physisorbed material. After the washing procedures, the porphyrin molecules are chemically bound to the substrate surface

through covalent bonds (Si(100)_CA_P).

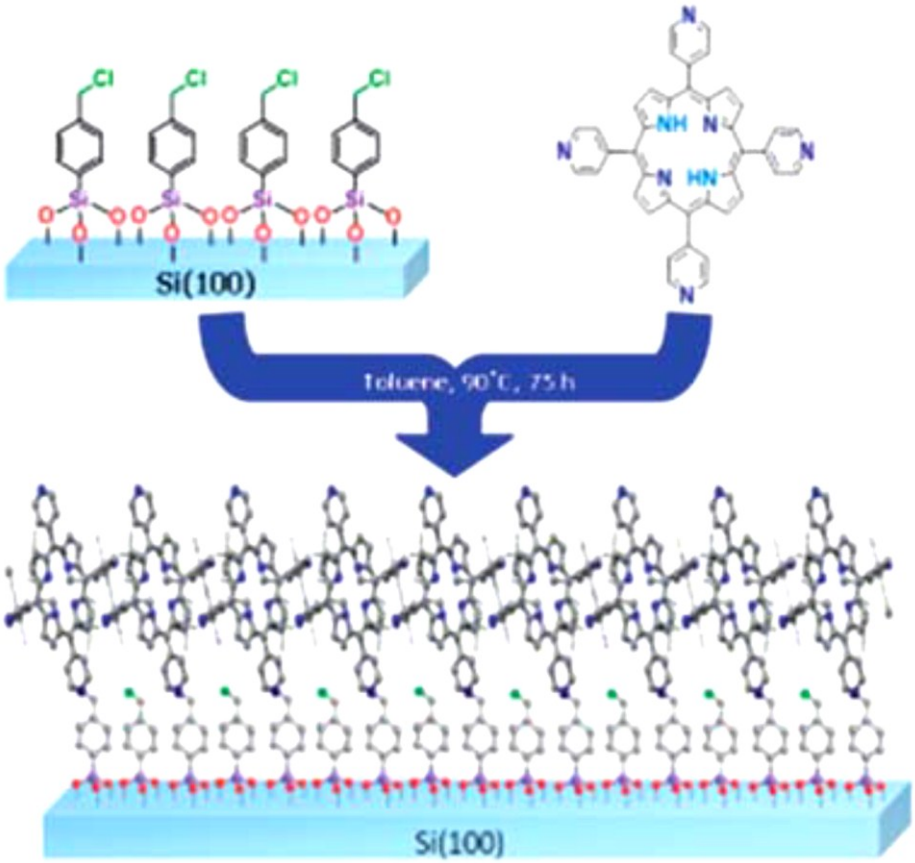

Scheme 2.1.1. Synthesis pathway for nanoscale covalent porphyrin structures on Si(100).

2.1.2 Characterization of Porphyrin Nanostructures on Si(100)

The system was firstly characterized by FT-IR spectra (Figure 2.1.2) using a Jasco FT-IR-430 spectrometer. Four hundred scans (scan range 400–4000 cm^{-1}, resolution 4 cm^{-1}) were collected.

The spectrum shows the N–H out-of-plane peak at 816 cm^{-1}, the C–H bending at 896 cm^{-1}, the pyrrole breathing and the pyridine C–H out-of-plane at 960 cm^{-1}, the pyrrole symmetric half-ring stretching at 1296 cm^{-1}, the pyrrole symmetric quarter-ring stretching at 1376 and 1396 cm^{-1}, and the pyridine CH wagging mode at 1448 cm^{-1}.

These peaks are typical of the pyridil porphyrin used for the synthesis of the system and confirm the presence of this molecule on the Si(100)_CA substrate.

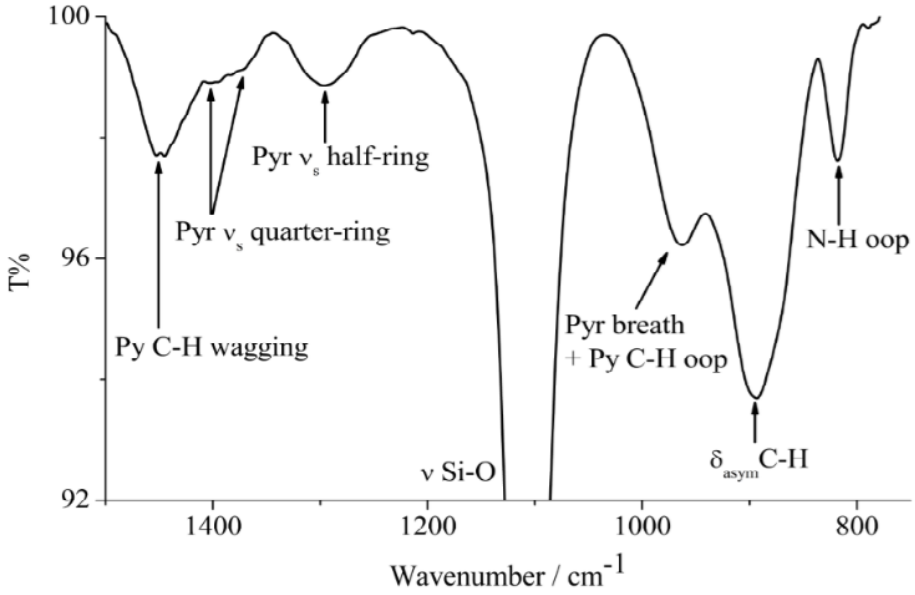

Figure 2.1.2. FTIR spectrum of the Si(100)_CA_P in the 750–1550 cm^{-1} range.

X-Ray photoelectron spectroscopy (XPS) was used to describe the surface elemental composition and the bonding state of the grafted molecules. Angle Resolved X-ray Photoelectron Spectra (AR-XPS) were measured at different (5°, 15°, 30°, 45° and 80°) take-off angles. High resolution spectra were acquired in the range of binding energies (B.E.) related to: C 1s, Si 2p, N 1s, and Cl 2p. Figure 2.1.3 shows the high-resolution N 1s XP spectrum of the Si(100)_CA_P. The fitting of the N 1s signal reveals the presence of two components in a 1 : 7 ratio. These two peaks lie at 399.9 and 402.2 eV. As a consequence, the component at 399.9 eV is assigned as a whole to the four pyrrole nitrogens of the porphyrin core and to three of the four pyridine nitrogens.[16] This assignment is in tune with already reported XPS data on porphyrins.[17-18] The higher energy component is consistent with a quaternised nitrogen of a pyridine moiety (Scheme 2.1.1).[19-23] It emerges that the porphyrin molecule grafts onto the silanized Si(100) substrate using only one pyridine moiety.

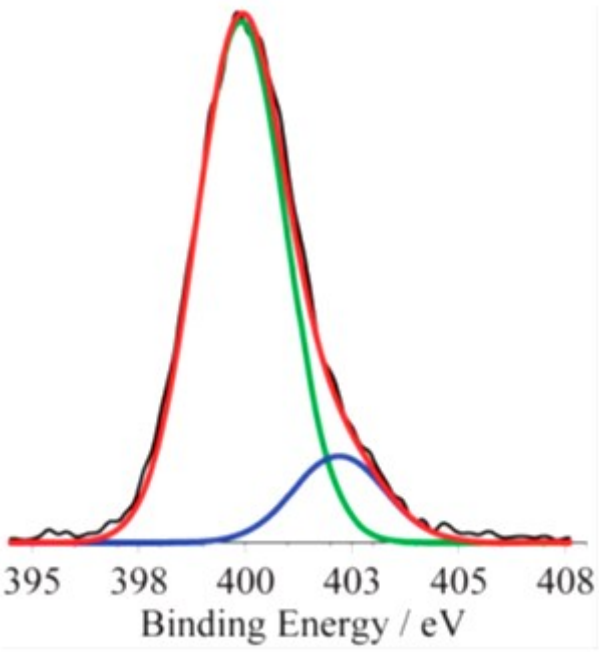

Figure 2.1.3. Monochromatized Al-Kα excited AR-XPS of a representative Si(100)_CA_P in the N 1s binding energy region at a 45° take-off angle.

Using the following equation:

$$\frac{I_{\mathrm{N}}}{I_{\mathrm{Si}}} = \frac{n_{\mathrm{N(atom\ per\ cm^3)}}\sigma_{\mathrm{N}}\lambda_{\mathrm{N/monolayer}}T(E_{\mathrm{N}})\left(1-\mathrm{e}^{\frac{(d_{\mathrm{N/monolayer}})}{\lambda_{\mathrm{N/monolayer}}\cos\theta}}\right)}{n_{\mathrm{Si(atom\ per\ cm^3)}}\sigma_{\mathrm{Si}}\lambda_{\mathrm{Si/Si}}T(E_{\mathrm{Si}})\left(1-\mathrm{e}^{\frac{d_{\mathrm{N/monolayer}}}{\lambda_{\mathrm{Si/monolayer}}\cos\theta}}\right)}$$

where:

- I represents the XPS peak intensity;
- n_N represents the number of N-containing molecules per cm^2 in the monolayer;
- σ is the photoelectron cross-section;
- λ is the inelastic mean free path;
- *T*(E) is the analyser transmission function of the XPS instrument;
- *d* is the monolayer thickness (ca. 2.4 nm from morphology characterisation);
- θ is the photoelectron take-off angle

it was possible to estimate n_N corresponding to the surface coverage of the

Si(100)_CA_P. Taking into account 8 nitrogen atoms per porphyrin molecule, values of 2.4 to 3.6 x 10^{13} (mean value 3.0 x 10^{13}) porphyrin molecules per cm^2 were obtained. These values are totally consistent with already reported results on similar systems.[16]

Surface morphology studies were carried out by Atomic Force Microscopy (AFM) and the images were obtained by an instrument manufactured by NT-MTD. The noise level before and after each measurement was 0.01 nm. AFM characterizations were performed in a high-amplitude mode (tapping mode) to avoid any possible modification of the grafted organic layer on the surfaces, caused by the interactions with the tip whose nominal curvature radius is 10 nm. Figure 2.1.4 (left) shows a representative AFM micrograph for a Si(100)_CA_P functionalised substrate.

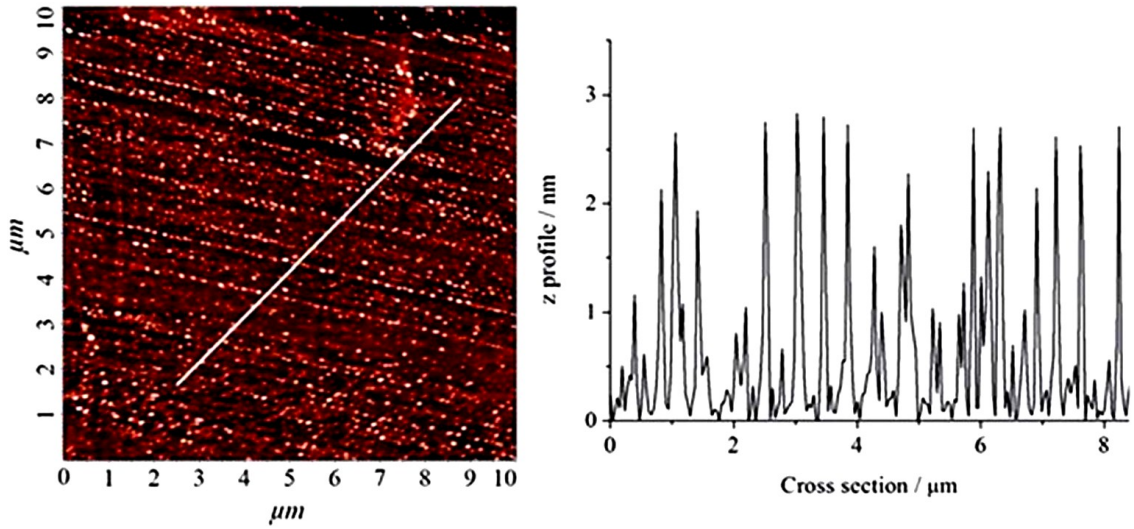

Figure 2.1.4. AFM image (left) for the representative Si(100)_CA_P monolayer and related cross-section profile (right).

The micrograph for the Si(100)_CA_P sample shows a relevant number of long structures having a linear arrangement that nucleated and grew-up on the substrate surface. The cross-section analysis (Fig. 2.1.4, right) shows structures whose height (peak-to-peak) is ca. 2.4 nm and widths of 40–60 nm. This structure height is consistent with the size of the CA_P since the silane unit length is 7.2 Å and the porphyrin size obtained by quantum mechanical calculations resulted to be 16.7 Å.[24] A few other shorter structures are also apparent because the monolayer set-up is not

perfectly homogenous on the molecular scale.[25] In fact, the mean height value observed in the AFM cross-section, evaluated across the entire area of Figure 2.1.4, is 1.2 nm (*see Density Fuctional Theory, DFT, results*). These surface structures evidence a long range order of more than 10 μm. Moreover, all the observed structures are parallel to each other thus showing the same direction. This suggests the presence of well-defined porphyrin nanostructures in an upright configuration.

Figure 2.1.5 shows a higher magnification AFM for the representative Si(100)_CA_P monolayer that gives a better idea of the density and size of porphyrin "crystallites" along the linear arrangement.

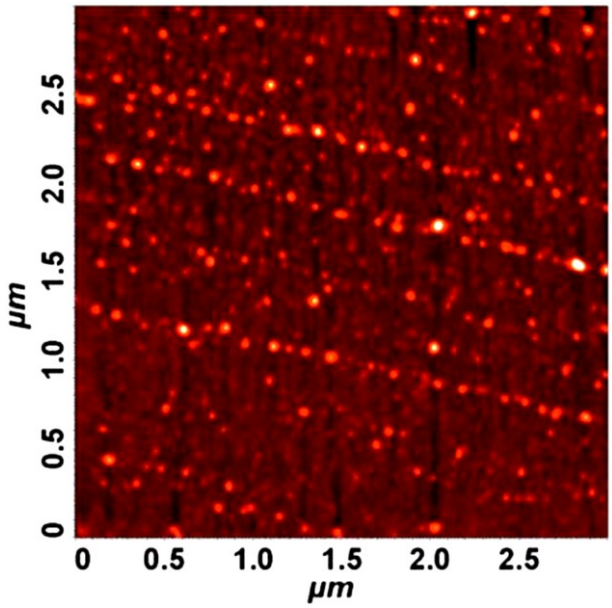

Figure 2.1.5. High magnification AFM image for the representative Si(100)_CA_P monolayer showing widths of single domains in the 40–60 nm range.

Finally, to have an idea about the 3D geometrical disposition of the porphyrins in the space after the anchoring to the substrate, accurate *DFT* quantum mechanical calculations were performed on a single porphyrin–silane system, adopting the closed shell PBE formalism (from Perdew, Burke and Ernzerhof) for both exchange and correlation functionals.[26] The standard all-electron 6-31G** basis set was used for all atoms.[27] Molecular geometry optimization of stationary points was carried out without symmetry constraints and analytical gradient techniques were used. All calculations

were performed using G09 code on linux cluster systems.[28] Results indicated that porphyrin molecules are tilted by 67° with respect to the normal to the substrate surface (Figure 2.1.6).

In fact, the pseudo-tetrahedral angle of the benzyl carbon with the quaternized nitrogen is 113° instead of 109°. By taking into account this tilting angle, many structure heights observed with AFM seem to be somewhat larger (ca. 2.4 nm) than those evaluated by *DFT* (ca. 1.2 nm). But, the mean height value observed in the AFM cross-section, evaluated across the entire area of Figure 2.1.4, is 1.2 nm, consistent with the value estimated on the basis of the *DFT* results.

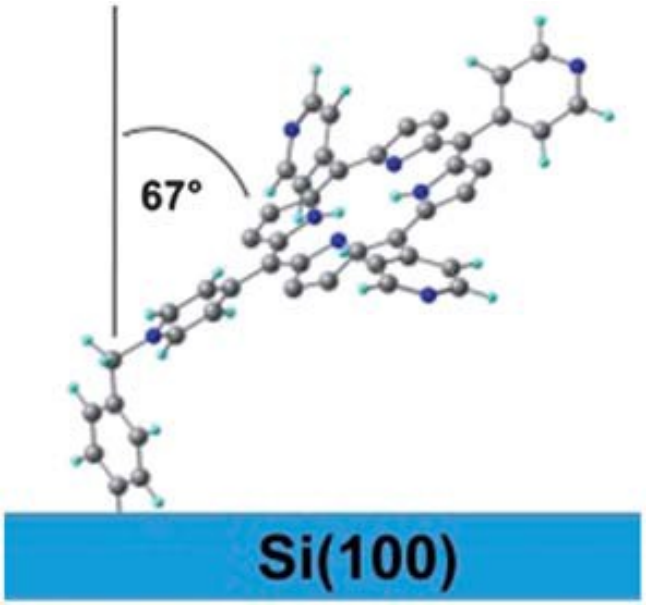

Figure 2.1.6. *DFT* optimization of the Si(100)_CA_P grafting geometry.

We already anticipated that the monolayer set-up is not perfectly homogenous on the molecular scale therefore, it is likely that in this monolayer there are porphyrin molecules either tilted or in the up-right grafting geometry. Both tilted and up-right arrangements should continue to promote good stacking between rings of vicinal porphyrins. The computed footprint of a single porphyrin molecule of 210 $Å^2$ is broadly compatible with its XPS evaluation (330 $Å^2$, obtained from 3.0 x 10^{13} porphyrin molecules per cm^2) when, according to the AFM cross-section profile, about 60% surface coverage is taken into account.

In order to verify whether porphyirins covalently bound to the substrates hold the luminescence properties, fluorescence measurements were carried out using a Varian Cary Eclipse Fluorescence spectrophotometer with a λ_{exc} of 420 nm and at 1 nm resolution, at room temperature. The emission was recorded at 90° with respect to the exciting line beam using 10:10 slit-widths. Spectra were collected at room temperature. Particularly, Figure 2.1.7 shows two strong emissions at λ = 663 and 718 nm. These results are in agreement with already reported measurements on porphyrin monolayers assembled on solid substrates and confirm that the observed packing due to directional π–π stacking and other more complex forces does not quench the photoluminescence properties.[29-30]

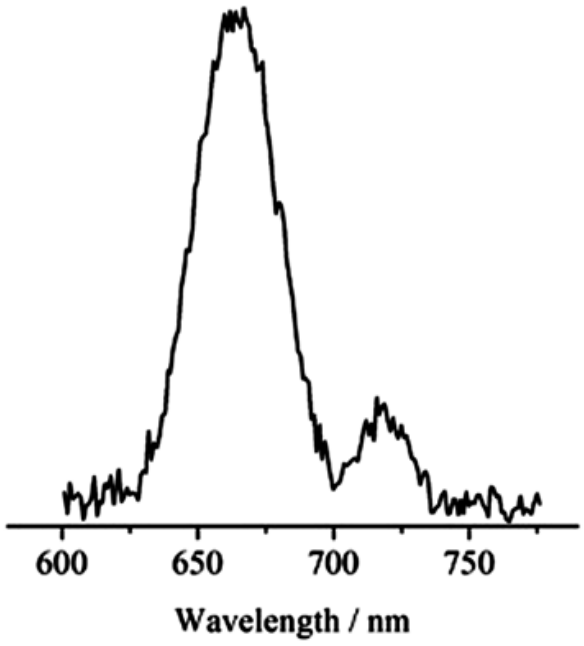

Figure 2.1.7. Photoluminescence spectrum of Si(100)_CA_P.

2.1.3 Results and Discussion

From the overall data analysis it results evident that a quite ordered monolayer of porphyrins on silanized Si(100) was grown. Since no discrete bonds are expected between the porphyrin single molecules, probably vicinal porphyrin molecules interact to align the rings and allow π–π stacking. This interaction leads to an overlap between the electronic states of individual porphyrin units. Moreover, the width of these

nanostructures could be due to inter-chain van der Waals and/or additional lateral π–π stacking interactions between the pyridine moieties. These lines are similar to styrene structures on the order of nm observed on Si(111) engineered substrates and reported in literature.[31] In fact, Lopinski et al. reported on the growth of straight molecular styrene lines and proposed that the crystalline silicon substrate determines both the orientation of the lines and the molecular spacing within them.[32] The method described for self-directed growth of molecular nanostructures on silicon should allow parallel fabrication of identical complex functional structures and could be sufficiently controllable to be useful in forming and/or connecting nanostructures.[32]

According to recent published works, ordered structures of polystyrene, in the μm range, on Si(111) engineered substrates have been also observed.[33-34] Other studies reported on the self-assembly properties of particular porphyrins, thus demonstrating that the strong porphyrin–substrate interaction enables a broader variety of structures[35] and that, the occurrence of porphyrins, assembled into patterns, depends on the interplay between directional hydrogen-bonding interactions and packing forces, including molecule–molecule and molecule–substrate interactions.[36] Taking into account the crosslinking ability of the trichloro[4-(chloromethyl)phenyl]silane molecules during the surface grafting it seems that the silane functionalised Si(100) template monolayer may encourage this order to the present porphyrin nanostructures.[37-38]

The most important result obtained from this study is that Si(100)_CA_P shows porphyrin nanostructures with a longer order range, more than 10 μm , than that observed in other systems and, despite molecule-molecule interaction, porphyrins preserve single molecule properties, such as their luminescence. Therefore such a system could be useful in the optoelectronic field.

2.2 Dynamics of the Chemical Communication between a Solid Nanoarchitecture and Cu(II) solutions

Chemical communication may comprise very intricate processes that allow biological organisms and inorganic systems to transfer information.[39] An interesting aspect of SRMs is the ability to communicate with the surrounding environment and produce outputs that can be read-out in a fast and precise way. In this context the optical read-out is one of the most reliable procedures. There exist many recent studies of intermolecular communication within thin films.[40-42] An example of chemical communication between metal-complex based monolayers is represented by the study of van der Boom.[43] Moreover some attention has been paid to the transfer of information between self-assembled organic or polymeric surfaces.[44-48] Additional examples refer to the electrochemical reaction along the solid–liquid–gas interface,[49] binary logic with synthetic molecular and supramolecular species,[50] integration of chemical logic gates,[51-53] surface reactions of self-assembled silane monolayers,[54] and molecular computing. [54]

In this context it was studied the communication between a porphyrin monolayer and different amounts of dilute copper(II) solutions to find out the involved dynamics. This is an example of a stimuli responsive porphyrin monolayer (hardware) subjected to the Cu(II) stimulus (input). The optical readout (output) was indicative of the degree of the communication (reaction) that it was possible to control. It was assembled a covalent monolayer of 5,10,15,20-tetrakis(4-hydroxyphenyl)-21H,23H-porphine (H2THPP) (Figure 2.2.1) on a previously silanized quartz substrate in order to get the H2THPP_SAM system. [39]

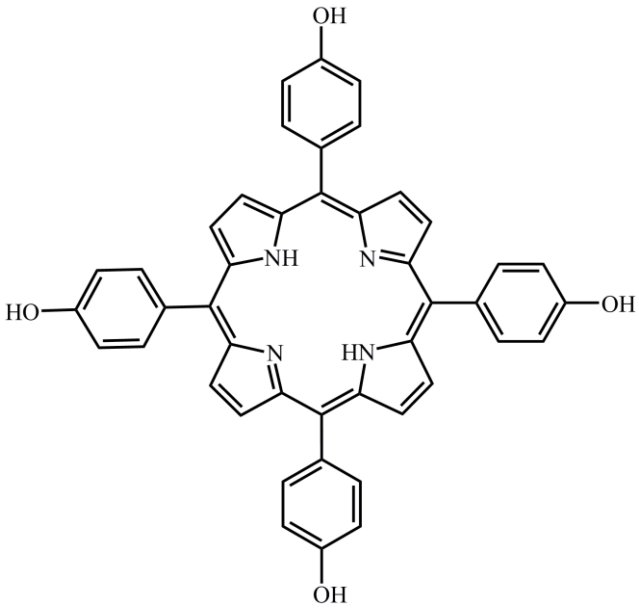

Figure 2.2.8. Structure of the 5,10,15,20-tetrakis(4-hydroxyphenyl)-21H,23H-porphine.

2.2.1 Synthesis of a SAM of Porphyrin

Freshly silanized substrates were immersed in an acetonitrile H2THPP 6.5 x 10^{-4} M solution and kept at 70 °C for 70 h while stirring. The H2THPP_SAM formed was left to cool to room temperature and then sonicated 15 min with CH_3CN to remove any residual unreacted porphyrin (Scheme 2.2.1, left).

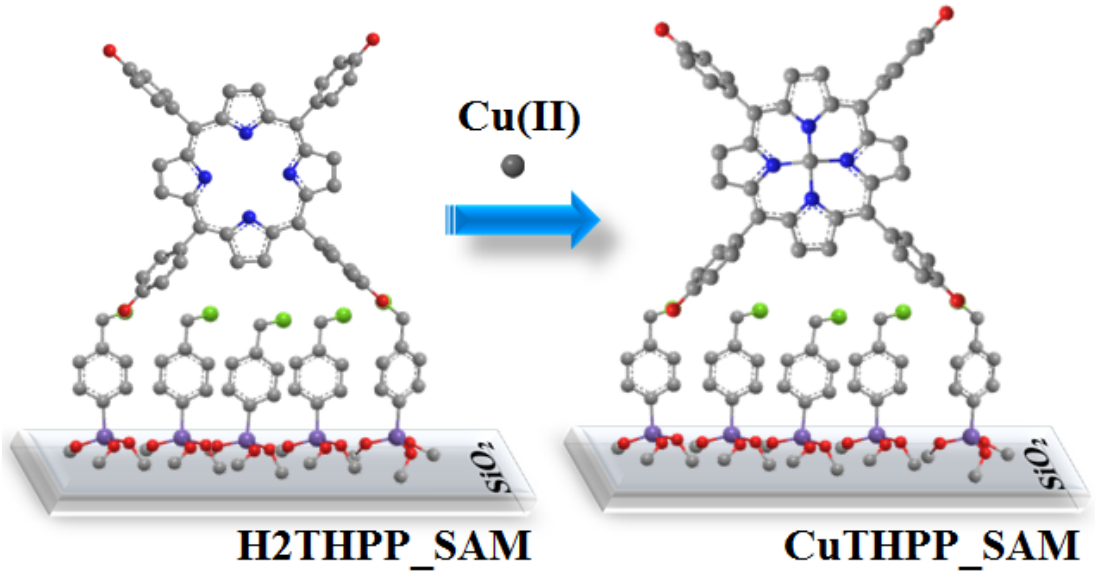

Scheme 2.2.1. Grafting arrangement in H2THPP_SAM and CuTHPP_SAM.

2.2.2 Characterization of a SAM of Porphyrin

The system was widely characterised by AR-XPS (5°, 15°, 45° and 80° take-off angles).

Figure 2.2.2 shows the fitting of the XP spectrum in the O 1s B.E. region of the H2THPP_SAM. Apart the main peak, due to the oxygen of the SiO_2 (quartz) substrate, two other additional peaks at 533.0 and 532.1 eV were essential for the fit. Moreover, the fit revealed identical intensity for these two peaks.

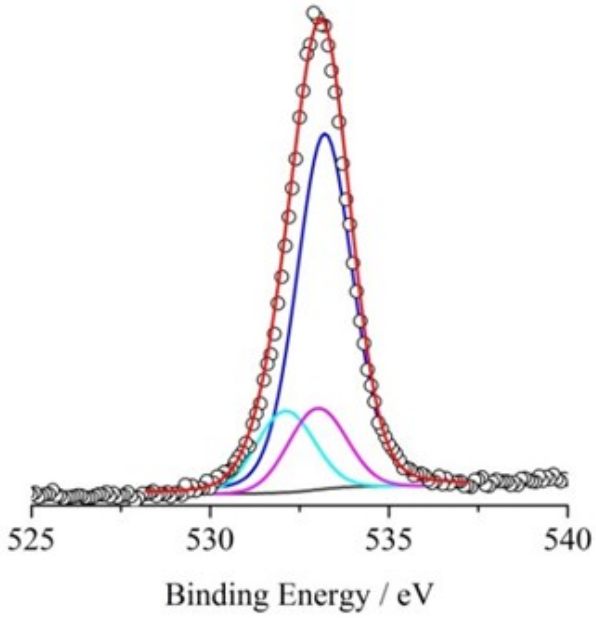

Figure 2.2.2. Monochromatized Al-Kα excited XPS of a representative H2THPP_SAM in the O 1s binding energy region at 45° take-off angle. The experimental spectral data points (open circles) are fitted with three dominant gaussians at 532.1 eV (cyan line), 533.0 eV (magenta line) and 533.2 eV (blue line). The red line superimposed to the experimental profile refers to the sum of the Gaussian components.

On the basis of previously reported data, these two peaks are consistent with the presence of phenol and ether functions. Therefore it emerges that the tetra-hydroxyphenyl-porphine on the H2THPP_SAM shows two phenol and two ether functions thus suggesting a grafting geometry involving two by four phenol groups (Scheme 2.2.1). This result is totally in agreement with already reported data on similar studies.[29]

Figure 2.2.3 (black line) shows the XP spectrum of the H2THPP_SAM in the N 1s binding energy region and it is evident the broad 1 + 3 band convolution with signals at 398.5 and 400.1 eV, typical of unmetalled porphyrins.[55-56]

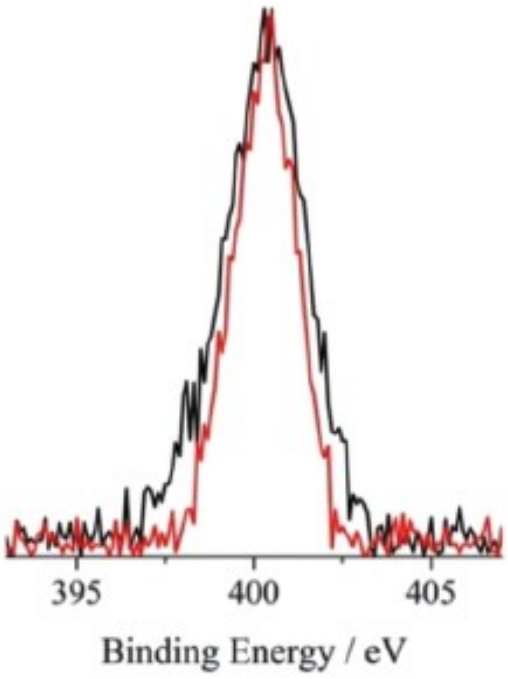

Figure 2.2.3. Al-Kα excited XPS of the as synthesized H2THPP_SAM (black line) and CuTHPP_SAM (red line) in the N 1s binding energy region at a 45 degree take-off angle.

Figure 2.2.4 shows the AR-XPS angular dependence of the I_C/I_{Si} intensity ratios (I_C and I_{Si} are the total intensities of carbon and silicon, respectively) vs. the photoelectron take-off angle for the H2THPP_SAM.[48, 55-60] The ratios exponentially decrease with the take-off angle, θ, consistently with the presence of a carbon overlayer on SiO_2. The I_C/I_{Si} intensity ratio can be modelled as follows:

$$\frac{I^C}{I^{Si}} = \frac{I_\infty^C (1 - e^{\frac{-d}{\lambda_{C1s}^C sen\theta}})}{I_\infty^{Si} e^{\frac{-d}{\lambda_{Si2p}^C sen\theta}}}$$

where $\lambda^C_{Si\ 2p}$ and λ^C_{C1s} are the mean free paths of Si 2p and C 1s photoelectrons in a

carbon overlayer and the $I^{C}\infty/I^{Si}\infty$ is the ratio of the Wagner sensitivity factors. The obtained *d* value is 27.4 ± 1.5 Å and is highly consistent with the presence of a monolayer of porphyrin molecules perpendicularly grafted on SiO_2.

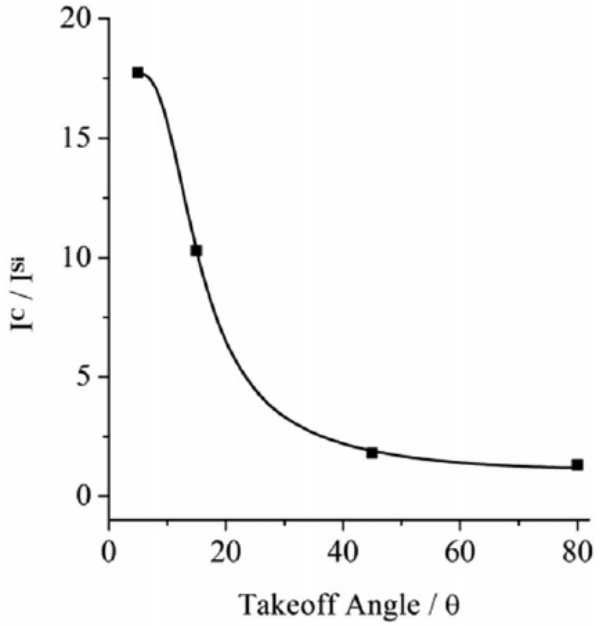

Figure 2.2.4. AR-XPS I_C/I_{Si} ratios vs the photoelectron take-off angle of the H2THPP_SAM. The R^2 value of the fit is 0.998.

The value of the thickness is also confirmed by the AFM measurements. In fact from morphology measurements of a representative H2THPP_SAM it emerges that the surface is rather homogeneous with a 2.61 ± 0.15 nm average height and a rootmean-square roughness of 0.72 nm (Figure. 2.2.5).

The H2THPP_SAM surface coverage was obtained by UV-Vis measurements. Acetonitrile H2THPP solutions in the 10^{-7}-10^{-9} M range, with absorbances in the order of 10^{-2}, (similar to those observed for the present H2THPP_SAM) were used for a correct evaluation of the molar extinction coefficient, ε (Figure 2.2.6, black line). The same procedure was carried out for diluted (10^{-7}-10^{-9}M) acetonitrile CuTHPP solutions (Figure 2.2.6, red line). All UV-Vis measurements were carried out with a 0.2 nm resolution at 25 °C using a diode-array Agilent 8453 spectrophotometer and the optical spectra were simulated using the ReactLab and Hyperquad software packages.[57-60]

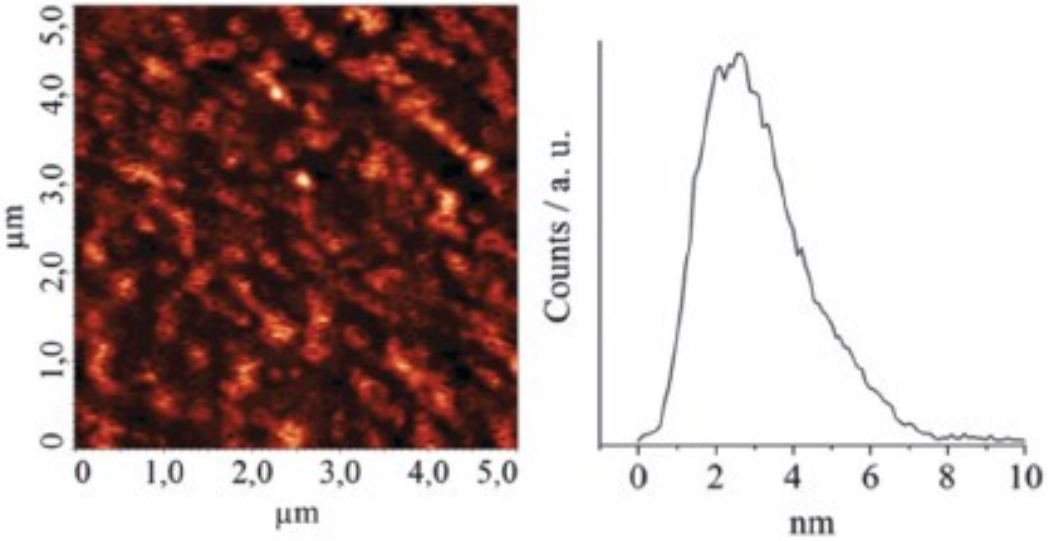

Figure 2.2.5. AFM image of the representative H2THPP_SAM (left) and related cross-sectional profile (right).

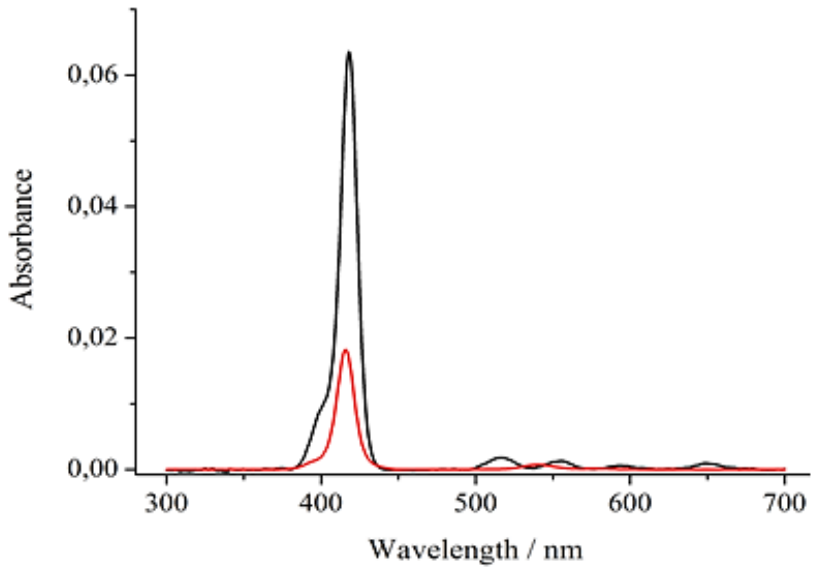

Figure 2.2.6. UV-Vis absorption spectra of acetonitrile H2THPP 1.37 x 10^{-7}M (black line) and CuTHPP 1.19 x 10^{-7}M (red line) solutions.

The obtained ε value for H2THPP is 572200 $M^{-1}cm^{-1}$ (at 418 nm) and 155500 $M^{-1}cm^{-1}$ (at 416 nm) for CuTHPP. The ε value found for H2THPP was used for calculating the porphyrin density by means of the Beer–Lambert law A =ε lc, where A is the absorbance and ε, l and c are the extinction coefficient, the thickness of the film

and the concentration of the molecules in the film, respectively. The obtained surface coverage, $d_{surf} = A\ \varepsilon^{-1}$ (number of molecules per cm^2), in H2THPP_SAM is 8.6 x 10^{12} molecules/cm^2.[61] This means 2.75 x 10^{13} molecules or 4.57 x 10^{-11} mol per substrate. This value is highly consistent with others reported on similar porphyrin monolayer systems.[62] In fact the resulting footprint of each porphyrin molecule (1160 $Å^2$) is three times larger than that estimated using the ChemBio3D program (360 $Å^2$) for a compact surface arrangement and this indicates the absence of significant aggregation phenomena and that the monolayer can be enough permeable.

2.2.3 Chemical Communication between a SAM of Porphyrin and Cu(II) solutions

The ability of H2THPP_SAM to chemically communicate with the surrounding environment was investigated by a complexation reaction between the present H2THPP_SAM and Cu(II) (Scheme 2.2.1), using aliquots of two acetonitrile $Cu(AcO)_2$ solutions having concentrations of the order of 10^{-6} and 10^{-4} M. Acetonitrile is a solvent that shows high affinity for both porphyrin and Cu(II) acetate. This experiment allowed to go deep inside the chemical reactivity of a system that differs from both classical homogenous and not-homogeneous reactants. In fact, it is known that a molecular monolayer cannot be envisaged as a solid bulk system, since single molecules possess a good degree of freedom, nor as a gaseous system since the grafted molecules are bound to the substrate surface. As a consequence the involved chemical reactivity can be rather different with respect to that of the typical chemical reaction media.

During the UV-Vis measurements the substrate (2 x 0.8 cm) bearing on both sides the porphyrin monolayer (whole area = 3.2 cm^2) was set inside a quartz cuvette using an appropriate Teflon substrate holder, (Figure 2.2.6), and 2.5 mL of acetonitrile were added to cover the substrate. The reference cuvette contained a silane functionalised quartz substrate on another Teflon substrate holder and 2.5 mL of acetonitrile. Then, increasing amounts of copper(II) acetate acetonitrile solutions (Table 2.2.1) were

added in both cuvettes using a precision burette (Hamilton, 1000 mL). After each addition, the system was allowed to equilibrate for 4 min prior to UV-Vis measurements. In particular, two 2.5 x 10^{-6} and 2.5 x 10^{-4} M copper acetonitrile solutions were used and 28 spectra were recorded for this experiment. The data, corrected for the volume variation, were subsequently analysed by using two different software packages namely ReactLab35 and Hyperquad36 that make use of a multiwavelength and multivariate treatment of spectral data.[57-60]

Figure 2.2.6. Set-up for UV-Vis measurements of the quartz substrate bearing a porphyrin monolayer.

Table 2.2.1. Additions of copper(II) acetate acetonitrile solutions for the conversion of the H2THPP_SAM in CuTHPP_SAM.

Addition	Mol of porphyrin in H2THPP_SAM	µL of $Cu(AcO)_2$ 2.5 x 10^{-6} M	$[Cu(AcO)_2]$ (mol/L)	Mol of $Cu(AcO)_2$ / Mol of porphyrin in H2THPP_SAM
0	4.57E-11	0	0	0
1	4.57E-11	5	5.00E-9	0.27
2	4.57E-11	10	1.00E-8	0.54
3	4.57E-11	20	2.00E-8	1.09
4	4.57E-11	40	4.00E-8	2.19
5	4.57E-11	60	6.00E-8	3.28
6	4.57E-11	100	1.00E-7	5.47
7	4.57E-11	140	1.40E-7	7.66
	Mol of porphyrin in H2THPP_SAM	µL of $(CuAcO)_2$ 2.5 x 10^{-4} M	$[Cu(AcO)_2]$ (mol/L)	Mol of $Cu(AcO)_2$ / Mol of porphyrin in H2THPP_SAM
8	4.57E-11	16.4	1.63E-6	89.72
9	4.57E-11	31.4	3.10E-6	171.77
10	4.57E-11	46.4	4.55E-6	253.83
11	4.57E-11	61.4	5.99E-6	335.89

12	4.57E-11	76.4	7.41E-6	417.94
13	4.57E-11	91.4	8.82E-6	500.00
14	4.57E-11	106.4	1.05E-5	582.05
15	4.57E-11	121.4	1.16E-5	664.11
16	4.57E-11	136.4	1.29E-5	746.17
17	4.57E-11	151.4	1.43E-5	828.23
18	4.57E-11	166.4	1.56E-5	910.28
19	4.57E-11	181.4	1.69E-5	992.34
20	4.57E-11	196.4	1.82E-5	1074.40
21	4.57E-11	211.4	1.95E-5	1156.45
22	4.57E-11	226.4	2.07E-5	1238.51
23	4.57E-11	241.4	2.20E-5	1320.57
24	4.57E-11	256.4	2.32E-5	1402.62
25	4.57E-11	271.4	2.45E-5	1484.68
26	4.57E-11	286.4	2.57E-5	1566.74
27	4.57E-11	301.4	2.69E-5	1648.80
28	4.57E-11	316.4	2.81E-5	1730.85

Finally, the system was characterized by XPS measurements. In particular, Figure. 2.2.2 (red line) shows a narrow and symmetric N 1s signal at 400.3 eV that is due to the equivalence of the porphyrin nitrogens upon the CuTHPP_SAM formation in which the copper complex has a local D_{4h} symmetry. The XPS atomic concentration analysis of the CuTHPP_SAM shows a N/Cu atomic ratio of 4.5 consistent with the 9% of the starting H2THPP_SAM and the 91% of the CuTHPP_SAM.

Figure. 2.2.7 describes the optical behaviour of the H2THPP_SAM upon three selected $Cu(AcO)_2$ additions. The starting Soret band at 427.6 nm shows a 9.6 nm red shift upon the porphyrin grafting with respect to the solution measurement. Moreover, the most dilute solution allowed to investigate the reaction pathway up to 50.0% of the total Abs variation (ΔAbs = 0.012) observed in experiments. In fact, after the addition of 3.5×10^{-10} mol of $Cu(AcO)_2$ (Table 1.1, [Cu(II)] = 1.40×10^{-7}) it was noted that the absorbance decreased to 0.01 (Abs_{50}) (Figure 2.2.7, red line) and this corresponds to the 61% of its initial intensity value (Abs_{100} = 0.016) (Figure 2.2.7, black line) and to the 50.0% of the total Abs variation. After the addition of 7.9×10^{-8} mol of $Cu(AcO)_2$ (Table 2.2.1, [Cu(II)] = 2.81×10^{-5}) the Abs value was 0.004 (Abs_0) (Figure 2.2.7, blue line) and this corresponds to the 25.0% of its initial intensity value. No other Abs variation was observed upon further $Cu(AcO)_2$ addition.

Therefore, it was obtained an optical ternary system whose readout procedure is

related to three absorbance values (0.016, 0.010 and 0.004) that can be used as thresholds and correspond to three different (mol of porphyrin in H2THPP_SAM) / (mol of the porphyrin Cu(II) complex in CuTHPP_SAM) ratios. Thus the present H2THPP_SAM may find potential interest for permanent memory storage. In fact, the observation of three distinct optical states Abs_{100}, Abs_{50}, and Abs_0, as a function of the [$Cu(AcO)_2$] concentration, can be exploited for integration of this ternary memory state system in optical devices.

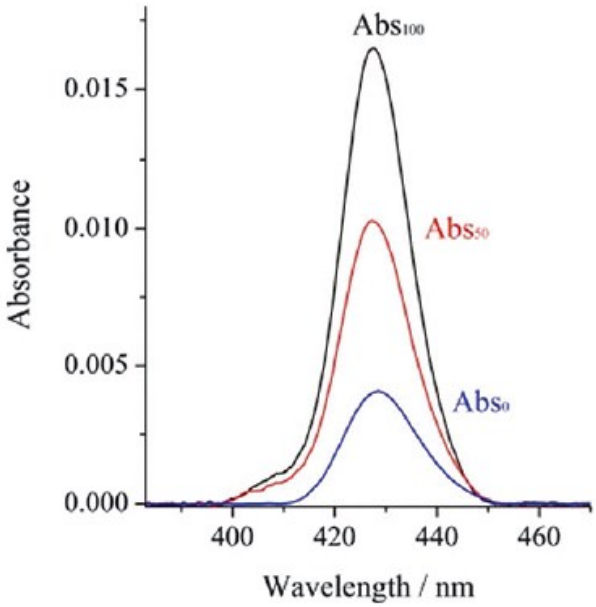

Figure 2.2.7. UV-Vis spectra H2THPP_SAM upon three selected $Cu(AcO)_2$ additions.

Figure 2.2.8 shows the overall optical variation of the H2THPP_SAM upon the $Cu(AcO)_2$ additions (Table 2.2.1). Therefore, the Soret (B-band) suffers a monotonic hypochromic effect consistent with the formation of the CuTHPP_SAM. The spectral changes, evident upon the $Cu(AcO)_2$ additions, can be interpreted in terms of the convolution of two Soret bands belonging to the H2THPP_SAM and CuTHPP_SAM whose ε values are significantly different (572200 and 155500 M^{-1} cm^{-1}, respectively).

The optical spectra in the Q-band region of the H2THPP_SAM upon the $Cu(AcO)_2$ additions show a decreased number of Q-bands (Figure 2.2.9, blue line). The starting bands for the H2THPP_SAM at 523.6, 563.6, 600.0, 656.8 nm reduce to

the 545.4 and 587.4 nm new bands. This observation is in agreement with the formation of the CuTHPP (Scheme 2.2.1, right).

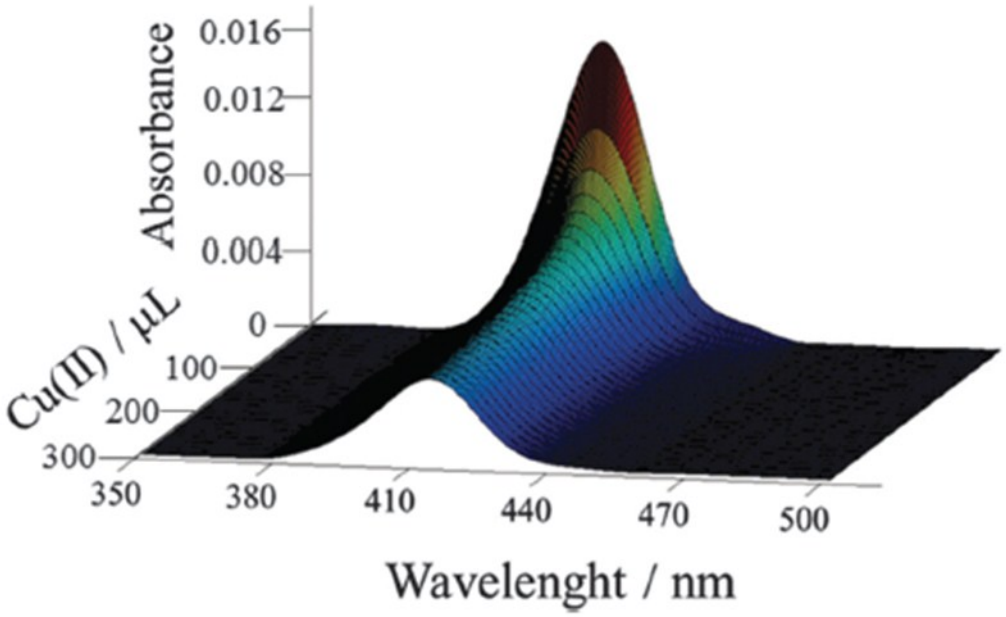

Figure 2.2.8. UV-Vis spectra of the H2THPP_SAM during the $Cu(AcO)_2$ additions.

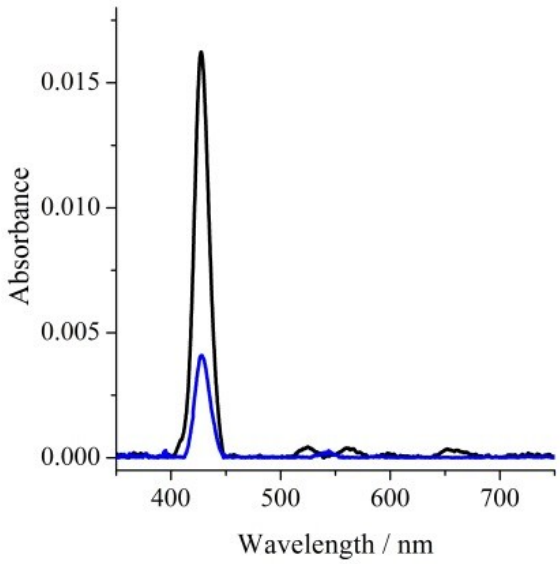

Figure 2.2.9. UV-Vis spectra of the starting H2THPP_SAM (black line) and upon 2.81 x 10^{-5} mol/L of $Cu(AcO)_2$ addition (blue line).

Figure 2.2.10 shows the relative absorbance variation during the $Cu(AcO)_2$

additions. In particular, Figure 2.2.10a shows the relative variations upon the addition of the most dilute 2.5 x 10^{-6} M $Cu(AcO)_2$ solution and Figure 2.2.10b shows the relative variations upon the addition of the 2.5 x 10^{-4} M $Cu(AcO)_2$ solution. In both cases almost linear behaviours are evident. These optical trends are highly desired. In fact, to exploit the ability of the present H2THPP_SAM nanoarchitecture to communicate with the solution, linear behaviour (outputs) upon external stimuli (inputs) easily allows the signal transduction to process the information and thus the development of devices useful in many important technological fields.

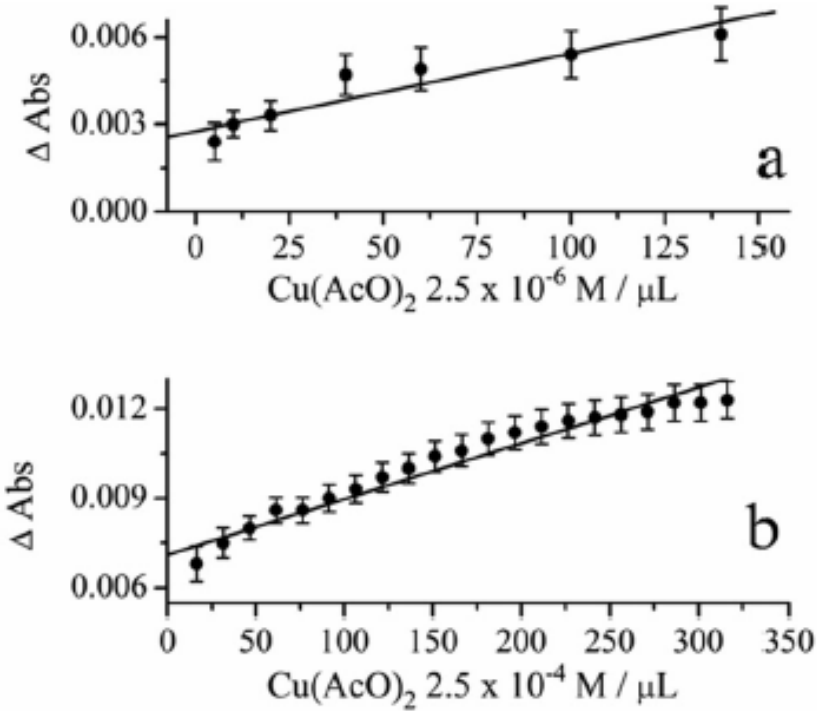

Figure 2.2.10. Relative absorbance variations during the 2.5 x 10^{-6} M (a) and 2.5 x 10^{-4} M (b) $Cu(AcO)_2$ additions. The R^2 values of the fits are (a) 0.96 and (b) 0.97.

It was also determined the stability constant of CuTHPP_SAM using the spectrophotometric experiment related to the following dynamic equilibrium reaction:

$$H2THPP\_SAM + Cu(AcO)_2 \leftrightarrow CuTHPP\_SAM + 2AcOH \quad \log K = 5.80$$

and it was found that the system shows a fairly high stability constant value (631000). This indicates the involvement of the four nitrogen atoms of the porphyrin ring in the

copper(II) coordination sphere. Interestingly, this value is in good agreement with already reported stability constants for similar solution reactions.[63]

Figure 2.2.11 shows the distribution diagram of the H2THPP_SAM and CuTHPP_SAM species obtained with the HYSS software package by simulating different additions of a unique 2.5 x 10^{-4}M $Cu(AcO)_2$ solution.[64] It can be noticed that the system forms only one complex species and the [H2THPP_SAM] / [CuTHPP_SAM] ratio = 1 at $\alpha = 0.5$ can be obtained when the concentration of the $[Cu(AcO)_2]$ is 1.63 x 10^{-6}. Indeed, this corresponds to the experimental cumulative $Cu(AcO)_2$ concentration reached after the first addition of the more concentrated solution in the reaction media (16.4 µL of $Cu(AcO)_2$ 2.5 x 10^{-4} M, Table 2.2.1). After 271.4 µL of $Cu(AcO)_2$, when the $[Cu(AcO)_2]$ is 2.45 x 10^{-5}, only the 6% of the starting H2THPP_SAM remained and the CuTHPP_SAM is now the 94% of the starting concentration.

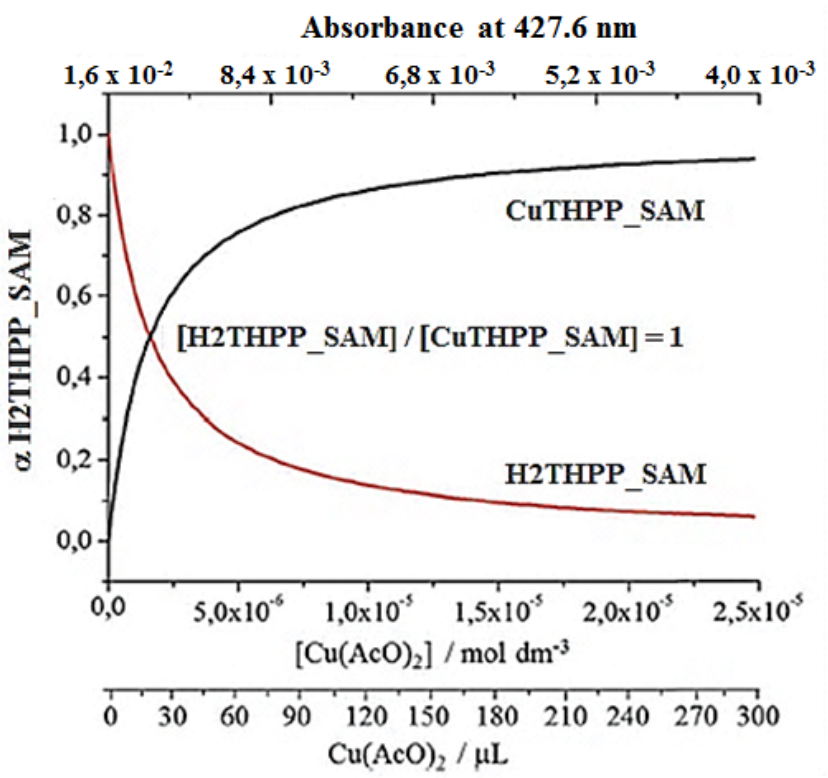

Figure 2.2.11. Distribution diagram of the [H2THPP_SAM] and [CuTHPP_SAM] calculated with the HYSS software package. Abscissa (bottom) shows both the $[Cu(AcO)_2]$ concentration and the corresponding volume addition of the 2.5 x 10^{-4} M $Cu(AcO)_2$ solution. The top abscissa shows the experimental absorbance corresponding to the $[Cu(AcO)_2]$ concentration reported in Table 2.2.1.

These calculated values are in close agreement with the experimental XPS evaluation based on the atomic concentration analysis. It emerges that each optical absorbance corresponds to a particular [H2THPP_SAM] / [CuTHPP_SAM] ratio.

In addition, the speciation study for this porphyrin and copper(II) was also carried out for acetonitrile H2THPP solutions (Figure 2.2.12).

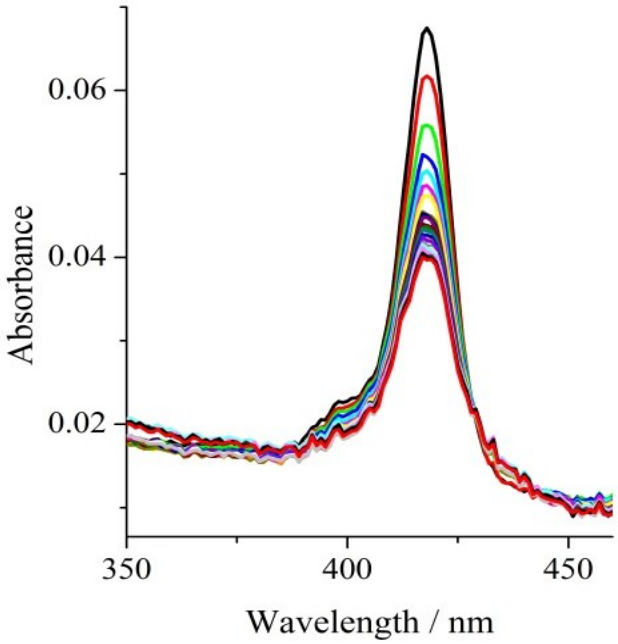

Figure 2.2.12. UV-Vis measurements of the acetonitrile H2THPP 1.37 x 10^{-7} M solution (2 mL) during the additions (5-200 μL) of the 3.62 x 10^{-4} M acetonitrile solution of $Cu(AcO)_2$.

In particular, Figure 2.2.13 shows three UV-Vis spectra registered during the solution H2THPP titration experiment: the starting spectrum (black line), the intermediate (blue line) and the final (red line). It is possible to note Abs variations in the Soret and in the Q-bands region. In detail, the initial 4 Q-bands at 515.6, 556.2, 594.0 and 648.6 nm respectively, reduce to two new bands at 544.2 and 581.6 nm upon Cu(II) additions, as similarly observed for the H2THPP_SAM.

From the ΔAbs data obtained during the solution titration it was calculated the log K value for such reaction and it was obtained a log K of 5.21 (stability constant = 162181), significantly smaller than that obtained for the H2THPP_SAM (log K = 5.80). This result suggests that the grafted complex is more stable than that formed in

solution probably owing to the lower ability of the cofacial molecules in CuTHPP_SAM to dissociate, and also because the preformed cofacial arrangement of the molecules facilitates the binding of the metal ion.[63]

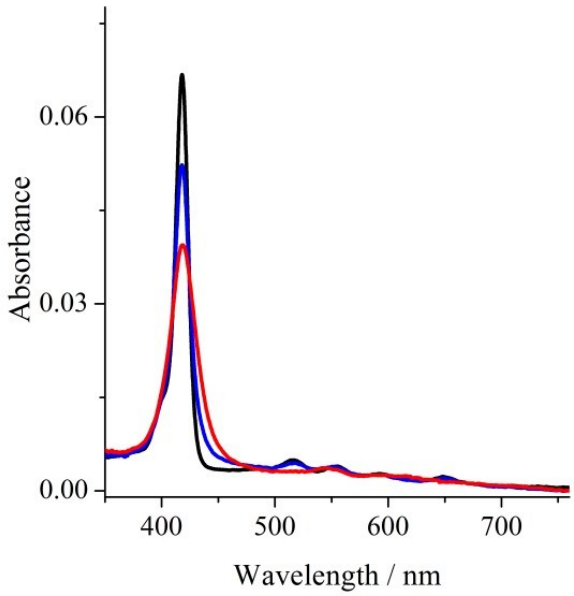

Figure 2.2.13. UV-Vis measurements of the acetonitrile H2THPP 1.37 x 10^{-7} M (2 mL) before (black line) and after the additions of 24 (blue line) and 200 (red line) μL of the 3.62 x 10^{-4} M acetonitrile solution of $Cu(AcO)_2$.

In summary H2THPP_SAM is a robust and stable SRM system that produces readable optical output upon external chemical stimuli. Each optical output corresponds to a precise chemical composition, namely a precise stable physical state. Therefore, such nanostructured system could have potential application for multi-bit information storage devices.

2.3 Porphyrins Functionalised TiO_2 and SnO_2 Nanocrystals

Nowadays the production of energy that satisfies the worldwide requirement is a need of the modern society. Renewable sources, as biofuels, biomasses, isothermal, geothermal, hydropower and solar energies are eco-friendly thus preferable. The solar energy impinging on the earth corresponds to 2.9×10^{12} TJ/year and that value overwhelms about 6.000 times the actual world annual need. Therefore it is not surprising that during the last decade attention was focused on the solar energy as major source for the energy production for the worldwide consumption.

In this context, photovoltaic devices, such as the dye sensitised solar cells, convert visible light to electrical energy.[65-72] In this technology the most used anode inorganic substrates are the transparent conducting oxides (TCOs) such as SnO_2 and TiO_2. [74-75] SnO_2 is a prototype oxide that adopts the tetragonal rutile structure (lattice parameters a= 4.737Å, c= 3.369 Å), belongs to the D^{14}_{4h} space group and contains two formula units per cell. In the SnO_2 there is a good level of metal-oxygen covalency that involves the diffuse Sn 5s and 5p atomic orbitals.[73] This covalency, in turn, causes a band-gap of 3.6 eV and a large O 2p valence band width (10 eV).[73] In TiO_2 the band-gap is 3.1 eV and the O 2p valence band width is 6.3 eV.[73] These differences are due to the fact that the conduction band states in TiO_2 are Ti 3d in nature whilst in SnO_2 involve the more diffuse Sn 5s and 5p levels. The attractive properties displayed by these nanostructures are based on their atomic scale structures and can be tailored for appropriate physico-chemical properties.[76] For example, low dimensional SnO_2 nanowires and nanobelts are highly sensitive and efficient transducers of surface chemical processes into electrical signals.[77-78] As anticipated above, porphyrins assembled on TiO_2 or SnO_2 play a leading role in the DSSC technology. If these dyes are physisorbed on the oxide surfaces, through-space electron interactions dominate.[79] In contrast, if the dyes are covalently assembled on the oxide surfaces,[80-82] through-bond electron interactions dominate thus increasing the device efficiency.[79] In fact,

these covalent systems overcome the problem of loss of efficiency during the electron injection since the dye layer is directly in contact (covalent) with the semiconductor surface.[65] Therefore well-organized porphyrin molecules, covalently anchored to appropriate nanosized conducting inorganic oxides, are promising materials for the next generation of molecular-based DSSC devices. In this perspective, the synthesis, characterization and optical properties of the free-base porphyrin H2THPP or its copper complex CuTHPP covalently assembled on TiO_2 and SnO_2 (hereafter, H2THPP_TiO_2, H2THPP_SnO_2, CuTHPP_TiO_2 and CuTHPP_SnO_2, respectively) were studied. To investigate the donor–acceptor effect between the porphyrin monolayers and the metal oxide the luminescence spectra of the different functional nanostructures presently synthesized were compared and it is announced that covalency between dye and semiconducting nanocrystals plays a fundamental role in the electron injection and in all cases the SnO_2 functionalised nanocrystals disclose the best donor–acceptor behaviour.[1]

2.3.1 Synthesis of Porphyrin Nanostructures on TiO_2 and SnO_2

The synthetic strategy already used for the covalent functionalization of flat substrates was adopted also in this case (Scheme 2.3.1). In detail, TiO_2 and SnO_2 white powders (Aldrich) were annealed overnight to 600°C in a furnace using recrystallised alumina crucibles and then, left to cool to room temperature and transferred in a glove-box under a N_2 atmosphere (1ppm H_2O, 1 ppm O_2). At that point, the single TiO_2 and SnO_2 powders were dispersed at room temperature in two *n*-pentane solutions (100 mL per each) 0.2 : 100 v/v of the silane coupling agent, soon removed from the glove-box in sealed flasks and sonicated for 60 min (25°C) to afford a CA monolayer on each crystal grain.[56] Afterward, the powder-containing flasks were moved back into the glove-box and the powders were decanted and washed with *n*-pentane 10 times while stirring. Then, they were removed from the glovebox and heated up to 135 °C for 15 min in an oven to complete the CA grafting. Subsequently, the powders were sonicated

twice in pentane for 5 min (25°C) to remove any eventual remaining physisorbed CA, decanted and transferred again in the glovebox. Then they were immersed into stirred 3.5×10^{-4} M CH_3CN 100 mL solutions of H2THPP, removed from the glovebox in sealed flasks, and sonicated for 7 h while heating at 50 °C. Then, the flasks were removed from the sonicator and heated-up to 70°C while stirring on an IKA RCT hotplate for 120 h. Similarly, some silanized TiO_2 and SnO_2 powders were left also to react with a 4.6 x 10^{-4} M CH_3CN solution of CuTHPP.

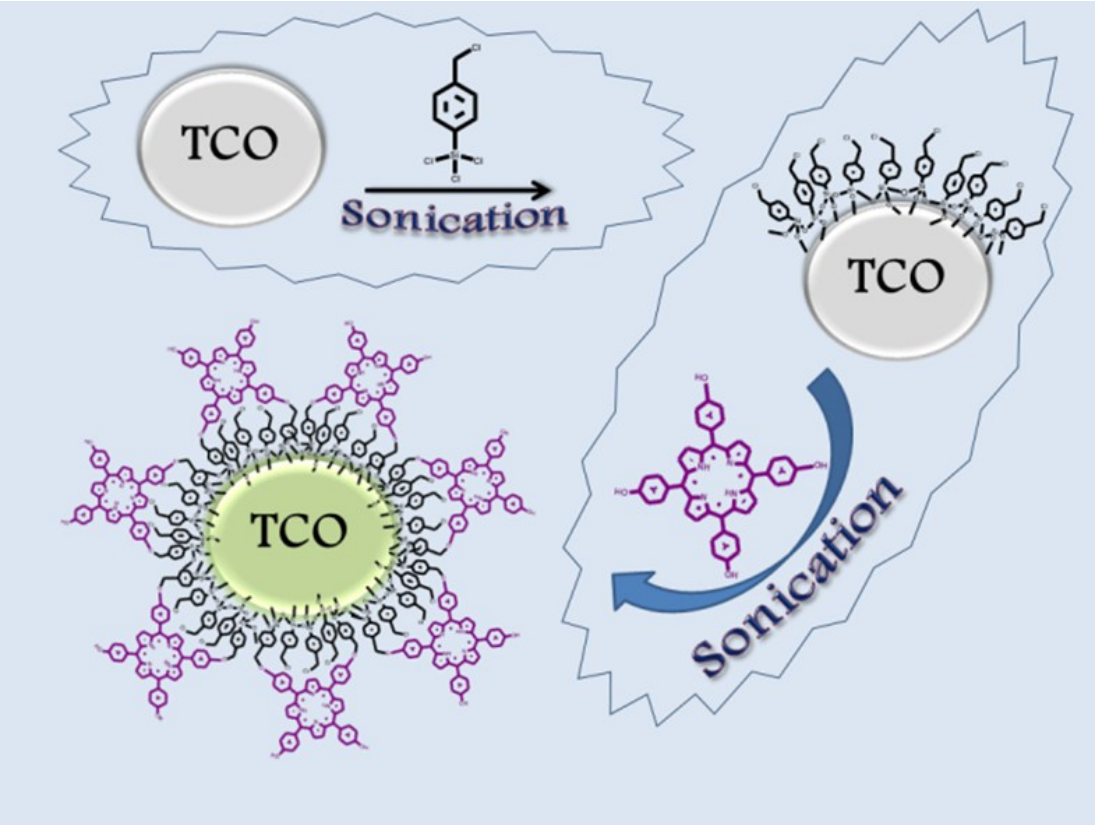

Scheme 2.3.1. Reaction pathway for TiO_2 and SnO_2 nanoparticles functionalised with a monolayer of H2THPP or CuTHPP.

Lastly, each suspension of the porphyrin (or CuTHPP) functionalised TiO_2 and SnO_2 was cooled to room temperature and subjected to multiple cycles of sonication/centrifugation-filtration until there was no UV-Vis evidence of any residual porphyrin in the remaining solutions. Each sonication (10 min) was performed in CH_3CN and the related centrifugation-filtration was achieved using a column (Sartorius Stedim Biotech) containing a molecular membrane having a 3000 MWCO

molecular weight cut-off, to remove any residual unreacted porphyrin. The filtration column was positioned at a fixed 25° angle in the centrifuge and, when subjected to 5000 rpm, the internal membrane restrains particles having a MWCO ≥ 3000. Pale yellow-green or pink nanocrystals were obtained for H2THPP or CuTHPP functionalised oxides, respectively.

The adopted synthetic procedure involves the sonication of the solutions during the powder silanization process since this reduces the presence of grain agglomerates. In addition, the sonication during the first 7 hours of reaction of the silanized grains with the porphyrin solutions is helpful in avoiding the formation of silanized oxide grain aggregates. Moreover, the sonication should partially prevent also some porphyrin aggregation due to the well-known stacking effect. Finally, the reaction time for the porphyrin grafting was much larger (120 h) than that typically used (Scheme 2.3.1).[56]

2.3.2 Characterization of Porphyrin Nanostructures on TiO_2 and SnO_2

The functionalised oxides were characterised by XPS, IR, UV-Vis, luminescence and Transmission Electron Microscopy (TEM) measurements.

Figure 2.3.1 shows the XP spectrum of the TiO_2 after the H2THPP grafting in the Ti 2p binding energy region. The two well resolved peaks at 459.3 and 465.1 eV represent the spin-orbit components of the Ti $2p_{3/2,1/2}$ states, respectively. These values are about 0.8 eV at higher B.E. with respect to those measured for pure TiO_2 annealed overnight at 600°C under a continuous 100 sccm (standard cubic centimetres per minute) flux of oxygen and that are typical of pure titania: Ti $2p_{3/2}$ = 458.5, $2p_{1/2}$ = 464.3 eV.

Figure 2.3.2 shows the XP spectrum of the SnO_2 after the H2THPP grafting in the Sn 3d binding energy region. The two well resolved peaks at 487.1 and 495.5 eV represent the spin-orbit components of the Sn $3d_{5/2,3/2}$ states.[56] Also in this case the observed values are at 0.8 eV higher B.E. with respect to those we measured for pure SnO_2 annealed overnight at 600°C under a continuous 100 sccm flux of oxygen (Sn

$3d_{5/2}$ = 486.3, $3d_{3/2}$ = 494.7 eV).

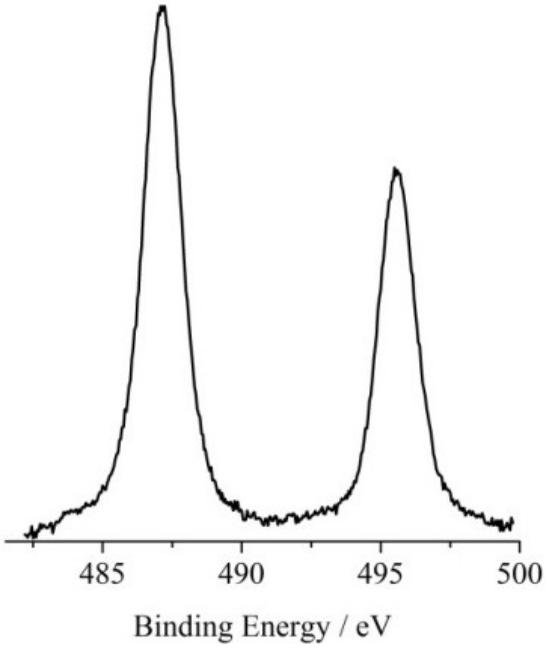

Figure 2.3.1. Al-Kα excited XPS of the H2THPP_TiO_2 in the Ti 2p binding energy region.

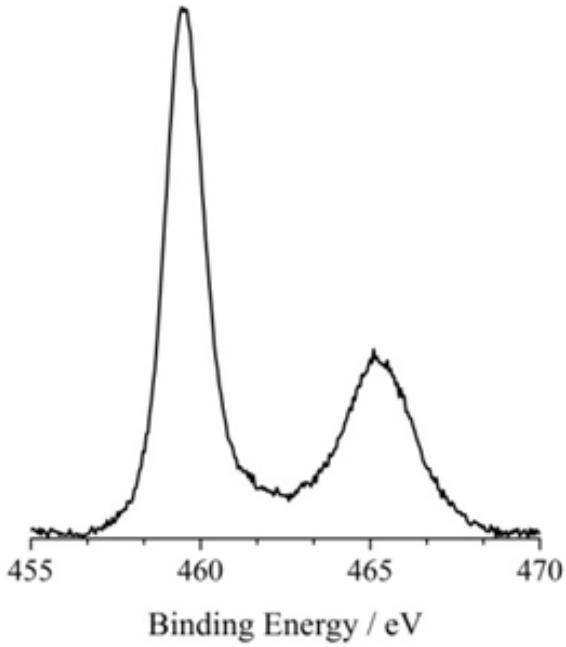

Figure 2.3.2. Al-Kα excited XPS of the H2THPP_SnO_2 in the Sn 3d binding energy region.

In contrast to these observations, the XPS N 1s main peak of both the H2THPP_TiO_2 and H2THPP_SnO_2 (Figure 2.3.3) lies at 400.1-400.2 eV that is at

lower B.E. with respect to that of the pure H2THPP (400.4 eV). In agreement with many previous reported data on similar systems, a peak shape consisting of two components in a 1 : 3 ratio is evident (~398 and ~400 eV). The observed B.E. is consistent with a system that has received some electron density.

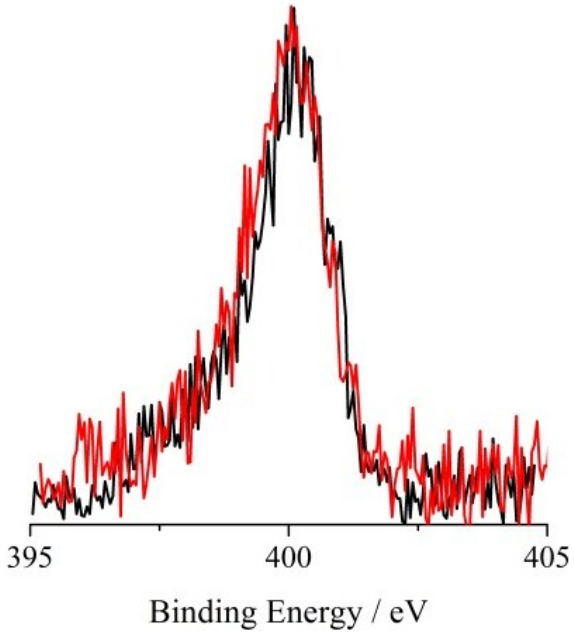

Figure 2.3.3. Al-Kα excited XPS of the H2THPP_SnO_2 (black line) and H2THPP_TiO_2 (red line) in the N 1s binding energy region.

A similar behaviour can be observed for both CuTHPP_TiO_2 and CuTHPP_SnO_2 systems that show Cu 2p states at 934.8 ± 0.1 (Cu $2p_{3/2}$) and 954.6 ± 0.1 eV (Cu $2p_{1/2}$) (Figure 2.3.4), whilst these states in the CuTHPP itself lie at 935.1 and 954.9 eV.

In addition, two well resolved shake-up satellites peaked at 944.0 and 963.8 eV confirm the presence of the different final states upon the ionization of the 2p levels in the open-shell Cu(II) d^9 system. In fact the main peaks correspond to $2p^5 3d^{10}H$ final states, whereas the satellite structures correspond to $2p^5 3d^9$ final states (H denotes a hole on the ligand after a charge-transfer processes). Furthermore, the XPS atomic concentration analyses confirmed for both systems a Cu/N atomic ratio of 0.25 thus excluding any presence of unmetallated porphyrin.

All these observations indicate that both TiO_2 and SnO_2 release electrons to the tetrapyrrole porphyrin core regardless of the fact that it is free base or Cu-complexed.

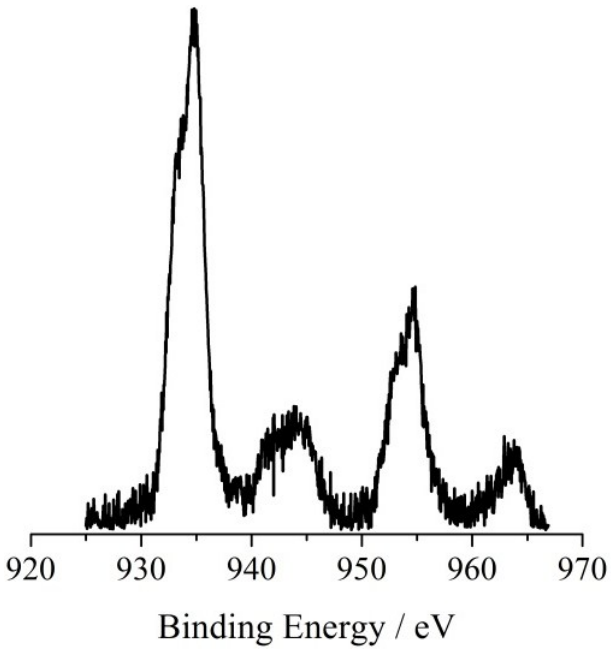

Figure 2.3.4. Al-Kα excited XPS of the CuTHPP_TiO_2 in the Cu 2p binding energy region.

If stoichiometric, both TiO_2 and SnO_2 have filled O 2p-based valence bands and empty Ti 3d or Sn 5s conduction bands. In contrast, native donor defects arising from nonstoichiometry, which in turn are strongly dependent on the synthetic procedure adopted, introduce carriers in the conduction bands.[73] It is recognized that oxygen vacancies (V_o) represent the main kind of defect in both oxides. When any of these n-type semiconductor is exposed to porphyrin molecules, some surface electrons are transferred to the porphyrin molecules as it occurs for oxygen molecules that are captured by the surface electrons and become adsorbed oxygen ions (O^{2-}, O^- and O_2^-). Obviously, the electron affinity of the porphyrin has to be higher than the work function of the oxide.[83] In this case the adsorbed molecules create an electron depletion layer on the oxide grain surface that continues to grow until the Fermi energy of the bands of the porphyrin equals that of the given oxide. Since the depletion layer increases the energy barrier and hence increases the electrical resistance of the given oxide, it is possible to use these semiconductors for sensing by electrical measurements.[78] It is important to note that all the above description applies to

porphyrin molecules in their electronic ground states deposited on semiconducting surfaces.

The FTIR spectra of H2THPP_TiO_2 (Figure 2.3.5a), CuTHPP_TiO_2 (Figure 2.3.5b) and CuTHPP_SnO_2 (Figure 2.3.5c) show the characteristic aromatic stretching (ν_{CH}) at 2856 and 2923-2929 cm^{-1} due to the silane coupling layer, and the ν_{asym} Si-CH_2 mode at 1122-1128 cm^{-1}. Moreover they show all the expected porphyrin bands. In particular, the whole 1100-1230 cm^{-1} region is typical of phenyl and pyrrole group "ring breathings". At 1260-1285 cm^{-1} there is a band due to the C-O-C ether group mode, absent in the H2THPP, that confirms the porphyrin grafting on the substrate surface.[56] The weak signal at 1200 cm^{-1} is typical of the phenolic C-O stretching. Furthermore the C-N stretching mode appears at 1381-1385 cm^{-1}. The weak band in the 1466-1472 cm^{-1} region is assigned to conjugated C-C symmetric stretching, while the intense band observed at 1400-1402 cm^{-1} is consistent with the aromatic O-H stretching. Finally, the band at 1635-1640 cm^{-1} is due to ring stretching of benzene derivatives.

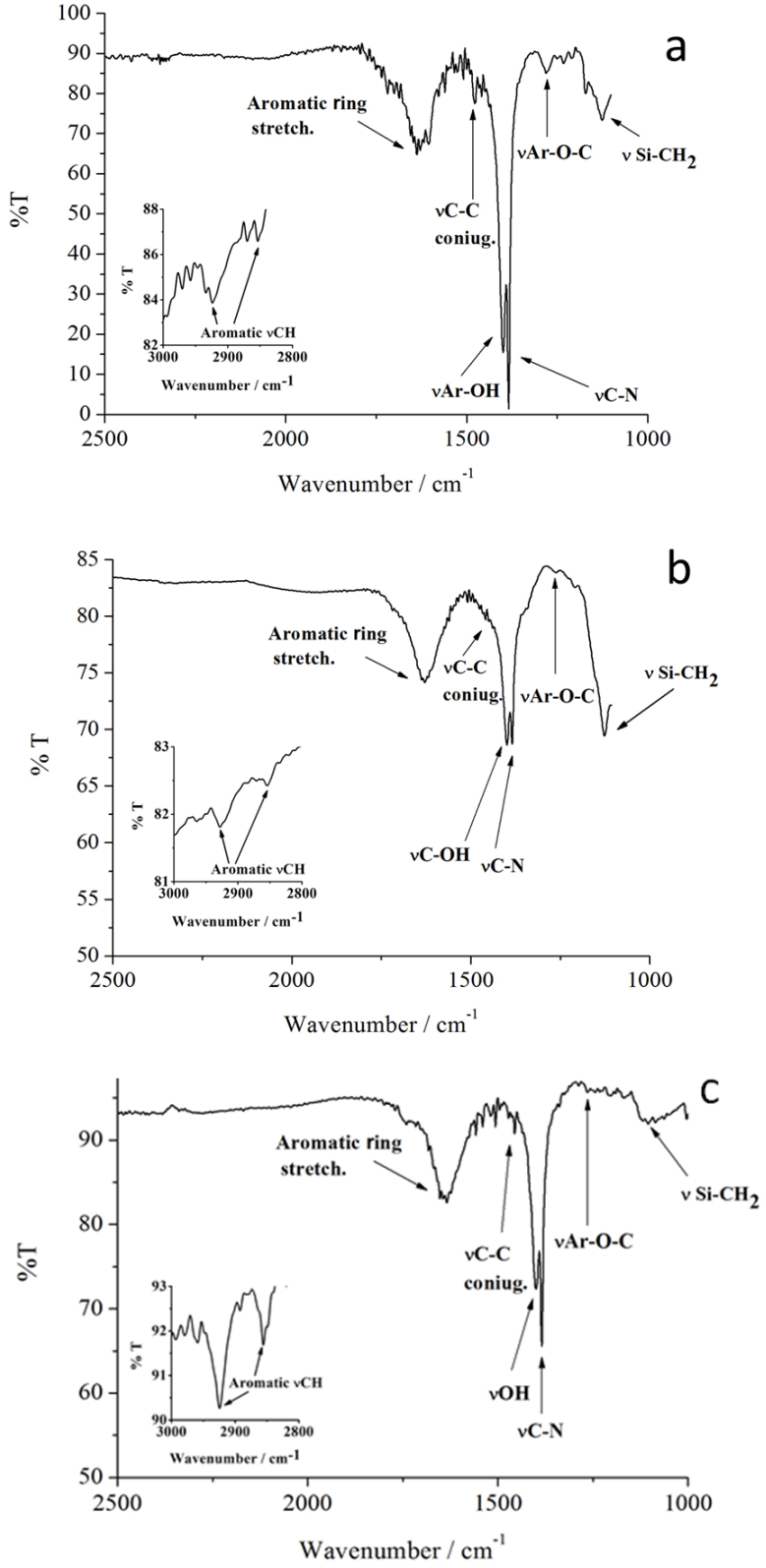

Figure 2.3.5. FTIR spectra of the H2THPP_TiO_2 (a), CuTHPP_TiO_2 (b) and H2THPP_SnO_2 (c) systems.

2.3.3 Properties of Porphyrin Nanostructures on TiO_2 and SnO_2

The optical properties of the synthesized systems were investigated through UV-Vis and luminescence measurements.

All sample weighing for UV-Vis and luminescence measurements were performed using a Mettler Toledo M3 microbalance with 1 μg precision.

Figure 2.3.6 shows the UV-Vis spectra of 0.12 mg (± 1μg) of H2THPP_SnO_2 (black line) and of 0.12 mg of H2THPP_TiO_2 (red line) in 25 mL of N-methyl-2-pyrrolidone (NMP). The Soret bands appear at 425.4 nm for both SnO_2 and TiO_2 oxides with an evident red shift (7.4 nm) with respect to the porphyrin free-base indicative of interactions between the metal oxide and the porphyrin.[56] No UV-Vis evidence of any residual porphyrin was observed in the solutions after the last centrifugation/filtration cycle thus confirming that no unreacted porphyrin was physisorbed on the investigated systems.

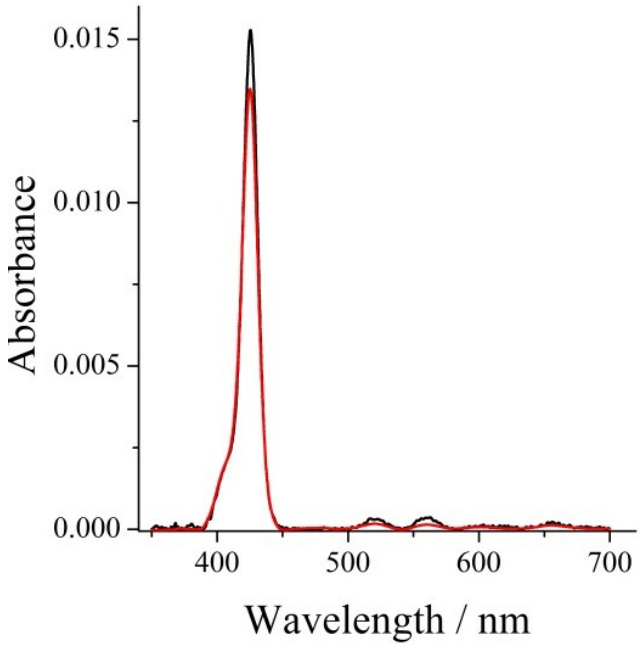

Figure 2.3.6. UV-Vis spectra of 0.12 mg of H2THPP_SnO_2 (black line) and 0.12 mg of H2THPP_TiO_2 (red line) in 25 mL of NMP.

The Brunauer, Emmett, Teller (BET) surface area of SnO_2 (6.9 m^2/g) is smaller

than that of TiO_2 (9 m^2/g) nevertheless it was observed at 425.4 nm a larger absorbance (1.5 x 10^{-2}) for the H2THPP_SnO_2 (vs. 1.3 10^{-2} for the H2THPP_TiO_2). As a consequence, 3.4 x 10^{18} porphyrin molecules/g have been grafted on the H2THPP_SnO_2 (ε of H2THPP = 572200 M^{-1} cm^{-1} at 418.0 nm) while only 3.0 x 10^{18} molecules/g have been grafted on the H2THPP_TiO_2 being their density ratio (3.4 x 10^{18}/3.0 x 10^{18}) = 1.1 (Table 2.3.1).

In order to understand the reason why for the H2THPP_SnO_2 is observed an absorbance larger than that for the H2THPP_TiO_2, nevertheless the surface area of SnO_2 is smaller than that of TiO_2, the powders were microscopically characterised by TEM investigations. TEM micrographs of bare SnO_2 nanoparticles, annealed at 600°C in recrystallised alumina crucibles and sonicated in CH_3CN, reveal a large quantity of spherical particles having a grain size distribution in the 30-60 nm range (Figure 2.3.7A-B)[76,84] and only a few particles show bigger size of about 90 nm.

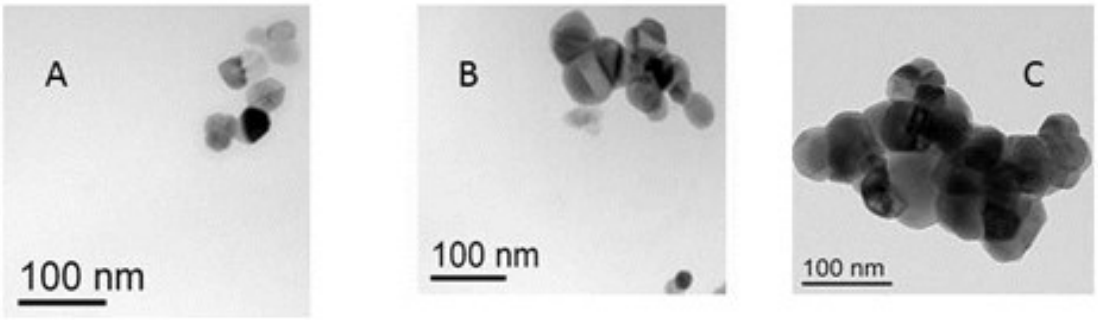

Figure 2.3.7. TEM images of the SnO_2 nanoparticles annealed overnight at 600°C.

The spherical particles are joined each other forming quite linear aggregates having lengths in the 150-300 nm (Figure 2.3.7C). Also the grain surface seems very smooth. Single annealed and sonicated TiO_2 nanoparticles show similar mean sizes of about 30 nm, however in this case they form no linear but bigger and more rounded aggregates, of about 200-400 nm range (Figure 2.3.8A-B).[76, 84] These TiO_2 aggregates are consistent with the anatase phase, as demonstrated by the electron diffraction (Figure 2.3.8C). In particular, the electron diffraction pattern shows several spots lying in circles related to the following plane distances and reflection typical of the anatase phase: 3.52 Å (101), 2.37 Å (004), 2.33 Å (112), 1.89 Å (200), 1.70 Å (105) and 1.67

Å (211).

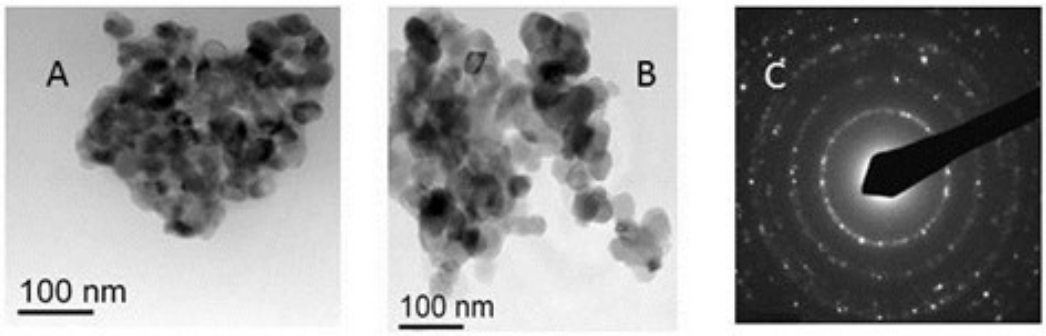

Figure 2.3.8. TEM images (A and B) of the TiO_2 nanoparticles annealed overnight at 600°C. Electron diffraction pattern (C) indicates the presence of the anatase phase.

Therefore, TEM analysis can give a rationale for the UV-Vis results. In fact, the TiO_2 grains tend to agglomerate in a more pronounced way with respect to SnO_2 crystal grains thus reducing the surface available for porphyrin functionalization.

Figure 2.3.9 shows the UV-Vis spectra of 0.12 mg of CuTHPP_SnO_2 (black line) and of 0.12 mg of CuTHPP_TiO_2_(red line) in 25 mL of NMP.[85] The Soret bands appear at 424.0 and 423.4 nm for the SnO_2 and TiO_2 systems, respectively with evident red shifts (6.0 and 5.4 nm, respectively) with respect to the Cu-porphyrin complex. Also in this case it was observed for the CuTHPP_SnO_2 an absorbance (4.1 x 10^{-3}) (ε of CuTHPP = 155500 M^{-1} cm^{-1} at 418 nm) larger than that for the CuTHPP_TiO_2 (3.0 x 10^{-3}). As a consequence, 3.2 x 10^{18} molecules/g have been grafted on the CuTHPP_SnO_2 while only 2.4 x 10^{18} molecules/g have been grafted on the CuTHPP_TiO_2. From these observation it emerges that the ratio between the number of porphyrin molecules/g and the number of Cu-complexed porphyrin molecules/g grafted on TiO_2 is 3.0 x 10^{18}/2.4 x 10^{18} = 1.3. Noteworthy, also the ratio between the number of porphyrin molecules/g and the number of Cu-complexed porphyrin molecules/g grafted on SnO_2 is similar to the above value being 3.4 x 10^{18}/3.2 x 10^{18} = 1.1. It is clear that there must be a mechanism that increases the footprint of the Cu-complexed porphyrin molecules on oxide surfaces and, in a very close system; this behaviour was interpreted in terms of increased face-to-face

repulsions between porphyrin molecules due to the presence of Cu^{++} ions in the porphyrin core. In this case the ratio of the CuTHPP molecules/g grafted on SnO_2 / the CuTHPP molecules/g grafted on TiO_2 (3.2 x 10^{18} molecules/g) / (2.4 x 10^{18} molecules/g) is 1.4 and this is justified by a tendency of TiO_2 grains to agglomerate more than the SnO_2 crystal grains.

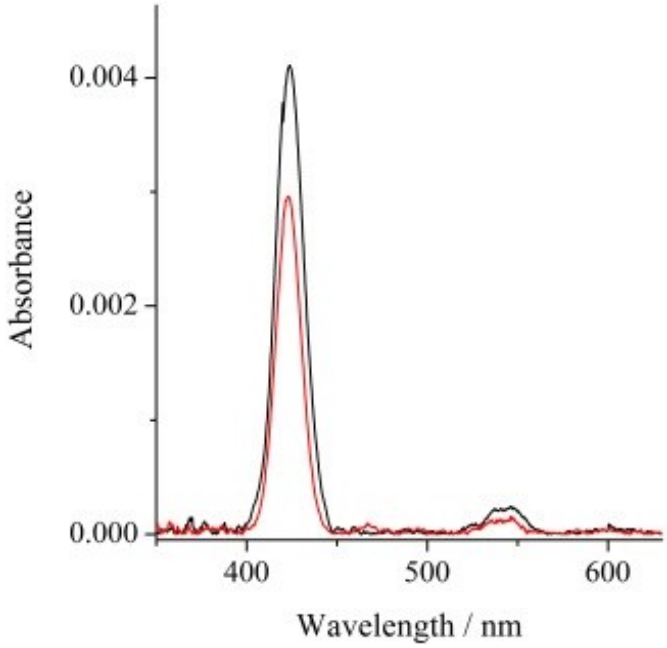

Figure 2.3.9. UV-Vis spectra of 0.12 mg of CuTHPP_SnO_2 (black line) and of 0.12 mg of CuTHPP_TiO_2 (red line) in 25 mL of NMP.

Figure 2.3.10 shows the luminescence spectra of H2THPP_SnO_2 and of H2THPP_TiO_2. The H2THPP_SnO_2 luminescence (black line) is less intense than that observed for the H2THPP_TiO_2 (red line) (I_{Ti}/I_{Sn} = 1.2, where I_{Ti} and I_{Sn} refer to the luminescence intensity observed at 654.0 nm for 0.12 mg of H2THPP_TiO_2 and 0.12 mg of H2THPP_SnO_2, respectively in 25 mL of CH_3CN), whilst the absorbances showed an opposite trend (Figure 2.3.6). In practice there is a larger number of porphyrin molecules/g grafted on SnO_2, as evidenced by the UV-Vis measurements, but in the same time there is a less intense porphyrin luminescence.

This behaviour is further evident in the case of CuTHPP_SnO_2 and of CuTHPP_TiO_2 being the I_{Ti}/I_{Sn} = 1.9 (Figure 2.3.11) and reveals the role of central metal ions, that affect the overall porphyrin energetics, in the electron transfer

processes.[86]

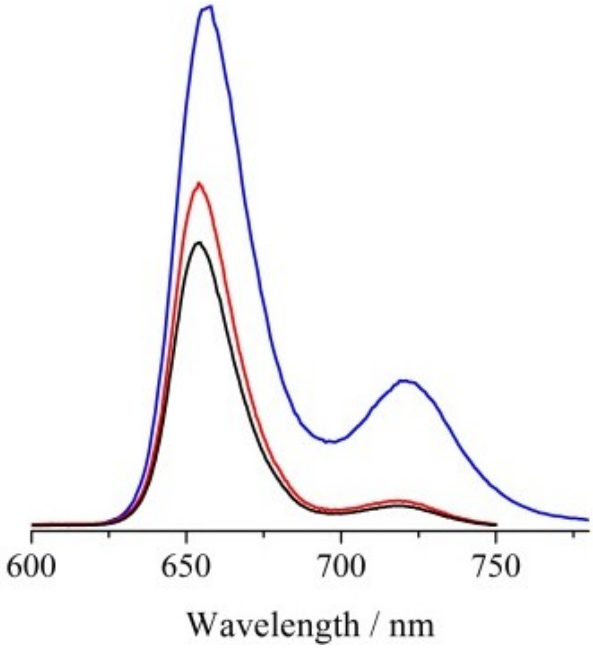

Figure 2.3.10. Luminescence spectra of 0.12 mg of H2THPP_SnO_2 (black line), of 0.12 mg of H2THPP_TiO_2 (red line) in 25 mL of CH_3CN (λ_{exc} = 418 nm) and of a CH_3CN solution of H2THPP (blue line) containing a number of porphyrin molecules identical to that found in H2THPP_TiO_2 (2.39 x 10^{-8} M, Table 2.3.1).

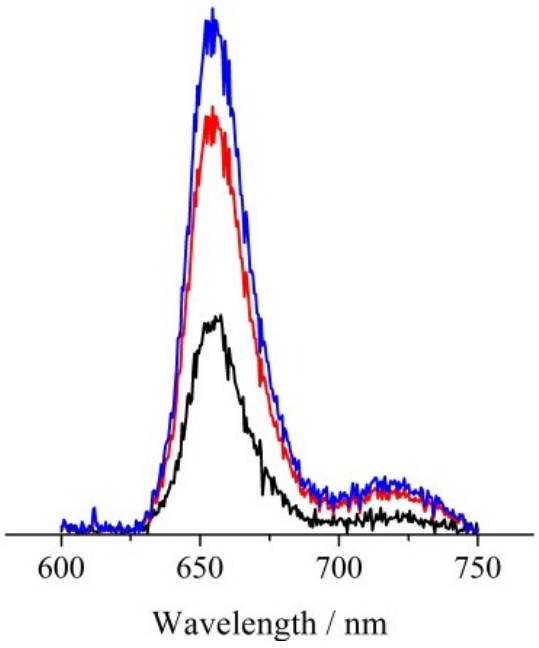

Figure 2.3.11. Luminescence spectra of 0.12 mg of CuTHPP_SnO_2 (black line), of 0.12 mg of CuTHPP_TiO_2 (red line) in 25 mL of CH_3CN (λ_{exc} = 418 nm) and of a CH_3CN solution of CuTHPP (blue line) containing a number of Cu-porphyrin molecules identical to that found in CuTHPP_TiO_2 (1.91 x 10^{-8} M, Table 2.3.1).

In fact there is a relevant decrease in the luminescence intensity of the CuTHPP_SnO_2 as compared with the TiO_2 analogue or, even better, with the luminescence observed for a CuTHPP solution having the same concentration in porphyrin molecules. This is an evidence of the fact that Cu modifies the oxidation potential (or LUMO) of the dye. It was already noted that XPS had excluded any presence of unmetallated porphyrin on these systems.

In this context, the observed less intense porphyrin or Cu(II) porphyrin luminescence on the SnO_2 substrate cannot be ascribed to a quenching effect due to porphyrin stacking interaction since in all cases the observed porphyrin or Cu-porphyrin footprints (Table 2.3.1) are large enough to rule out stacking effects.

Table 2.3.1. Number of grafted molecules/g and molecule footprint.

System	N° molecules / g	Mol / L	Footprint Å^2
H2THPP_TiO_2	3.0×10^{18}	2.39×10^{-8}	300
H2THPP_SnO_2	3.4×10^{18}	2.71×10^{-8}	205
CuTHPP_TiO_2	2.4×10^{18}	1.91×10^{-8}	375
CuTHPP_SnO_2	3.2×10^{18}	2.55×10^{-8}	219

The observed luminescence intensity trend can find an explanation by considering that the conduction band of the SnO_2 is mainly Sn 5s in character and that of TiO_2 is represented by the Ti 3d levels. In the simple metals the B.E. of the Sn 5s states is about 12 eV while the B.E. of the Ti 3d states is about 8 eV. In addition, also the Pauling electronegativity of Sn (1.8) is larger than that of Ti (1.5). Therefore, simple native chemical intuition suggests that the Sn 5s levels lie at lower (more negative) energy than the Ti 3d and, as a consequence, electron injection should be easier towards SnO_2 than towards TiO_2. This observation finds a support in the recent study of Brudvig and Schmuttenmaer who, using time resolved terahertz spectroscopy, investigated the energy levels and the photoexcited electron injection dynamics of some porphyrins and Cu-porphyrins bound to TiO_2 and SnO_2 nanoparticles and arrived at the same conclusion.[83] Generally, inclusion of copper into the porphyrin structure

enhances intersystem crossing into the triplet state thus lowering the singlet emission. A triplet state is unlikely to lead to electron injection into the TiO_2/SnO_2 nanoparticles. In fact there is a definite decrease in the emission intensity on going from the porphyrin free-base to the copper complex. In the studied systems it was evidenced a significant decrease in the luminescence intensity on passing from the porphyrin free base or Cu-porphyrin complex to their related covalently assembled monolayers on TiO_2 or SnO_2. This is an evidence of how important may be that the first layer of the dye is covalently assembled on the semiconducting oxide surfaces instead of to simple be physisorbed.[87-89] To resume, porphyrins in the excited states inject electrons into conduction bands of the TiO_2 and SnO_2 nanoparticles and, the larger electron injection the lower luminescence intensity.

As a control check of the above observation it was measured the luminescence spectrum of a sample of CuTHPP physisorbed on SnO_2 (CuTHPP-SnO_2) in absence of the coupling agent, obtained using the same treatments and reaction conditions reported above for the covalent assembly, apart the experiments involving the formation of a silane coupling layer (Figure 2.3.12).

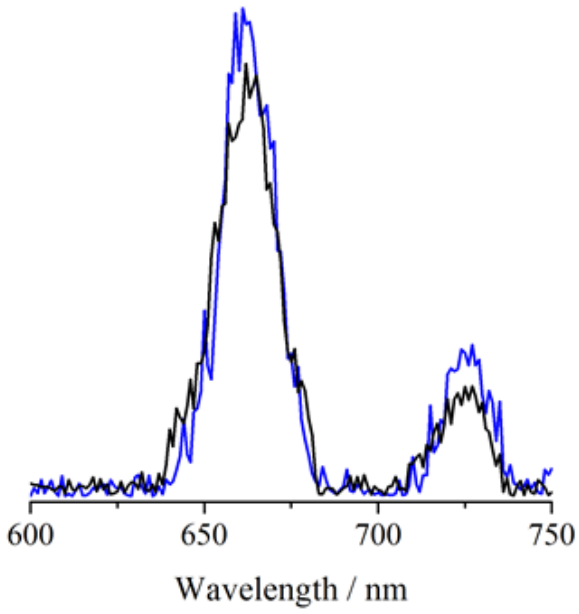

Figure 2.3.12. Luminescence spectra of 0.14 mg of CuTHPP-SnO_2 (black line) in 25 mL of CH_3CN (λ_{exc} = 418 nm) and of a CH_3CN solution of CuTHPP (blue line) containing a number of Cu-porphyrin molecules identical to that found in CuTHPP-SnO_2 (2.96 x 10^{-8} M).

This final suspension was subjected to cycles of sonication/centrifugation-filtration until the UV-Vis absorbance of 0.14 mg of CuTHPP-SnO_2 in 25 mL of NMP was similar to that obtained for the covalent parent system. The related luminescence spectrum (Figure 2.3.12, black line) was compared with a CH_3CN solution of CuTHPP (Figure 2.3.12, blue line) containing a number of Cu-porphyrin molecules identical to that found in CuTHPP-SnO_2. It emerged that the luminescence intensity decrease of CuTHPP-SnO_2 is much less pronounced with respect to the covalent system indicative of a smaller electron-injection effect. This is a further indication of the importance of the covalently assembly for the electron injection.

All the above observation confirm that electron injection is more efficient in systems where the molecular dye is covalently anchored to the TCO with respect to those where the dye is just physisorbed.

Conclusions

In this chapter it was shown how the *bottom-up* approach is useful to synthesise nanomaterials using discrete molecules as building blocks. Moreover, the silane coupling agent allowed obtaining stable and robust covalent assemblies with high degree of order useful for their integration in devices.

In particular, the functionalization of the Si(100) surface allowed the generation of ordered porphyrin assemblies in the micrometre range, covalently bound to the silicon surfaces.

Then it was exploited the ability of a porphyrin monolayer to communicate with copper(II) solutions. In fact this porphyrin architecture exhibits many optically active states that can be optically readout. By coupling the optical output with the calculated distribution diagram it was possible to detect the physical states of the overall system that, in turn, represent the answer (output) to the chemical Cu(II) stimulus. At least three different states have been safely distinguished. The response time of the setup is short (4 min) and this archetypal could represent the platform for the development of advanced interfacial communication systems based on optically active monolayers. In fact the distinct optical states of the present system are of interest for permanent memory storage devices. Worthy of note this study also reported on the first evaluation of the stability constant for the complexation reaction between a covalent porphyrin monolayer and Cu(II).

In the third part of the study the donor–acceptor properties between the porphyrin monolayers and some metal oxides were investigated by means of their optical properties. Specifically monolayers of a free-base porphyrin or its copper complex covalently assembled on TiO_2 and SnO_2 nanocrystals were fabricated. The electron injection from these dyes into the conduction bands of the semiconducting metal oxides resulted in an evident decrease of the related luminescence. Indeed the electron injection occurs mainly via chemical bonds since porphyrins are covalently assembled

on the oxide surfaces and through-bond electron interactions dominate. The overall results are consistent with the convenience of the present systems for the DSSC technology.

In summary we have demonstrated the large flexibility of porphyrin-based nanostructures that can be useful for different applications in nanotechnology.

References

[1] W. Auwärter, K. Seufert, F. Bischoff, D. Ecija, S. Vijayaraghavan, S. Joshi, F Klappenberger, N. Samudrala and J. V. Barth, *Nat. Nanotechnol.* **2012**, 7, 41.

[2] A. Gulino, S. Bazzano, P. Mineo, E. Scamporrino, D. Vitalini, I. Fragalà, *Chem. Mater.* **2005,** *17,* 521-526.

[3] 1) J. S. Lindsey and D. F. Bocian, *Acc. Chem. Res.*, **2011**, 44, 638.

[9] Barea, E. M.; Bisquert, J. *Langmuir* **2013**, *29*, 8773-8781.

[5] Jang, J. K.; Park, S. H.; Kim, C.; Ko, J.; Seo, W. S.; Song H.; Park, J. T. *Nanotechnology* **2011**, *22*, 275720.

[6] Cheng, Y. -J.; Cao, F. -Y.; Lin, W. -C.; Chen C. -H.; Hsieh, C. -H. *Chem. Mater.* **2011**, *23*, 1512-1518.

[7] Zhan, C.; Maitani, M. M.; Mochizuki, D.; Suzuki E.; Wada, Y. *Chem. Lett.*, **2012**, *41*, 423-424.

[8] Moore, G. F.; Konezny, S. J.; Song, H. -e.; Milot, L.; Blakemore, J. D.; Lee, M. L.; Batista, V. S.; Schmuttenmaer, C. A.; Crabtree R. H.; Brudvig, G. W. *J. Phys. Chem. C* **2012**, *116*, 4892-4902.

[9] Wagner, K.; Griffith, M. J.; James, M.; Mozer, A. J.; Wagner, P.; Triani, G.; Officer D. L.; Wallace, G. G. *J. Phys. Chem. C* **2011**, *115*, 317-326.

[10] Lu, H. -P.; Tsai, C. -Y.; Yen, W. -N.; Hsieh, C. -P.; Lee, C. -W.; Yeh, C. -Y.; Diau, E. W. -G. *J. Phys. Chem. C* **2009**, *113*, 20990-20997.

[11] Lee C. Y.; Hupp, J. T. *Langmuir* **2010**, *26*, 3760-3765.

[12] Nobukuni, H.; Shimazaki, Y.; Uno, H.; Naruta, Y.; Ohkubo, K.; Kojima, T.; Fukuzumi,
S.; Seki, S.; Sakai, H.; Hasobe T.; Tani, F. *Chem. Eur. J.* **2010**, *16*, 11611-11623.

[13] Ohtani, M.; Kamat P. V.; Fukuzumi, S. *J. Mater. Chem*. **2010**, *20*, 582-587.

[14] Saarenp, H.; Sariola-Leikas, E.; Pyymaki Perros, A.; Kontio, J. M.; Efimov, A.; Hayashi, H.; Lipsanen, H.; Imahori, H.; Lemmetyinen, H.; Tkachenko, N. V. *J. Phys. Chem. C* **2012**, *116*, 2336-2343.

[15] D. A. Cristaldi, A. Motta, S. Millesi, T. Gupta, M. Chhatwal, A.Gulino, *J.Mater. Chem. C: Materials for Optical and Electronic Devices*, **2013**, 1, 4979.

[16] A. Gulino, P. Mineo, E. Scamporrino, D. Vitalini and I. Fragalà, *Chem. Mater.*, **2004**, 16, 1838.

[17] J. M. Gottfried, K. Flechtner, A. Kretschmann, T. Lukasczyk and H.-P. Steinr¨uck, *J. Am. Chem. Soc.*, **2006**, 128, 5644–5645.

[18] A. Ghosh, J. Moulder, M. Br¨oring and E. Vogel, *Angew. Chem., Int. Ed.*, **2001**, 40, 431–434.

[19] R. Kaminker, L. Motiei, A. Gulino, I. Fragalà, L. J. W. Shimon, G. Evmenenko, P. Dutta, M. A. Iron and M. E. van der Boom, *J. Am. Chem. Soc.*, **2010**, 132, 14554.

[20] J. Choudhury, R. Kaminker, L. Motiei, G. de Ruiter, M. Morozov, F. Lupo, A. Gulino and M. E. van der Boom, *J. Am. Chem. Soc.*, **2010**, 132, 9295.

[21] L. Motiei, M. Altman, T. Gupta, F. Lupo, A. Gulino, G. Evmenenko, P. Dutta and M. E. van der Boom, *J. Am. Chem. Soc.*, **2008**, 130, 8913.

[22] D. A. Cristaldi, I. Fragalà, A. Pappalardo, R. M. Toscano, F. P. Ballistreri, G. A. Tomaselli and A. Gulino, *J. Mater. Chem.*, **2012**, 22, 675.

[23] F. Lupo, C. Capici, G. Gattuso, A. Notti, M. F. Parisi, A. Pappalardo, S. Pappalardo and A. Gulino, *Chem. Mater.*, **2010**, 22, 2829.

[24] S. L. Brandow, M. S. Chen, C. S. Dulcey and W. J. Dressick, *Langmuir*, **2008**, 24, 3888.

[25] A. Gulino, S. Giuffrida, P. Mineo, M. Purrazzo, E. Scamporrino, G. Ventimiglia, M. E. van der Boom and I. Fragalà, *J. Phys. Chem. B*, **2006**, 110, 16781.

[26] J. P. Perdew, K. Burke and M. Ernzerhof, *Phys. Rev. Lett.*, **1996**, 77, 3865.

[27] V. A. Rassolov, J. A. Pople, M. A. Ratner and T. L. Windus, *J. Chem. Phys.*, **1998**, 109, 1223.

[28] Gaussian 09, Revision A.1, M. J. Frisch, G. W. Trucks, H. B. Schlegel, G. E. Scuseria, M. A. Robb, J. R. Cheeseman, G. Scalmani, V. Barone, B. Mennucci, G. A. Petersson, H. Nakatsuji, M. Caricato, X. Li, H. P. Hratchian, A. F. Izmaylov, J. Bloino, G. Zheng, J. L. Sonnenberg, M. Hada, M. Ehara, K. Toyota, R. Fukuda, J. Hasegawa, M. Ishida, T. Nakajima, Y. Honda, O. Kitao, H. Nakai, T. Vreven, J. A. Montgomery, Jr., J. E. Peralta, F. Ogliaro, M. Bearpark, J. J. Heyd, E. Brothers, K. N. Kudin, V. N. Staroverov, R. Kobayashi, J. Normand, K. Raghavachari, A. Rendell, J. C. Burant, S. S. Iyengar, J. Tomasi, M. Cossi, N. Rega, J. M. Millam, M. Klene, J. E. Knox, J. B. Cross, V. Bakken, C. Adamo, J. Jaramillo, R. Gomperts, R. E. Stratmann, O. Yazyev, A. J. Austin, R. Cammi, C. Pomelli, J. W. Ochterski, R. L. Martin, K. Morokuma, V. G. Zakrzewski, G. A. Voth, P. Salvador, J. J. Dannenberg, S. Dapprich, A. D. Daniels,

Ö. Farkas, J. B. Foresman, J. V. Ortiz, J. Cioslowski, and D. J. Fox, Gaussian, Inc., Wallingford CT, 2009.

[29] A. Gulino, F. Lupo, G. G. Condorelli, P. Mineo and I. Fragalà, *Chem. Mater.*, **2007**, 19, 5102.

[30] A. Gulino, P. Mineo, E. Scamporrino, D. Vitalini and I. Fragalà, *Chem. Mater.*, **2006**, 18, 2404.

[31] R. L. Cicero, C. E. D. Chidsey, G. P. Lopinski, D. D. M. Wayner and R. A. Wolkow, *Langmuir*, **2002**, 18, 305.

[32] G. P. Lopinski, D. D. M. Wayner and R. A. Wolkow, *Nature*, **2000**, 406, 48.

[33] P. G. Mineo, D. A. Cristaldi, A. Motta, T. Gupta and A. Gulino, *RSC Adv.*, **2013**, 3, 1137.

[34] P. Mineo, A. Motta, F. Lupo, L. Renna and A. Gulino, *J. Phys. Chem. C*, **2011**, 115, 12293.

[35] L. A. Fendt, M. Stoehr, N. Wintjes, M. Enache, T. A. Jung and F. Diederich, *Chem.–Eur. J.*, **2009**, 15, 11139.

[36] J. Otsuki, E. Nagamine, T. Kondo, K. Iwasaki, M. Asakawa and K. Miyake, *J. Am. Chem. Soc.*, **2005**, 127, 10400.

[37] W. Lin, W. Lin, G. K. Wong and T. J. Marks, *J. Am. Chem. Soc.*, **1996**, 118, 8034.

[38] A. Gulino, G. G. Condorelli, P. Mineo and I. Fragalà, *Nanotechnology*, **2005**, 16, 2170.

[39] Millesi, S.; Maccarrone, G.; Gulino, A. *PhysChemChemPhys* **2015**, *17*, 6612-6617.

[40] M. Mazur and G. J. Blanchard, *J. Phys. Chem. B*, **2005**, 109, 4076–4083.

[41] D. Zigah, C. Herrier, L. Scheres, M. Giesbers, B. Fabre, P. Hapiot and H. Zuilhof, *Angew. Chem., Int. Ed.*, **2010**, 49, 3157–3160.

[42] B. Fabre, Y. Li, L. Scheres, S. P. Pujari and H. Zuilhof, *Angew. Chem., Int. Ed.*, **2013**, 52, 12024–12027.

[43] T. Gupta and M. E. van der Boom, *Angew. Chem., Int. Ed.*, **2008**, 47, 2260–2262.

[44] S. Rubin, J. T. Chow, J. P. Ferraris and T. A. Zawodzinski, *Langmuir*, **1996**, 12, 363–370.

[45] M. Turesson, T. Aakesson and J. Forsman, *Langmuir*, **2007**, 23, 9555–9558.

[46] J. Rebek and F. Gavina, *J. Am. Chem. Soc.*, **1974**, 96, 7112–7114.

[47] Q. Feng, T. K. Park and J. Rebek, *Science*, **1992**, 256, 1179–1180.

[48] J. Rebek, *Science*, **1987**, 235, 1478–1484.

[49] Y. Wu, K. Liu, B. Su and L. Jiang, *Adv. Mater.*, **2014**, 26, 1124–1128.

[50] M. Semeraro, M. Baroncini and A. Credi, *Molecular and Supramolecular Information Processing: From Molecular Switches to Logic Systems*, 2012, p. 25–52.

[51] R. Guliyev, S. Ozturk, Z. Kostereli and E. U. Akkaya, *Angew. Chem., Int. Ed.*, **2011**, 50, 9826–9831.

[52] M. Biancardo, C. Bignozzi, H. Doyle and G. Redmond, *Chem. Commun.*, **2005**, 3918–3920.

[53] A. P. de Silva, *Nature*, **2008**, 454, 417–418.

[54] C. Haensch, S. Hoeppener and U. S. Schubert, *Chem. Soc. Rev.*, **2010**, 39, 2323–2334.

[55] P. Oliveri, G. Maccarrone and S. Di Bella, *J. Org. Chem.*, **2011**, 76, 8879–8884.

[56] D. A. Cristaldi and A. Gulino, *ChemSusChem*, **2013**, 6, 1031–1036.

[57] A. Sabatini, A. Vacca and P. Gans, Coord. *Chem. Rev.*, **1992**, 120, 389–405.

[58] P. Gans, A. Sabatini and A. Vacca, *Talanta*, **1996**, 43, 1739–1753.

[59] www.hyperquad.co.uk/hq2000.htm.

[60] G. Arena, A. Contino, G. Maccarrone, D. Sciotto and C. Sgarlata, *Tetrahedron Lett*., **2007**, 48, 8274–8276.

[61] D. Q. Li, B. I. Swanson, J. M. Robinson and M. A. Hoffbauer, *J. Am. Chem. Soc.*, **1993**, 115, 6975–6980.

[62] H. R. Jimènez, M. Julve and J. Faus, J. Chem. Soc., *Dalton Trans*, 1991, 1945–1949.

[63] A. M. J Devoille, P. Richardson, N. L. Bill, J. L. Sessler and J. B. Love, *Inorg. Chem.*, **2011**, 50, 3116–3126.

[64] L. Alderighi, P. Gans, A. Ienco, D. Peters, A. Sabatini and A. Vacca, *Coord. Chem. Rev.*, **1999**, 184, 311–318.

[65] S. Millesi, R. Lo Nigro, M. Pedroni, A. Speghini, A. Gulino, *J. Phys. Chem. C*, **2015**, *119*, 23743-23751.

[66] Klajn, R.; Stoddart, J. F.; Grzybowski, B. A. *Chem. Soc. Rev.* **2010**, *39*, 2203-2237.

[67] Graetzel, M.; Janssen, R. A. J.; Mitzi, D. B.; Sargent, E. H. *Nature* **2012**, *488*, 304-312.

[68] Chen, X.; Li, C.; Graetzel, M.; Kostecki, R.; Mao, S. S. *Chem. Soc. Rev*. **2012**, *41*, 7909-7937.

[69] Das, S. K.; Sandanayaka, A. S. D.; Subbaiyan, N. K.; Zandler, M. E.; Ito, O.; D'Souza, F. *Chem. Eur. J.* **2012**, *18*, 11388-11398.

[70] Pagona, G.; Zervaki, G. E.; Sandanayaka, A. S. D.; Ito, O.; Charalambidis, G.; Hasobe, T.; Coutsolelos A. G.; Tagmatarchis, N. *J. Phys. Chem. C* **2012**, *116*, 9439-9449.

[71] Vizuete, M.; Gomez-Escalonilla, M. J.; Fierro, J. L. G.; Sandanayaka, A. S. D.; Hasobe, T.; Yudasaka, M.; Iijima, S.; Ito, O; Langa, F. *Chem. Eur. J.* **2010**, *16*, 10752-10763.

[72] Umeyama, T.; Mihara, J.; Tezuka, N.; Matano, Y.; Stranius, K.; Chukharev, V.; Tkachenko, N. V.; Lemmetyinen, H.; Noda, K.; Matsushige, K.; Shishido, T.; Liu, Z.; Hirose-Takai, K.; Suenaga K.; Imahori, H. *Chem. Eur. J.* **2012**, *18*, 4250-4257.

[73] Taverner, A. E.; Rayden, C.; Warren, S.; Gulino, A.; Cox, P. A.; Egdell, R. G. Comparison of the Energies of Vanadium Donor Levels in Doped SnO_2 and TiO_2. *Phys. Rev. B*, **1995**, *51*, 6833-6837.

[74] Chen, H. -Y.; Kuang, D. -B.; Su, C. -Y. *J. Mater. Chem.* **2012**, *22*, 15475-15489.

[75] Panda, D. K.; Goodson, F. S.; Ray, S.; Lowell R.; Saha, S. *Chem. Commun*. **2012**, *48*, 8775-8777.

[76] Joshi R. K.; Schneider, J. J. *Chem. Soc. Rev*. **2012**, *41*, 5285-5312.

[77] Baik, J. M.; Zielke, M.; Kim, M. H.; Turner, K. L.; Wodtke, A. M .; Moskovits, M. *ACS NANO* **2010**, *4*, 3117-3122.

[78] Klenov, K. D. O.; Lilach, Y.; Stemmer, S.; Moskovits, M. *NANO LETT.* **2005**, *5*, 667-673.

[79] Millesi, S; Gulino, A. *J. Mater. Chem. C* **2014**, *2*, 5924-5930.

[80] de Ruiter, G.; van der Boom, M. E. *Angew. Chem*. **2012**, *124*, 8726 –8729; *Angew. Chem. Int. Ed*., **2012**, *51,* 8598-8601.

[81] Di Benedetto, S. A.; Facchetti, A.; Ratner M. A.; Marks, T. J. *Adv. Mater*. **2009**, *21*, 1407-1433.

[82] Ding L.; Fang, Y. *Chem. Soc. Rev*. **2010**, *39*, 4258-4273.

[83] Milot, R. L.; Moore, G. F.; Crabtree, R. H.; Brudvig, G. W.; Schmuttenmaer, C. A. *J. Phys. Chem. C* **2013**, *117*, 21662-21670.

[84] Jun, Y. -w.; Choi, J. -s.; Cheon, J. *Angew. Chem. Int. Ed*. **2006**, *45*, 3414-3439.

[85] Lu, G.; Zhang, X.; Cai, X.; Jiang, J. *J. Mater. Chem*. **2009**, *19*, 2417-2424.

[86] Sardar, S.; Sarkar, S.; Myint, M. T. Z.; Al-Harthi, S.; Dutta, J.; Pal, S. K. *Phys. Chem. Chem. Phys.* **2013**, *15*, 18562-18570.

[87] Leem, G.; Morseth, Z. A.; Puodziukynaite, E.; Jiang, J.; Fang, Z.; Gilligan, A. T.; Reynolds, J. R.; Papanikolas, J. M.; Schanze, K. S. *J. Phys. Chem. C* **2014**, *118*, 28535-28541.

[88] Schuetz, R.; Malhotra, S.; Thomas, I.; Strothkaemper, C.; Bartelt, A.; Schwarzburg, K.; Hannappel, T.; Fasting, C.; Eichberger, R. *J. Phys. Chem. C* **2014**, *118*, 9336-9345.

[89] Natali, M.; Ravaglia, M.; Scandola, F.; Boixel, J.; Pellegrin, Y.; Blart, E.; Odobel, F. *J. Phys. Chem. C* **2013**, *117*, 19334−19345.

Chapter 3

Interacting Luminescent Nanostructures

The combination of particular properties of different chemical entities is a methodological challenge that often generates enhanced effects useful to enlarge the range of applications in material science.[1] Excellent examples are represented by some magnetic nanoparticles covered with organic monolayers useful for active drug targeting, hyper thermic treatment, bio-separation, diagnosis and detoxification of biological fluids;[2] proteins and carbon nanotube hybrids for medical, nanotechnology, and materials science applications;[3] graphene materials for electronic transport;[4] DNA/nanoparticle hybrid systems for controlled delivery of drugs;[5] fluorescent, magnetic and plasmonic-hybrid multifunctional colloidal nano objects for advances properties, etc..[1]

In the previous chapter we focused the attention on porphyrin nanostructures useful for optoelectronic applications. Other important luminescent systems are lanthanide complexes. In fact, lanthanides have exceptional luminescent characteristics such as high luminous intensity, long fluorescence lifetime, large Stokes shifts and sharp emission profiles from the f−f electron transitions which make them useful in fluorescence, DNA hybridization, cell activity, bioimaging assays etc..[6-12] Moreover, taking into account that lanthanide complexes conjugated to polymers matrices improve their thermal and mechanical stabilities[13-15] and that photoluminescence of lanthanide ions upon ultraviolet light irradiation is strongly influenced by their chemical environment,[16] we implemented on solid surfaces different luminescent nanostructures all of them covalently bound on appropriated substrates.

Specifically we performed the implementation of an europium(III) complex monolayer on polystyrene films, in turn covalently bound on Si(100). Afterward, we studied the mutual interaction of a porphyrin monolayer combined with a Eu-complex. Finally, it was synthesized an Y-complex as a new potential building-block for application in luminescent nanostructures.

3.1 Europium(III) on Si(100) Engineered with Covalent Polystyrene Nanostructures

Lanthanide complexes embedded in polymeric matrices have unique luminescent properties and polymers are regarded as appropriate hosts for flexible, large area displays and light-emitting diodes.[17] The polymers typically used in this field are polymethylmetacrylate (PMMA), polyvinylalcohol (PVA), polyethylene (PE), polystyrene (PS) and fluorinated polymers (for IR luminescence). Polymer matrices (photoactive and photoinert) play different roles in photoluminescence.[18] E.g., the presence of benzene substituents in the polymer chains influences the photoluminescence intensity of lanthanides, and values three times larger than those observed for lanthanides embedded in polymer matrices with no benzene groups have been observed.[18] Thus, the polystyrene seems one of the best polymers to conjugate lanthanides. Moreover, covalent-assembled polymeric films, grown perpendicular to the silicon surface by a *bottom-up* approach, offer significant advantages to control both chain length and concentration of functional groups.[19-21]

In this context, we fabricated a monolayer of the tris(dibenzoylmethane) mono(5-amino-1,10-phenanthroline)europium(III) complex molecules, $Eu(dbm)_3$-phen, (Figure 3.1.1) bound to a polymeric film, in turn grown on a flat substrate.

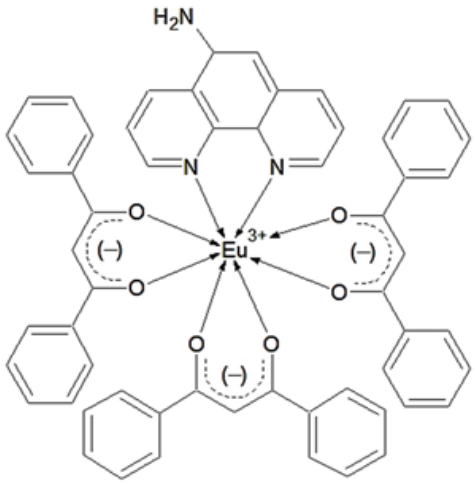

Figure 3.1.1. Structure of the tris(dibenzoylmethane) mono(5-amino-1,10-phenanthroline)europium(III) complex.

In particular, silanized Si(100) and quartz substrates were chosen for the growth of a film of self-assembled polystyrene (SA_PSS). The surface bound styrene chloride serves for anchoring of the Eu(III) complex (SA_PSS_Eu).[22]

3.1.1 Synthesis of an Eu(III) Complex on Polystyrene Nanostructures

After silanization of Si(100), an atom transfer radical polymerization (ATRP) reaction of PS, mediated by a Cu^{+} catalyst, was performed on the Si(100) surface (Scheme 3.1.1). In particular, polystyrene structures were obtained by an optimized redox reaction between the benzyl chloride functionality of the silane and the Cu^{+} catalyst to produce Cu^{++}, reduction of the $Cl^{\bullet}$ radical to Cl^{-} anion (due to homolytic fragmentation of the C-Cl bond) and formation of the surface-bound benzyl radical.[23-24] Afterward, the benzyl radical reacts with the styrene monomer to form the surface-bound styrene radical that, in turn, reacted with the Cu^{++} to return the starting Cu^{+} catalyst and the surface bound styrene chloride (Scheme 3.1.1).[23-24] With the cycling of this reaction pathway, polystyrene structures grow-up covalently bound to the Si(100). After two hours of reaction, SA_PSS systems were washed and sonicated in NMP and THF to remove any residual physisorbed material, loaded into glass pressure vessels under N_2, immersed in a fresh prepared 1.5 x 10^{-3} M toluene solution of the $Eu(dbm)_3$-phen and heated-up to 90°C for 72 h. During this step the surface bound styrene chloride reacts with the amine substituent of the phenanthroline ligand thus allowing additional functionalization with the Eu complex to give $Eu(dbm)_3$-phen monolayer bound to the silanized surface. The functionalised substrates, bearing the covalently self-assembled $Eu(dbm)_3$-phen molecules, were left to cool to room temperature and repeatedly washed and sonicated with toluene and dichloromethane to remove any residual physisorbed metal complex. The films strongly adhere to the substrates since they cannot be removed by abrasion with toluene wetted wipes and were stable for more than six months, as evidenced by X-ray photoelectron spectra.

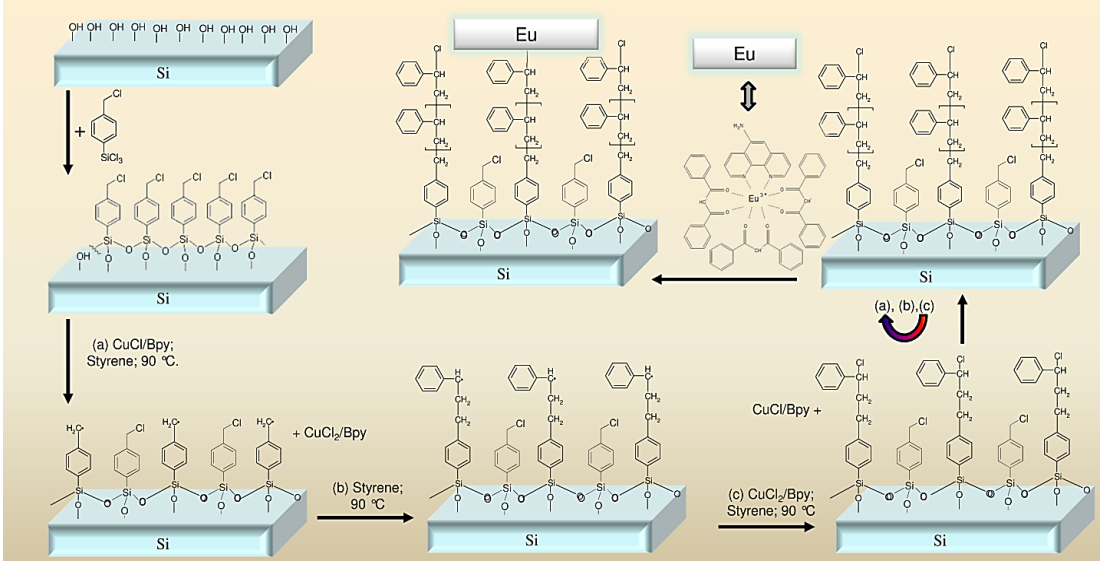

Scheme 3.1.1. Reaction pathway for the europium β-diketonate complex, covalently bound to nanoscale, surface-confined polystyrene assemblies.

3.1.2 Characterization of an Eu(III) Complex on Polystyrene Nanostructures

Infrared attenuated total reflectance (FTIR-ATR) spectra of the silicon-based monolayers were recorded using a Jasco FT/IR-430 spectrometer equipped with a Harrick GATR germanium single reflection ATR accessory, in the 4000-400 cm^{-1} range, with a resolution of 4 cm^{-1}. One hundred scans per spectrum were collected.

FTIR-ATR measurements of the SA_PSS_Eu confirmed the grafting of the $Eu(dbm)_3$phen complex on the substrate with $\nu_a(CH_2)$ and $\nu_s(CH_2)$ stretching modes at 2920 and 2854 cm^{-1}, respectively (Figure 3.1.2).[23] Furthermore, modes at 1536 and 1504 cm^{-1} are due to the C=O and C=C stretching, respectively for β-diketonate complexes. Finally, at 1648 and 1632 cm^{-1} there is evidence of the C-N group.

UV-Vis measurements were performed on quartz-based SA_PSS_Eu systems (Figure 3.1.3, red line) and on a $Eu(dbm)_3$-phen 1.6 $x \cdot 10^{-5}$ M CH_2Cl_2 solution (Figure 3.1.3, black line), used as reference to verify wheter the molecular system had modified its optical properties. Spectra show a close correspondence, in fact, in

both cases two bands are apparent whose positions for the Eu solution are at 287.5 and 348.6 nm and for the SA_PSS_Eu are at 290.8 and 358.6 nm.

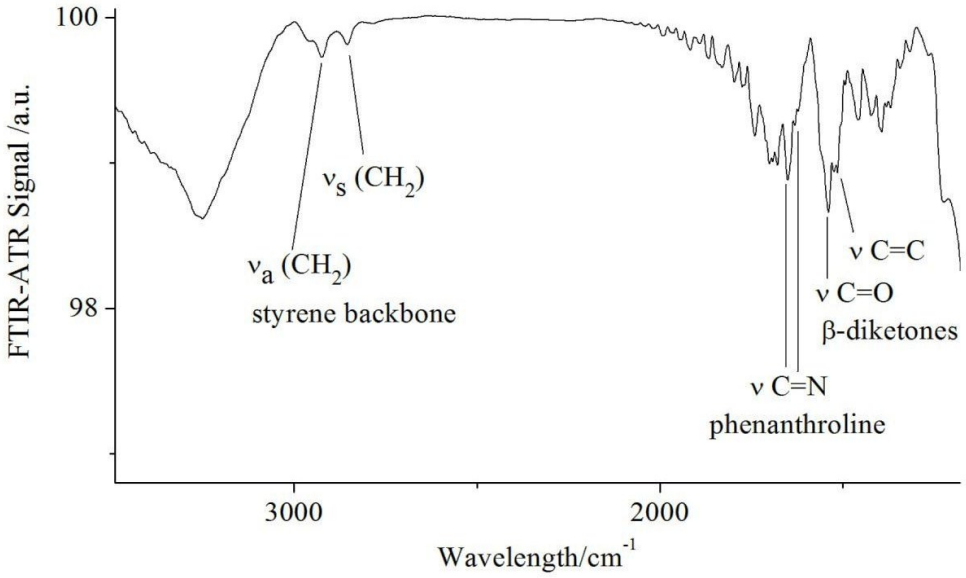

Figure 3.1.2. FTIR-ATR of SA_PSS_Eu on Si(100).

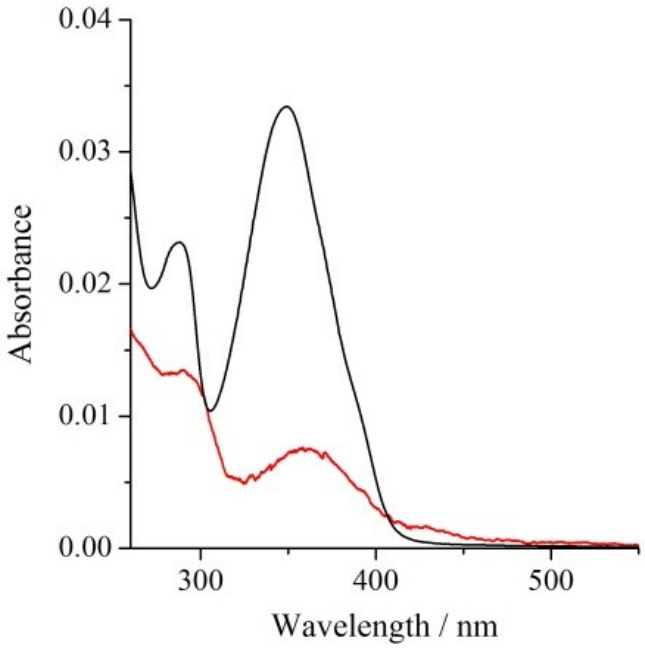

Figure 3.1.3. UV-Vis spectra of the $Eu(dbm)_3$-phen 1.6 x 10^{-5} M CH_2Cl_2 solution (black line) whose absorbance values were divided by 30; SA_PSS_Eu on quartz (red line).

Taking into account the ε value of 63000 $M^{-1}cm^{-1}$ for the band at 358.6 nm of

$Eu(dbm)_3$-phen in CH_2Cl_2, the calculated density value for SA_PSS_Eu is 3.6 x 10^{13} molecules/cm^2 with a footprint of 278 $Å^2$ per molecule.[25] This value is in agreement with a full surface coverage once the Eu molecule cross-section area (201 $Å^2$ estimated with the Gaussian 03 code) was taken into account.[26]

The XPS structural characterization of SA_PSS_Eu shows in the Eu 3d energy region a well resolved spin-orbit doublet at 1134.8 and 1164.5 eV, with a 29.7 eV spin-orbit separation, consistent with Eu(III) states (Figure 3.1.4).

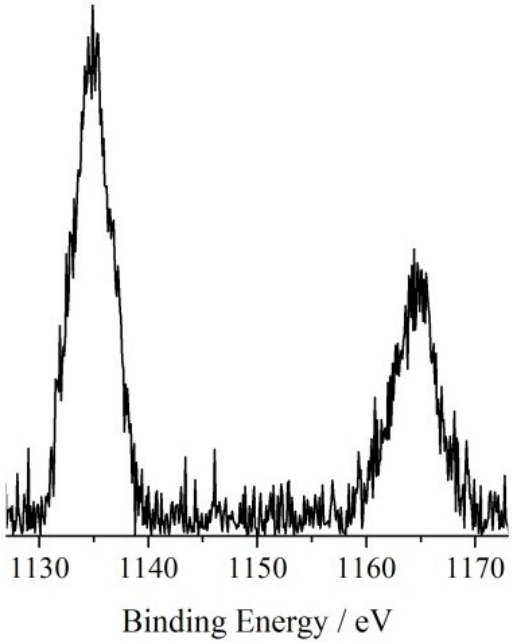

Figure 3.1.4. Monochromatized Al Ka excited XPS for the SA_PSS_Eu on Si(100) in the Eu 3d binding energy region at 45° take-off angle.

The N 1s spectrum shows a symmetric peak at 399.6 eV (Figure 3.1.5). This signal accounts for the three nitrogen atoms of the amino-phenanthroline ligand.[27] The N/Eu XPS atomic concentration ratio of 2.7 is largely compatible with the expected theoretical value of 3. Observing the C 1s region of the SA_PSS_Eu system it is possible to notice that the peak is asymmetric as a consequence of the presence of carbon atoms with different oxidation states. Through an accurate fitting of the experimental profile, three components were revealed (Figure 3.1.6).

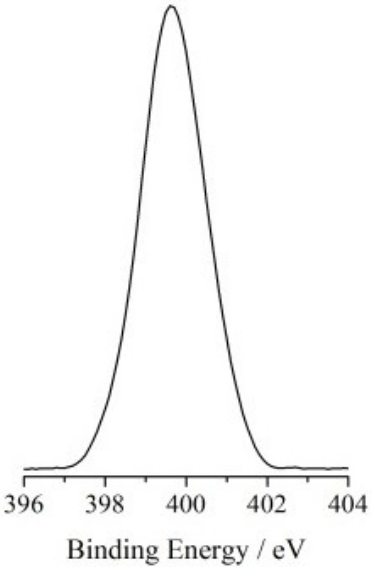

Figure 3.1.5. Monochromatized Al Ka excited XPS for the SA_PSS_Eu on Si(100) in the N 1s binding energy region at 45° take-off angle.

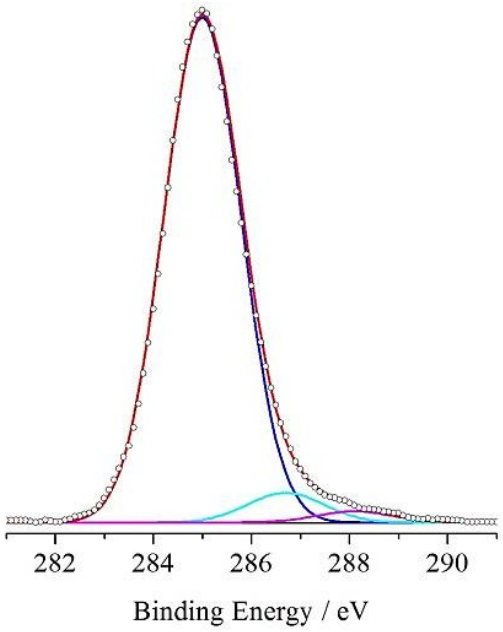

Figure 3.1.6. Monochromatized Al Ka excited XPS for the SA_PSS_Eu on Si(100) in the C 1s binding energy region at 45° take-off angle. The black empty dots refer to the experimental profile, the cyan and magenta lines refer to the Gaussian at 286.8 and 288.2, respectively; the red line superimposed to the experimental profile refers to the sum of the Gaussian components.

The first component at 285.0 eV is due to the aliphatic and aromatic carbon atoms. The second component at 286.8 eV is due to the not reacted C-Cl functionalities of the

SA_PSS_Eu (Scheme 3.1.1), and to the C-N groups of the amino-phenanthroline; the component at 288.2 eV is consistent with the C=O groups of the β diketonate anions. The intensity ratio between the 286.8 and 288.2 eV components is 2.66:1. Since in the Eu complex there are 6 C-N and 6 C=O groups, the expected C-N/C=O intensity ratio is 1. The extra intensity of the 286.8 component is due to the C-Cl functionalities. It emerges that the 2.66:1 intensity ratio is consistent with 10 not reacted C-Cl plus 6 C=N and 6 C=O groups in the 16:6 ratio. This result is in total agreement with the UV-Vis footprint of 278 $Å^2$ per Eu molecule that corresponds to the footprint of 11 silane moieties, each of which has a 24 $Å^2$ footprint. Moreover, AFM studies for the SA_PSS_Eu shows an average height of these features of 6.7 nm (Figure 3.1.7, right), in total agreement with the thickness (of about 6.5 nm) expected on the basis of previously reported data related to the increase of the polystyrene thickness vs. the reaction time.[23] This means that XPS technique is able to probe the whole present thickness.

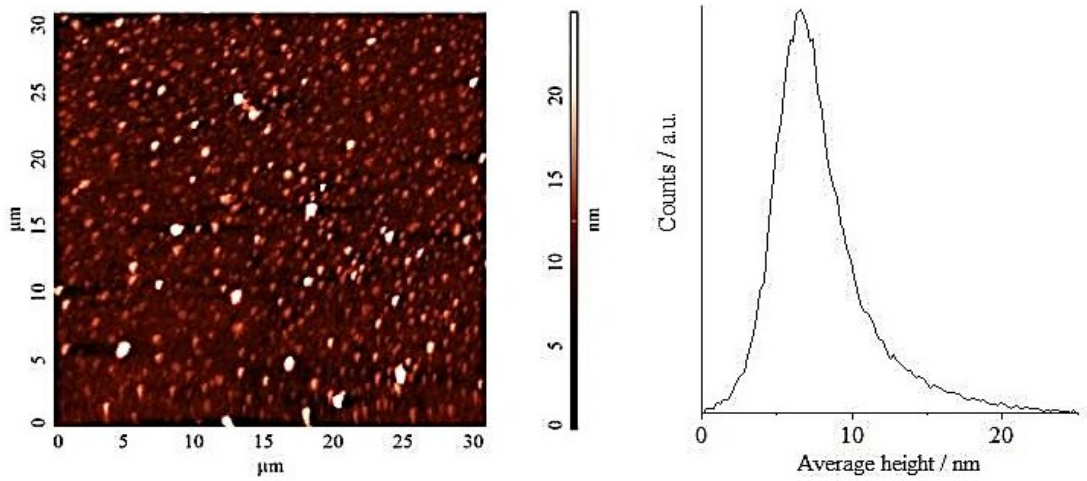

Figure 3.1.7. AFM of SA_PSS_ Eu on Si(100) (left); Average height (right).

In fact, the spectrum in the Si 2p binding energy region shows the two peaks at 99.9 and 103.1 eV, typical of the Si and SiO_2 phases respectively (Figure 3.1.8). Moeover, quantum mechanical calculations indicate a footprint for each polystyrene chain of about 100 $Å^2$ (Figure 3.1.9) corresponding to the footprint of 4 silane moieties.

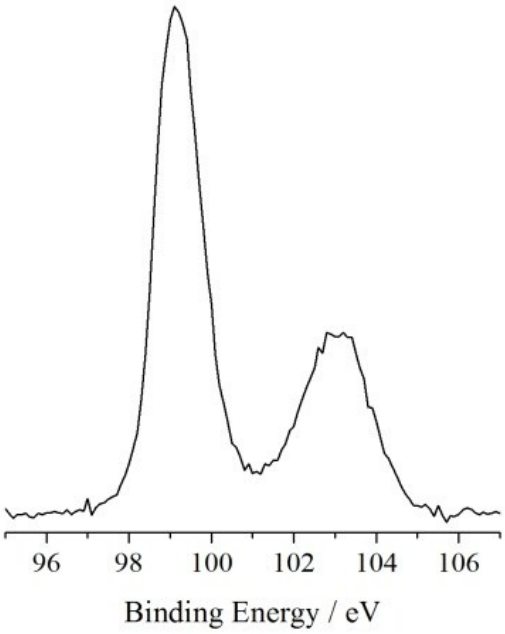

Figure 3.1.8. Monochromatized Al Ka excited XPS for the SA_PSS_Eu on Si(100) in the Si 2p binding energy region at 45° take-off angle.

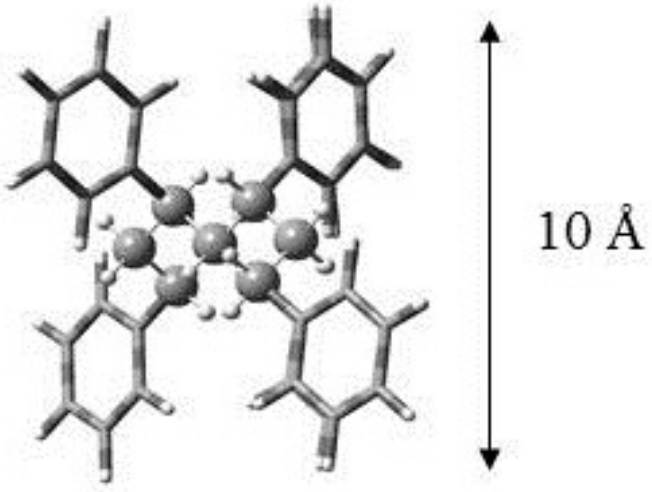

Figure 3.1.9. Polystyrene chain size (footprint) obtained by quantum mechanical calculations.

Therefore, each Eu complex substitute for one by three polystyrene C-Cl groups and this corresponds to one Eu complex by 11-12 silane benzyl chloride functionalities. From these consideration, it appears that the coupling of UV-Vis and XPS techniques is very useful to study monolayers since provides unique information.

Luminescence measurements were carried out using different λ_{exc} in the 220-

380 nm range, (step 10 nm), at room temperature (Figure 3.1.10).

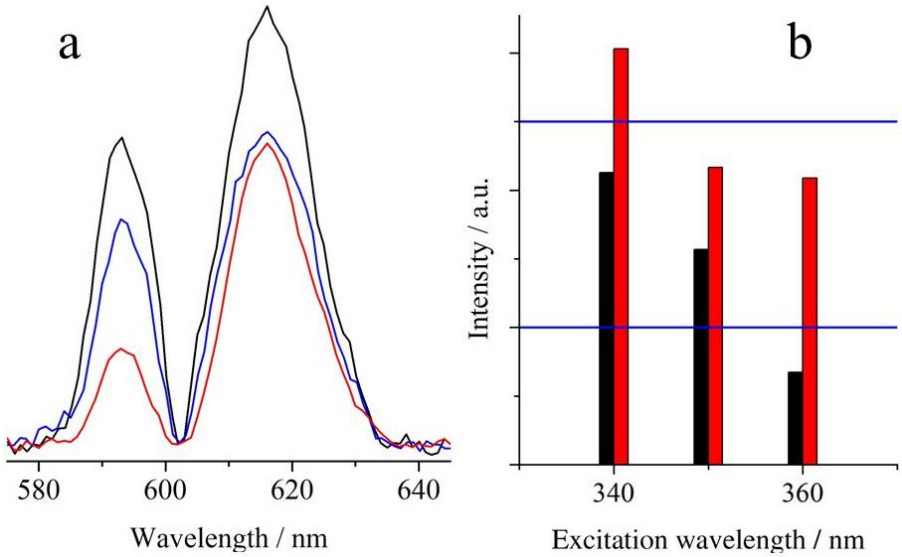

Figure 3.1.10. a) Luminescence spectra of the SA_PSS_Eu on Si(100) at different excitation wavelengths: 340 (black line), 350 (blue line) and 360 nm (red line); b) Behaviour of the PL intensity of the SA_PSS_Eu on Si(100) at different excitation wavelengths: 593 nm emission (black histograms) and 616 nm emission (red histograms); the two blue lines represent arbitrary thresholds.

In $Eu(dbm)_3phen$ the fluorescence is governed by the Free Resonance Energy Transfer (FRET) effect. In fact, 1,10-phenanthroline (Phen) acts as a synergic shielding ligand, which can reduce the rate of nonradiative decays and strongly enhance the fluorescence intensity of the complex.[28] Eu(III) has five narrow emission bands corresponding to the $^5D_0 \rightarrow ^7F_j$ transitions, where j = 0, 1, 2, 3, 4 and the cross-section for the $^5D_0$ (lowest excited state) $\rightarrow$ $^7F_{0\text{-}6}$ (ground states) transitions depends on the Eu site symmetry.[12,29] Moreover, Eu(III) in sites with inversion symmetry shows the magnetic-dipole $^5D_0 \rightarrow ^7F_1$ transition at about 590 nm, whilst, Eu(III) in sites with no inversion symmetry undergoes the electric-dipole $^5D_0 \rightarrow ^7F_2$ strong transition with emissions in the 610–620 nm range.

The SA_PSS_Eu exhibits photoluminescence with a strong, sharp and well resolved emission at 616 nm (Figure 3.1.10a) that can be ascribed to the electric-dipole $^5D_0 \rightarrow ^7F_2$ transition of the Eu^{3+} ions located at the sites without inversion symmetry.[30-32] A less intense emission peak for the $^5D_0 \rightarrow ^7F_1$ is also evident at 593 nm.[33-35] Other

very weak PL signals are present at higher wavelength, out of the range of Figure 3.2.9a. Therefore, in the present Eu(III)-monolayer[30] both electric- and magnetic-dipole transitions are evident even though with different intensities.

In fact, 4f levels in lanthanide compounds have been generally considered essentially atomic in nature and simple spectators with respect to the chemical bond, because filled $5s^2$ and $5p^6$ levels shield 4f orbitals from ligand field effects.[33-35] In practice, the various states arising from f^n configurations are split by external fields only to a small extent (~100 cm^{-1}).[33-35] Therefore, even though with different intensities, both electric- and magnetic-dipole transitions are expected and evident in Eu(III)-containing materials.

In order to use the SA_PSS_Eu as a tunable luminescent device, PL measurements were carried out using different excitation wavelengths (Figure 3.1.10b). It turned out that the highest PL intensity values for both emission bands (at 593 and 616 nm) were observed using a λ_{exc} = 340 nm while the lowest values were observed using a λ_{exc} = 360, thus showing that the luminescence intensity is strongly dependent on the excitation radiation. From these results it emerges that the cross-section of the two magnetic-dipole and electric-dipole mechanisms are significantly and differently affected by the excitation radiations, being the emission at 593 nm that which suffers the stronger variation.[26] In fact, the PL intensity ratio of the two bands (at 616 nm /at 593 nm) seems rather constant (1.4-1.3) on passing from λ_{exc} = 340 to 350 nm whilst it strongly increases to 3.1 using a λ_{exc} = 360 nm. Comparing these results with those obtained from a monolayer of the same Eu complex covalently assembled on a quartz substrate (Eu-SAM) some relevant differences can be noticed. In fact, at λ_{exc} = 340 nm the relative intensities of the two observed (593 and 616 nm) emissions are significantly different in the two systems. Indeed, the intensity ratio of the 616/593 emissions is 8.8 for the Eu-SAM while is only 1.4 for the present SA_PSS_Eu on Si(100). At λ_{exc} = 360 nm this ratio decreases from 8.8 to 1.7 for the Eu-SAM while increases from 1.4 to 3.1 for the SA_PSS_Eu on Si(100). High ratios correspond to the predominance of the electric-dipole $^5D_0 \rightarrow {}^7F_2$ transition of the Eu^{3+} ions located at the

sites without inversion symmetry. As a consequence, the low intensity ratio value (1.4) observed for the Eu-complex in the present SA_PSS_Eu on Si(100) during the transition at λ_{exc} = 340 nm suggests that the Eu^{3+} ions reach a symmetry higher than that in their ground state, if compared to the Eu-SAM. Conversely, at λ_{exc} = 360 nm the larger intensity ratio value (3.1) suggests that the excited Eu^{3+} ions experience a symmetry lower than that in their ground state (with some inversion symmetry) since magnetic-dipole $^5D_0 \rightarrow {}^7F_1$ transition intensity at ~593 nm increases. As a consequence, this strong luminescence variation, upon the excitation wavelength, can be used as on/off controls. Concerning the emission at 616 nm, it is possible to choose an arbitrary high intensity threshold (Figure 3.1.10b) in order to get it ON (above the threshold) only at λ_{exc} = 340 nm and OFF (below the threshold) at λ_{exc} = 350 and 360 nm, being the emission at 593 always OFF. Alternatively, one can choose a lower intensity threshold (Figure 3.1.10b) in order to get both emissions ON at λ_{exc} = 340 or 350 nm. The emission at 593 nm can be now OFF and that at 616 nm ON at λ_{exc} = 360 nm. Therefore, the obtained emission values can be triggered at will simply by choosing one or more arbitrary thresholds. These measurements were performed many times and outputs proved to be highly repeatable. The emission intensity can be alternated between different low and high intensity values.

Therefore, also this SA_PSS_Eu represents a system able to give optical outputs upon excitation input applications. The read-out procedure is fast and highly reliable and the system can be used as a tunable light emitting device for optical applications although it does not represent a switch.

3.2 Porphyrin_Eu-β-Diketonate Supramolecular Nanostructures

After demonstrating the effect of an aromatic polymeric environment on the luminescence properties of the lanthanide complexes now we show how the same properties can be modified also upon interaction with different luminescent aromatic molecules. In fact, in this study we show a superior combination of luminescent properties of a silica surface engineered with a porphyrin monolayer on which an Eu(III) complex was after assembled to obtain a supramolecular architecture. In particular, it was fabricated a covalent monolayer of the 5,10,15,20-tetrakis(4-hydroxyphenyl)-21H,23H-porphine (H2THPP_SAM) on which, $Eu(dbm)_3$-phen molecules were then anchored to obtain the H2THPP_Eu_SAM system.[1]

3.2.1 Synthesis of Porphyrin_Eu-β-Diketonate Nanostructures

Freshly prepared H2THPP_SAM (Chapter 2, paragraph 2.2.1) were transferred into the glove box and immersed in a dry toluene 8.3 x 10^{-4} M solution of $Eu(dbm)_3$-phen (Aldrich) for 24 h while stirring at room temperature. The remaining not-reacted porphyrin phenolic -OH groups reacted with the amino group of the phenanthroline thus giving an ammonium phenate salt (Scheme 3.2.1). The final H2THPP_Eu_SAM system was repeatedly washed/sonicated with toluene at ambient temperature. H2THPP_Eu_SAM demonstrated to be high temporally stable and thermally robust.

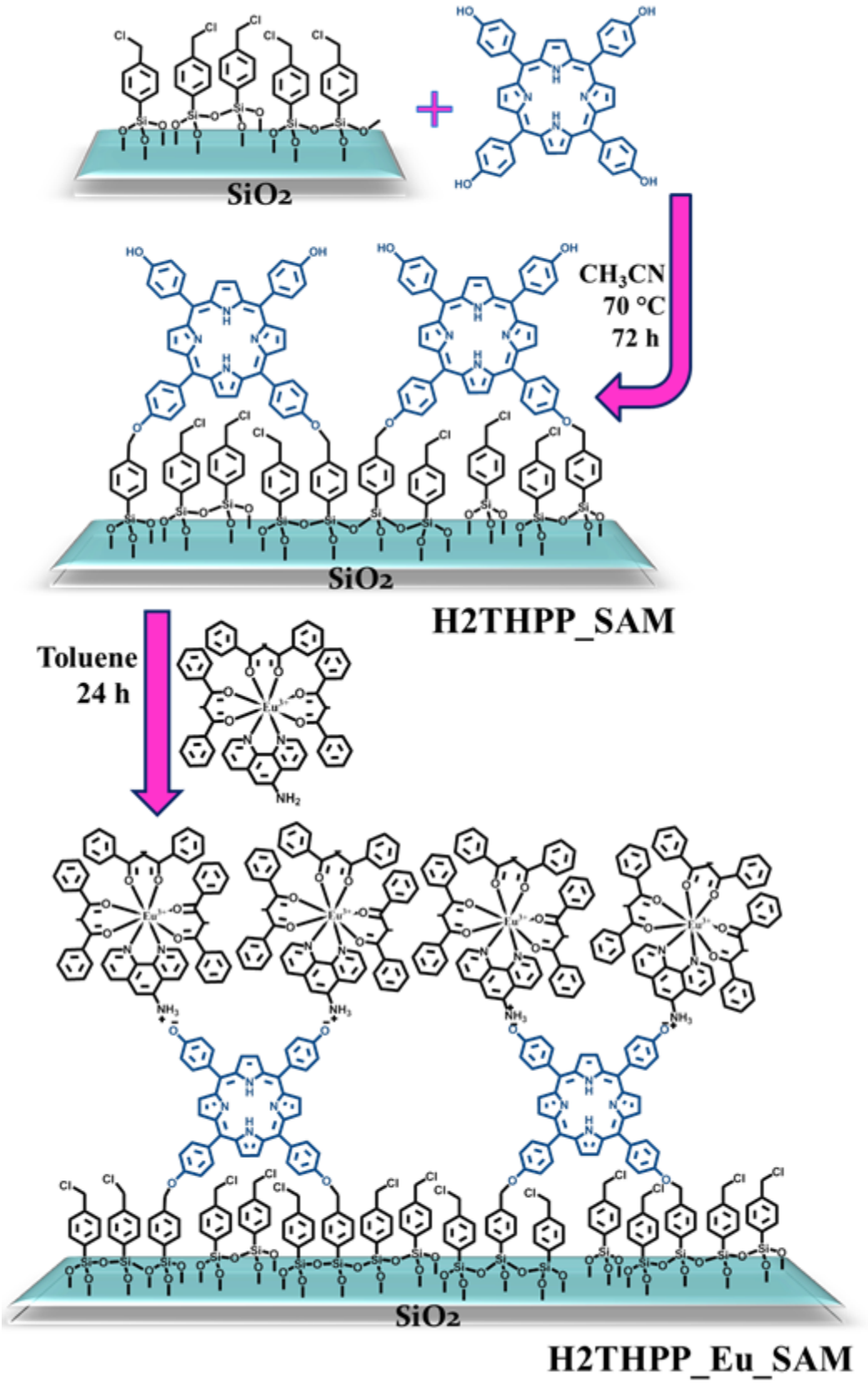

Scheme 3.2.2. Synthesis pathway for porphyrin-Eu-β-diketonate nanostructures.

3.2.2 Characterization of Porphyrin_Eu-β-Diketonate Nanostructures

The synthesized systems were characterized by AR-XPS measurements (5°, 15°, 45° and 80° take-off angles). The characterization of H2THPP_SAM is reported in Chapter 2, paragraph 2.2.2).

Figure 3.2.1 shows the XP spectrum of the H2THPP_Eu_SAM in the Eu 3d energy region. The spin-orbit doublet at 1135.4 – 1165.2 eV is consistent with Eu(III) states. It is important to note that these values are about 1.3 eV at lower binding energy with respect to those previously observed for a simple covalent Eu monolayer on silica.[29] This shift is in agreement with the electron donating capability of the porphyrin ring that decreases the binding energy of the Eu states and confirms a strong interaction between these two entities.

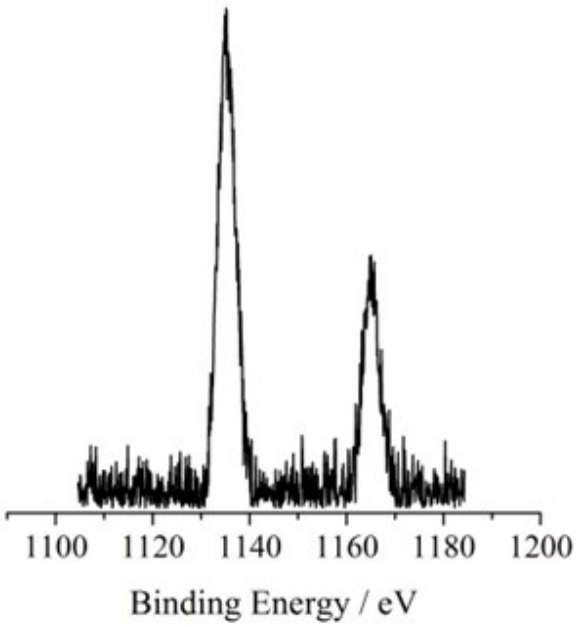

Figure 3.2.1. Monochromatized Al-Kα excited XPS of a representative H2THPP_Eu_SAM in the Eu 3d binding energy region at 45° take-off angle.

Figure 3.2.2 shows the high-resolution N 1s XP spectrum of the H2THPP_Eu_SAM and the fitting of the N 1s signal reveals the presence of two evident components in the 6:1 ratio. These two peaks lie at 399.8 and 402.0 eV. The

first component (399.8 eV) is assigned as a whole to the four pyrrole nitrogens of the porphyrin core and to the two nitrogens of the phenanthroline.[29,36] In contrast the peak at 402.0, already evident also in the experimental spectrum, is consistent with a protonated nitrogen due to the formation of the ammonium group.

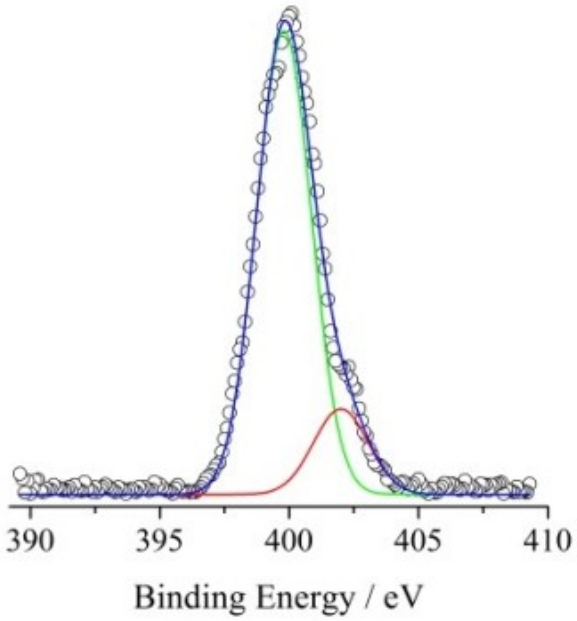

Figure 3.2.2. Monochromatized Al-Kα excited XPS of a representative H2THPP_Eu_SAM in the N 1s binding energy region at 45° take-off angle. The experimental spectral data points (open circles) are fitted with two dominant gaussians at 399.8 eV (green line) and 402.0 eV (red line). The blue line superimposed to the experimental profile refers to the sum of the Gaussian components.

This experimental observation is a strong evidence of the formation of the ammonium phenate salt between the porphyrin phenolic -OH groups and the amino group of the phenanthroline (Scheme 3.2.1). In addition, the XPS atomic concentration analysis revealed a N/Eu ratio of 4.8 ± 0.4 and this result is almost coincident with that expected on the basis of the overall grafting mechanism: two Eu-complexes per porphyrin molecule.

The morphology was studied by AFM technique and Figure 3.2.3 shows a micrograph for a representative H2THPP_Eu_SAM functionalised substrate that indicates the formation of a homogeneous surface layer.

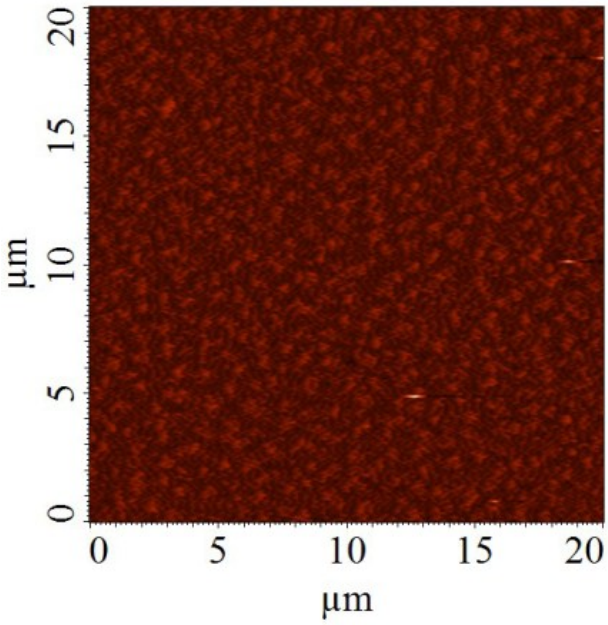

Figure 3.2.3. AFM image for a representative H2THPP_Eu_SAM.

3.2.3 Optical properties of Porphyrin_Eu-β-Diketonate Nanostructures

Figure 3.2.4 shows the UV-Vis absorption spectra of H2THPP_SAM (red line) and H2THPP_Eu_SAM (black line).

The UV/Vis of the H2THPP_SAM (Figure 3.2.4, red line) exhibits high quality signals and identifies the presence of H2THPP. In fact it shows a sharp characteristic Soret band at 428.6 nm and four satellite Q-bands at 528, 564, 596 and 657 nm (Figure 3.2.4 Inset). Figure 3.1.5, black line, shows the absorbance spectrum of the H2THPP_Eu_SAM. There is a 1.4 nm red shift in the Soret band that now appears at 430.0 nm. This shift towards lower energy values can be attributed to a consistent electron level reorganization of the frontier orbitals of the porphyrin (those responsible of the so-called B-band) upon interaction with the Eu complex. Moreover, the two evident absorption intensity increases at about 362 and 282 nm (black line) are diagnostic of $Eu(dbm)_3$-phen.[29]

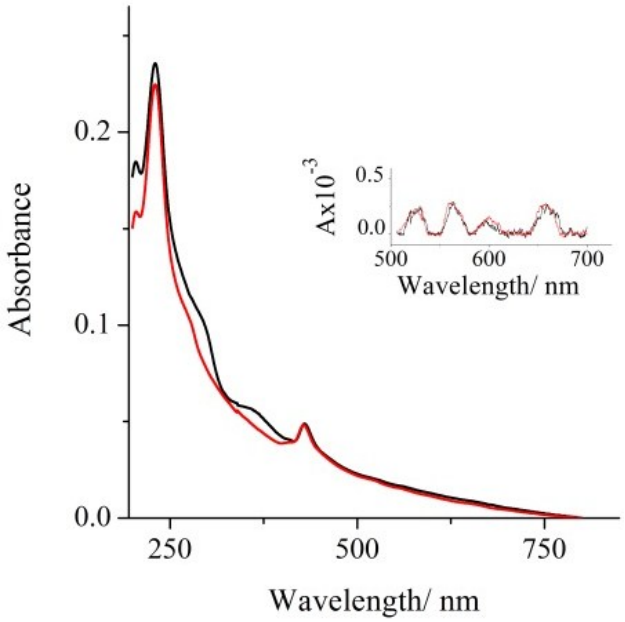

Figure 3.2.4. UV-Vis absorption spectra (0.2 nm resolution) of the H2THPP_SAM (red line) and H2THPP_Eu_SAM (black line). Inset: expanded scale of the 500-700 nm range.

In both spectra there are four evident Q-bands due to the electronic transitions from the two topmost filled molecular orbitals (HOMO's), a_{2u} (δ) and a_{1u} (δ), to the two degenerate lowest empty molecular orbitals (LUMO's), (δ*) of the porphyrin base. These four Q-bands reduce to two in porphyrin metal complexes. As a consequence, it is possible to safely affirm that the H2THPP_Eu_SAM is composed by the porphyrin base and the Eu metal complex thus excluding any formation of Eu-porphyrin metal complex.

Taking into account the ε value of H2THPP in CH_3CN, the surface coverage calculated in H2THPP_SAM is $1.9 \cdot 10^{13}$ molecules/cm^2. This value is in agreement with already reported results on similar systems and confirms the presence of a compact porphyrin monolayer. In analogy, using the intensity difference between the two spectra at 362 nm, (Abs = 0.008) and the ε = 62400 in toluene, the obtained Eu complex coverage is $3.7 \cdot 10^{13}$ molecules/cm^2. This value is close to the double of that of the porphyrin molecules/cm^2 and suggests that two Eu-complex molecules are bound per each porphyrin molecule in the H2THPP_Eu_SAM, according to the

Scheme 3.2.1. This result is in tune with the results of the XPS atomic concentration analysis.

The emission properties were investigated using a fluorescence spectrophotometer with λ_{exc} of 360, 380, 400, 420 and 440 nm (± 0.2 nm wavelength reproducibility) at room temperature. Figure 3.2.5 shows photoluminescence emission measurements at different excitation wavelengths of the H2THPP_Eu_SAM sample. Four PL emissions at λ = 592.8, 613.0, 656.8 and at 721.8 nm are present. The first two emission bands at 592.8, 613.0 can be ascribed to the magnetic-dipole $^5D_0 \rightarrow {}^7F_1$ and electric-dipole $^5D_0 \rightarrow {}^7F_2$ transitions between the Eu states, respectively.

The other two emissions at 656.8 and 721.8 nm are well tuned with already reported measurements on porphyrin monolayers assembled on solid substrates, and it is interesting to note some relative intensity variations among all these bands (Figure 3.2.6).

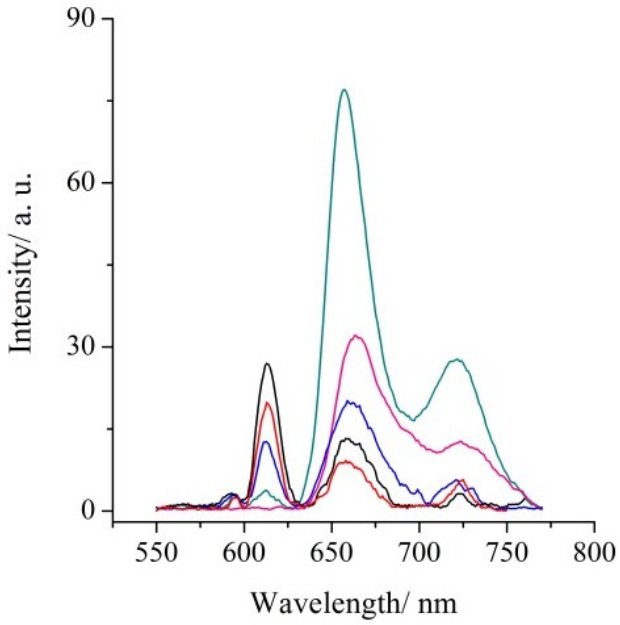

Figure 3.2.5. Photoluminescence spectra of H2THPP_Eu_SAM; λ_{exc} = 360 (black), 380 (red), 400 (blue), 420 (dark cyan) and 440 (magenta) nm.

The first important observation is represented by the trend to level off of the 592.8 and 613.0 nm bands with the increasing of the excitation wavelength up to 420 nm. In fact, almost identical intensities of the two Eu emissions (592.8 and 613.0 nm) at λ_{exc} =

420 nm are observed (Figure 3.2.6). As already discussed these intensities are strongly related to the existence of a symmetry centre element in the Eu molecule. This element is absent in the ground state geometry of the present $Eu(dbm)_3$-phen and therefore, in principle the band at 592.8 nm should be absent. It is noted that PL spectra of Eu(III) complexes show both electric and magnetic-dipole bands with diverse cross-sections. Then, some geometrical distortions in the excited state apparently further stress this behaviour and almost equalize the intensities of these two emissions.

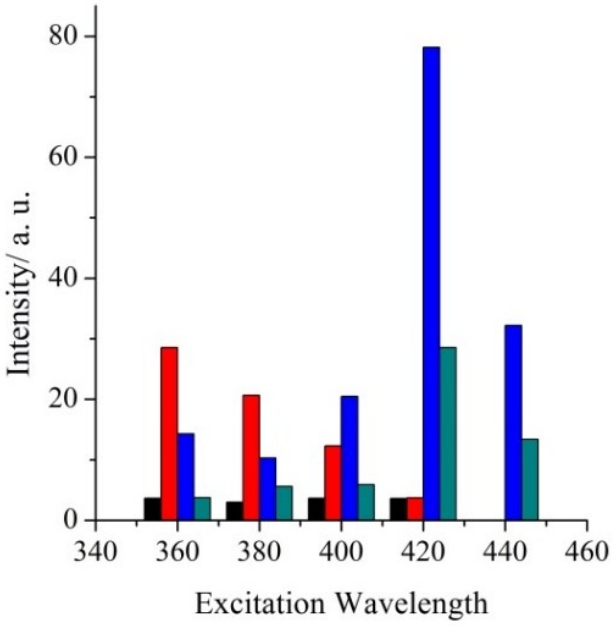

Figure 3.2.6. Relative intensity variations of the photoemission bands of the H2THPP_Eu_SAM at λ_{exc} = 360, 380, 400, 420 and 440 nm. Black bar = band at 592.8 nm of Eu; red bar = band at 613.0 nm of Eu; blue bar = band at 656.8 nm of H2THPP; green bar = band at 721.8 nm of H2THPP.

This observation was never previously reported. At λ_{exc} = 360 nm the 592.8 nm emission of Eu and that at 721.8 nm of H2THPP also show almost identical intensities. At both λ_{exc} = 360 and 380 nm the 613.0 nm emission band of Eu is the most intense. The 656.8 nm emission of H2THPP dominate the PL spectra at $\lambda_{exc} \geq 400$ nm. At λ_{exc} = 440 nm no Eu emission is observed.

It has been noted a previous significant change in the intensity ratio of the

613.0/592.8 nm emissions that increased from 1.7, for a simple covalent monolayer of this Eu complex on quartz,[29] to 3.1 for a Eu monolayer covalently bound to these polystyrene nanostructures.[35] Now, the observed intensity ratio of the 613.0/592.8 nm emissions is 7.5. This high ratio is certainly due to the Eu complex interacting with the porphyrin system. In addition, the 656.8/721.8 nm intensity ratio is 3.6, 1.9, 3.5, 2.7 and 2.4 at λ_{exc} = 360, 380, 400, 420 and 440 nm, respectively. From this overall view it emerges a delicate balance between porphyrin and Eu-complex electronic states that results in unprecedented optical properties.[37] Therefore, it arises an interesting way to compare/contrast selected emissions at different excitations and these can be safely used as discriminants. Indeed, it is possible to choose appropriate and different thresholds to transform emission intensities (or even better emission intensity ratios) in optical ON/OFF actions.

In Figure 3.2.7 an example of arbitrary thresholds is showed and it is clear that these can allow using the 656.8/721.8 nm and the 613.0/592.8 nn emission ratios for ON/OFF actions.

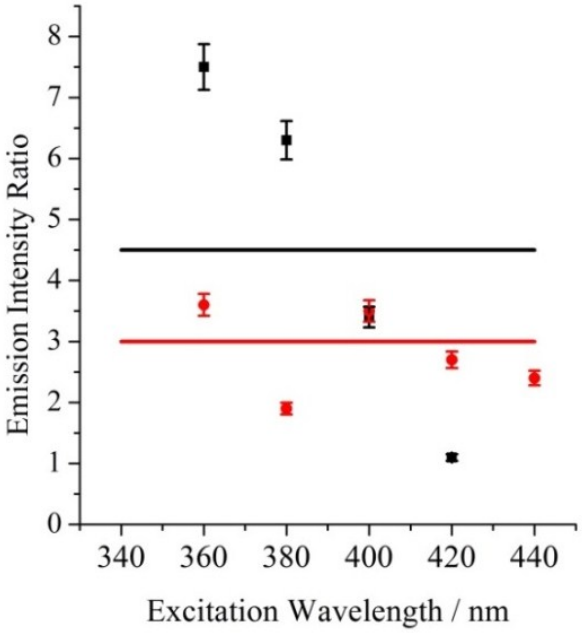

Figure 3.2.7. Emission intensity ratios vs. λ_{exc} : red squares refer to the 656.8/721.8 nm ratios, black circles refer to the 613.0/592.8 ratios; red and black solid lines refer to the arbitrary thresholds for the 656.8/721.8 nm and the 613.0/592.8 nm emission ratios, respectively. The bar errors refer to the experimental uncertainty in the data points observed during 10 different measurements.

More interesting, the system allows to read a couple of outputs (two ratio values) using just one input (excitation wavelength). As a consequence, there are four ON/OFF combinations associated to the four excitation wavelengths as reported in Table 3.2.1. These measurements were performed many times and outputs proved to be highly repeatable. The emission intensity can be alternated above and below the thresholds. Therefore, this H2THPP_Eu_SAM represents a new system that responds to excitation inputs by luminescence emission intensity variations (output).

Table 3.2.1 Optical outputs vs λ_{exc} for the H2THPP_Eu_SAM.

656.8/721.8 nm	613.0/592.8 nm	λ_{exc} / nm
ON	ON	360
OFF	ON	380
ON	OFF	400
OFF	OFF	420

It seems that covalent and ionic electronic interactions play a fundamental role on the variation of photoluminescence relative intensities and, eventual inter-molecular interactions between adjacent molecules can also contribute to some extent. The read-out procedure is fast and highly reliable and the system can be used as a tunable light emitting device for photonic applications. All the above measurements proved to be high repeatable and these supramolecular nanostructures were stable for at least five months after the synthesis.

Nevertheless, it is fair to say that this system does not represent a switch since the different luminescence intensity of any of the emission bands at any excitation wavelengths are not due to different and stable physical states of the system.[38]

3.3 An Y-complex for SAM application

Yttrium strongly resembles lanthanides, it is found in Nature along with the lanthanides and is usually considered beside them.[39] Nevertheless, the yttrium(III) centre does not show d-d nor f-f transitions.

In the present study we synthesized a new molecular Y-system, the tris(1,1,1,5,5,5-hexafluoro-2,4-pentanedionate) mono(5-amino-1,10-phenanthroline)yttrium (III) complex, $Y(hfa)_3$-phen, and studied its optical outputs upon the excitation input,[40-41] in the future perspective of using it as new luminescent molecule for SAM-based nanostructures.

3.3.1 Synthesis of $Y(hfa)_3$-phen

The $Y(hfa)_3$-phen (Scheme 3.3.1) was synthesized using a procedure already reported for similar β-diketonate metal complexes of zinc, cadmium and cobalt, saturated with polydentate glymes as ancillary ligands.[42-47]

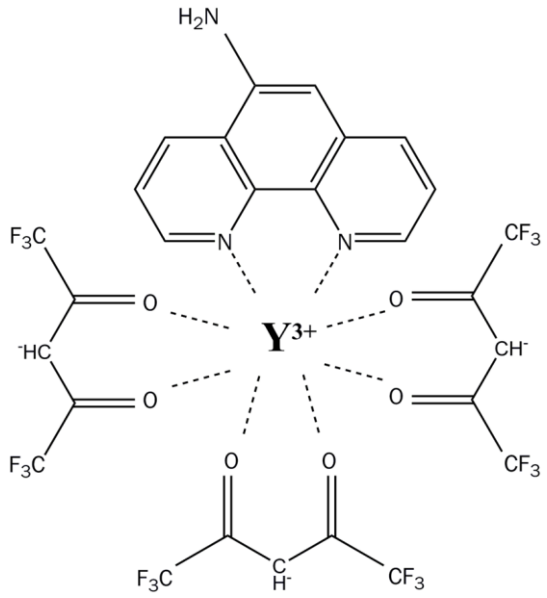

Scheme 3.3.1. Schematic representation of the synthesized $Y(hfa)_3$-phen complex.

In the present case, 5-amino-1,10-phenanthroline was used instead of polyethers. The $Y(hfa)_3$-phen was synthesized by adding, under vigorous

stirring, 0.8550 g ($2.2 \cdot 10^{-3}$ mol) of $Y(NO_3)_3 \cdot 6H_2O$ and 0.93 ml ($6.57 \cdot 10^{-3}$ mol) of hexafluoroacetylacetone, Hhfa, (mol ratio 1:3) in 50 ml of CH_2Cl_2.

3.3.2 Characterization of $Y(hfa)_3$-phen

The chemical characterization of the $Y(hfa)_3$-phen complex was performed by elemental analysis, MALDI-TOF mass spectra, IR, ^{1}H-NMR, XPS, UV-Vis, and photoluminescence measurements.

The XPS of the synthesized $Y(hfa)_3$-phen complex in the C 1s binding energy region is shown in Figure 3.3.1.

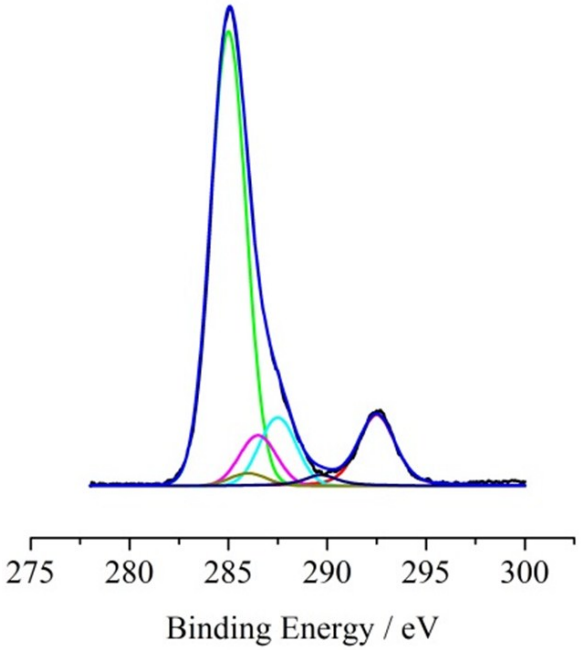

Figure 3.3.1. Al-Kα excited XPS of $Y(hfa)_3$-phen in the C 1s binding energy region. The black line refers to the experimental spectrum, the green line refers to the Gaussian at 285.0 eV, the dark yellow line refers to the Gaussian at 286.0 eV, the magenta line refers to the Gaussian at 286.6 eV, the cyan line refers to the Gaussian at 287.5 eV, the navy line refers to the Gaussian at 289.7 eV, the red line refers to the Gaussian at 292.5 eV, the blue line superimposed to the experimental profile refers to the sum of the Gaussians components.

In detail, the C 1s band consists of six components: the first centered at 285.0 eV is due to the aliphatic and aromatic backbones; the second at 286.0 eV is due to the carbon of the C-NH_2 group; the third at 286.6 eV is due to the carbon of the C=N functions; the fourth at 287.5 eV is due to the carbon of the C=O groups; the fifth at

289.7 eV, in tune with literature data, is due to the π-π* shake up satellites of conjugated and aromatic carbon systems. Finally, the sixth and the highest binding energy component at 292.5 eV is due to the carbon of the CF_3 groups. Note that the relative intensity of the Gaussian components at 286.0, 286.6, 287.5 and 292.5 eV is 1 : 4 : 6 : 6 consistent with the formula of the $Y(hfa)_3$-phen complex.

Figure 3.3.2 shows the XPS of $Y(hfa)_3$-phen in the Y 3d binding energy region

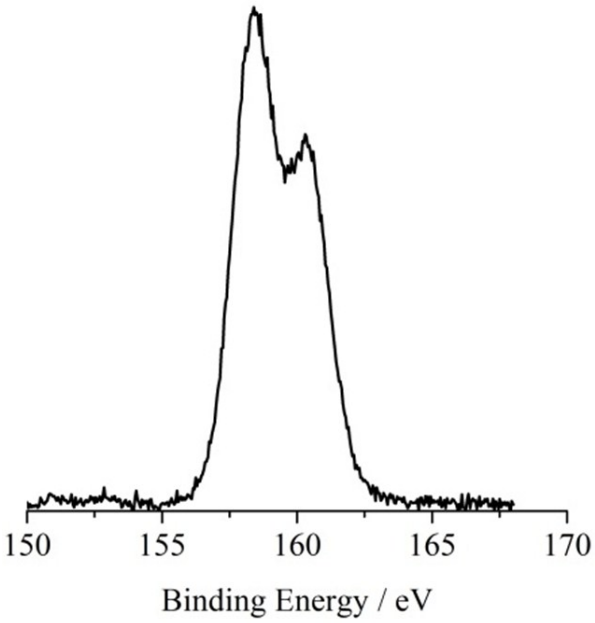

Figure 3.3.2. Al-Kα excited XPS of the $Y(hfa)_3$-phen in the Y 3d binding energy region.

Two spin-orbit peaks at 158.4 ($3d_{5/2}$) and 160.3 ($3d_{3/2}$) eV are evident. These values are between the highest observed for Y compounds and are justified by the presence of the three hfa anions in which there is a total of six -CF_3 withdrawing groups that significantly increase the Y(III) 3d binding energies. Also the spin-orbit separation of 1.9 eV is somewhat larger than that usually observed. In the YI_3 molecule the $3d_{3/2}$ level was reported at 160.40 eV while in the YF_3 molecule the same level is reported at 161.20 eV.[48] B.E. values of 158.2, 158.3 and 159.7 eV for the $3d_{5/2}$ levels, similar to those observed for the present $Y(hfa)_3$-phen complex, have been reported for the yttrium arachidate,[49] for the yttrium(III) oxalate nonohydrate[50] and for the yttrium(III) trioxalate, [51] respectively. All these values are surprising larger than

those observed for Y(III) in oxide matrices (e.g. 157.8 ($3d_{5/2}$) and 159.1 ($3d_{3/2}$) eV).[52,53]

Figure 3.3.3 shows the XPS of the $Y(hfa)_3$-phen in the N 1s binding energy region. The signal was fitted using two symmetric Gaussians at 399.1 and 399.7 eV and the obtained 1:2 intensity ratio is consistent with ionization of the –NH and the 2 -N=C groups of the 5-amino-1,10-phenanthroline ligand, respectively.

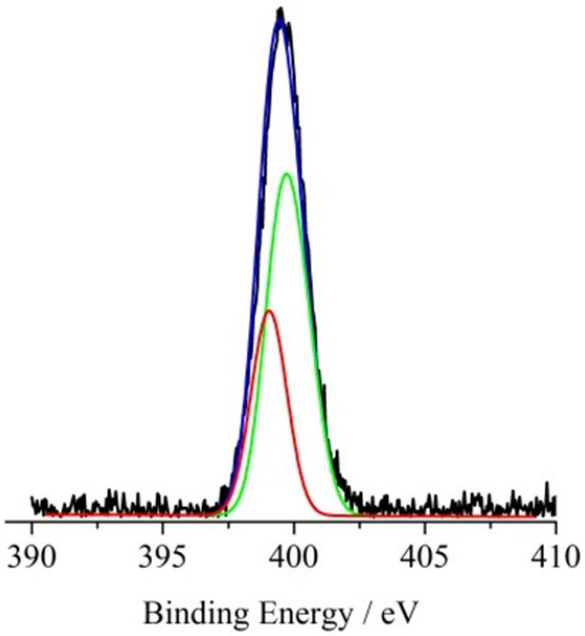

Figure 3.3.3. Al-Kα excited XPS of the: $Y(hfa)_3$-phen in the N 1s binding energy region. The black line refers to the experimental spectrum, the green line refers to the Gaussian at 399.1 eV, the red line refers to the Gaussian at 399.7 eV, the blue line superimposed to the experimental profile refers to the sum of the Gaussians components.

The UV-Vis spectrum of a CH_2Cl_2 $Y(hfa)_3$-phen 1.8 $x \cdot 10^{-5}$ M solution (Figure 3.3.4) shows an intense absorption band ranging from 225 nm to 550 nm that contains a strong band at 286.0 nm (ε = 43900) with two right hand asymmetries at 316.7 and 345.5 nm. Moreover, two left hand bands at 257.3 and 236.7 nm are also evident. The two absorption peaks at 286.0 and 345.5 nm are attributed to n-π and π-π* transition of the β diketonate ligand.

Figure.3.3.5 shows the photoluminescence emission spectra for a CH_2Cl_2 $Y(hfa)_3$-phen 1.8 $x \cdot 10^{-3}$ M solution, using different excitation wavelengths.

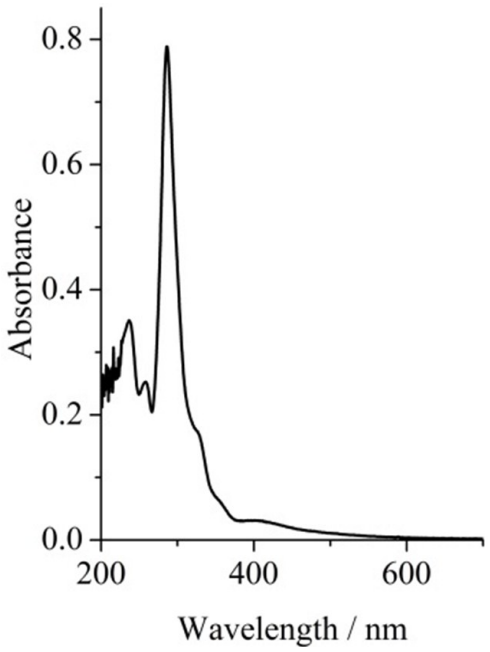

Figure 3.3.4. UV-Vis spectrum of a CH_2Cl_2 $Y(hfa)_3$-phen 1.8 x·10^{-5} M solution.

Typical stability constants in the range of 10^5 M^{-1} have been reported for these adduct in anhydrous organic solvents.[54,55] Therefore, we are confident that the adduct remains intact in the 1.8 x·10^{-3} M CH_2Cl_2 solution since no significant ligand dissociation is expected. An emission band at 509 nm is always present in the PL spectra, which mainly originates from the ligand-centred π-π* transition of the hexafluoro-2,4-pentanedionate ligand. Important, the emission intensity is strongly dependent on the excitation wavelength. In fact, normalized to 100 % the emission observed at λ_{exc} = 255 nm, it reduces to 14.6 % and to 49.2 % at λ_{exc} = 225 and λ_{exc} = 285 nm, respectively. As a consequence, it is possible to set one arbitrary intensity threshold to use the emission of the $Y(hfa)_3$-phen as an ON/OFF output.[17,22] For example, if the threshold is set to 49.2 %, the system will return the OFF value using λ_{exc} = 225 nm and the ON value using λ_{exc} = 255.

In particular, we tried to find a chemical way to encode the optical emissions of this new luminescent and simple molecular architecture in a modified Morse Code whose output can be optically read.

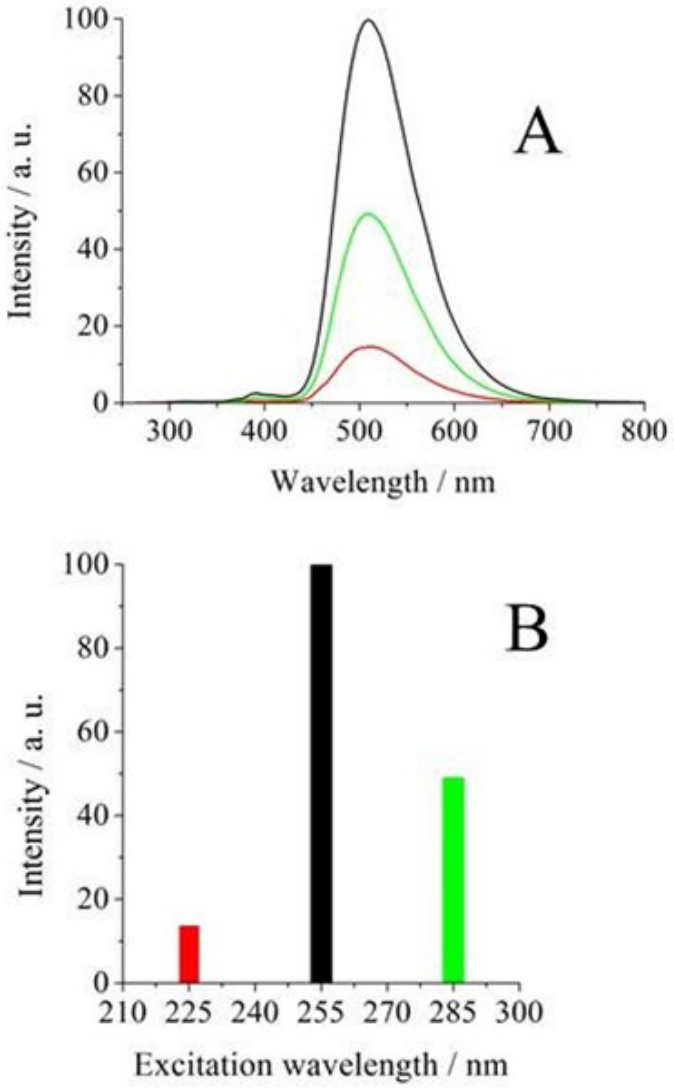

Figure 3.3.5. A: Normalized luminescence spectra of the $Y(hfa)_3$-phen 1.8 $x \cdot 10^{-3}$ M CH_2Cl_2 solution at three different excitation wavelengths: 225, 255 and 285 nm; B: Bar histogram representation of the intensity emission upon the excitation wavelengths.

The Morse code is widespread among radio operators, pilots, sailors, air traffic controllers, etc.. The most popular Morse code is the standard internationally recognized emergency signal, SOS, which is encoded in three dots, three dashes and three dots. One of the limits of the Morse Code is represented by the length of the dot whose duration has to be calibrated on the ability of the "reader/listeners". Using $Y(hfa)_3$-phen as system to transfer information the duration of the dot is as short as the typical photoluminescence events.

The optical signal transduction of $Y(hfa)_3$-phen can be easily performed by assigning to the dot the intensity emission upon the 225 nm excitation, and to the dash the intensity emission upon the 255 nm excitation (Table 3.3.1).

Table 3.3.1 Transduction of the photoluminescence intensity of the $Y(hfa)_3$-phen in the International Morse Code.

Symbol	Excitation λ	IMC	Symbol	Excitation λ	IMC
A	E_{225} E_{255}	•–	S	E_{225} E_{225} E_{225}	•••
B	E_{255} E_{225} E_{225} E_{225}	–•••	T	E_{255}	–
C	E_{255} E_{225} E_{255} E_{225}	•–•	U	E_{225} E_{225} E_{255}	••–
D	E_{255} E_{225} E_{225}	–••	V	E_{225} E_{225} E_{225} E_{255}	•••–
E	E_{225}	•	W	E_{225} E_{255} E_{255}	•– –
F	E_{225} E_{225} E_{255} E_{225}	••–•	X	E_{255} E_{225} E_{225} E_{255}	–••–
G	E_{255} E_{255} E_{225}	– –•	Y	E_{255} E_{225} E_{255} E_{255}	–•– –
H	E_{225} E_{225} E_{225} E_{225}	••••	Z	E_{255} E_{255} E_{225} E_{225}	– –••
I	E_{225} E_{225}	••	1	E_{225} E_{255} E_{255} E_{255} E_{255}	•– – – –
J	E_{225} E_{255} E_{255} E_{255}	•– – –	2	E_{225} E_{225} E_{255} E_{255} E_{255}	••– – –
K	E_{255} E_{225} E_{255}	–•–	3	E_{225} E_{225} E_{225} E_{255} E_{255}	•••– –
L	E_{225} E_{255} E_{225} E_{225}	•–••	4	E_{225} E_{225} E_{225} E_{225} E_{255}	••••–
M	E_{255} E_{255}	– –	5	E_{225} E_{225} E_{225} E_{225} E_{225}	•••••
N	E_{255} E_{225}	–•	6	E_{255} E_{225} E_{225} E_{225} E_{225}	–••••
O	E_{255} E_{255} E_{255}	– – –	7	E_{255} E_{255} E_{225} E_{225} E_{225}	– –•••
P	E_{225} E_{255} E_{255} E_{225}	•– –•	8	E_{255} E_{255} E_{255} E_{225} E_{225}	– – –••
Q	E_{255} E_{255} E_{225} E_{255}	– –•–	9	E_{255} E_{255} E_{255} E_{255} E_{225}	– – – –•
R	E_{225} E_{255} E_{225}	•–•	0	E_{255} E_{255} E_{255} E_{255} E_{255}	– – – – –

In addition, the intensity emission upon the 285 nm excitation (threshold) can be used as a space for letters and words. In this way there are three different emission intensities that largely improve the Morse Code.

Conclusions

The *bottom-up* approach was used for the fabrication of multiple self-assembled nanostructures having unique optical properties that may be advantageous in many fields of nanotechnology.

In fact, a Eu-β-diketonate monolayer was implemented on polystyrene films thus obtaining a new chemical platform that responds to lights inputs by luminescence intensity variations and that may be useful in optoelectronic devices.

Furthermore, the functionalization of quartz substrates with a covalent porphyrin monolayer and then with an additional Eu-β-diketonate monolayer provided a supramolecular architecture with unique optical applications.

Finally, it was exploited the luminescence of a simple yttrium complex whose emissions were easily "keyed" ON and OFF and adapted for a versatile method for optical telecommunication as the Morse Code.

References

[1] S. Millesi and A.Gulino, *J.Mater. Chem. C,* **2014**, *2*, 5924-5930

[2] a) N. Erathodiyil, J. Y. Ying, *Acc. Chem. Res.* **2011**, *44*, 925–935. b) S. Bolisetty, J. J. Vallooran, J. Adamcik, R. Mezzenga, *ACS Nano*, **2013**, *7*, 6146–6155. c) S. Laurent, D. Forge, M. Port, A. Roch, C. Robic, V. Elst, R. N. Muller, Chem. Rev. **2008**, *108*, 2064–2110.

[3] M. Calvaresi, F. Zerbetto, *Acc. Chem Res*., **2013**, *46*, 2454–2463.

[4] J. Coraux, L. Marty, N. Bendiab, V. Bouchiat, *Acc. Chem Res*., **2013**, *46*, 2193–2201.

[5] C.-H. Lu, B. Willner, I. Willner, *ACS Nano*, **2013**, *7*, 8320–8332.

[6] Ida, S.; Ogata, C.; Shiga, D.; Izawa, K.; Ikeue, K.; Matsumoto, Y. *Angew. Chem. Int. Ed*. **2008**, *47*, 2480-2483.

[7] Deiters, E.; Song, B.; Chauvin, A-S.; Vandevyver, C. D. B.; Bünzli, J-C. G. *New J. Chem*. **2008**, *32*, 1140-1152.

[8] Arrachart, G.; Karatchevtseva, I.; Cassidy, D. J.; Triani, G.; Bartlett, J. R.; Man, M. W. C. *J. Mater. Chem*. **2008**, *18*, 3643-3649.

[9] Leonard, J. P.; Nolan, C. B.; Stomeo, F.; Gunnlaugsson, T., *Top. Curr. Chem.,* **2007**, *281*, 1-43.

[10] Hanaoka, K.; Kikuchi, K.; Kobayashi, S.; Nagano, T., *J. Am. Chem. Soc*., **2007**, *129*, 13502-13509.

[11] Bünzli, J-C. G., *Acc. Chem. Res*., **2006**, *39*, 53-61.

[12] Li, Y.; Yan, B.; Yang, H., *J. Phys. Chem. C,* **2008**, *112*, 3959-3968.

[13] Sun, Z.; Bai, F.; Wu, H.; Boye, D. M.; Fan, H., *Chem. Mater*. **2012**, *24*, 3415−3419.

[14] Lenaerts, P.; Driesen, K.; Van Deun, R.; Binnemans, K., *Chem. Mater*. **2005**, *17*, 2148−2154.

[15] Gai, S.; Yang, P.; Li, C.; Wang, W.; Dai, Y.; Niu, N.; Lin, J., *Adv. Funct. Mater*. **2010**, *20*, 1166−1172.

[16] L.-M. Fu, X.-F. Wen, X.-C. Ai, Y. Sun, Y.-S. Wu, J.-P. Zhang, Y. Wang, *Angew. Chem. Int. Ed*. **2005**, *44*, 747–750.

[17] Ishizaka, T.; Kasai, H.; Nakanishi, H., *J. Mater. Sci.* **2009**, *44*, 166–169.

[18] Yakimanskii, A. V.; Goikhman, M. Ya.; Podeshvo, I. V.; Anan'eva, T. D.; Nekrasova, T. N.; Smyslov, R. Yu., *Polymer Science Ser. A* **2012**, *54*, 921-941.

[19] Matyjaszewski, K.; Dong, H.; Jakubowski, W.; Pietrasik, J.; Kusumo, A., *Langmuir*, **2007**, *23,* 4528-4531.

[20] LeMieux, M. C.; McConney, M. E.; Lin, Y.-H.; Singamaneni, S.; Jiang, H.; Bunning, T. J.; Tsukruk, V. V., *NANO LETTERS*, **2006**, *6*, 730-734.

[21] Juang, A.; Scherman, O. A.; Grubbs, R. H.; Lewis, N. S., *Langmuir*, **2001,** *17,* 1321-1323.

[22] Cristaldi D. A., Millesi S., Mineo P., A. Gulino. *J. Phys. Chem. C*. **2013**, *117*, 16213-16220.

[23] Mineo, P.; Motta, A.; Lupo, F.; Renna, L.; Gulino, A., *J. Phys. Chem. C* **2011**, *115*, 12293-12298.

[24] Mineo, P. G.; Cristaldi, D. A.; Motta, A.; Gupta, T.; Gulino, A., *RSC Adv.* **2013**, *3*, 1137-1144.

[25] Gulino, A.; Gupta, T.; Altman, M.; Schiavo, S. L.; Mineo, P. G.; Fragalà, I. L.; Evmenenko, G.; Dutta, P.; van der Boom, M. E., *Chem. Commun.* **2008**, 2900-2902.

[26] Gulino, A.; Lupo, F.; Condorelli, G. G.; Motta, A.; Fragalà, I., *J. Mater. Chem.* **2009**, *19*, 3507-3511.

[27] Motiei, L.; Altman, M.; Gupta, T.; Lupo, F.; Gulino, A.; Evmenenko, G.; Dutta, P.; van der Boom, M. E., *J. Am. Chem. Soc*. **2008**, *130*, 8913-8915.

[28] E. Janos, B. Andrea, K. Attila, and K. Laszlo, J. Lumin. 1997, *72***,** 570.

[29] A. Gulino, F. Lupo, G. G. Condorelli, A. Motta and I. Fragalà, *J. Mater. Chem.*, **2009**, *19*, 3507.

[30] Bünzli, J.-C. C., *Chem. Lett*., **2009**, *38*, 104-109.

[31] Carlos, L. D.; Donega, C. D. M.; Albuquerque, R. Q.; Alves, J. R. S.; Menezes, J. F. S.; Malta, O. L., *Mol. Phys*. **2003**, *101*, 1037-1045.

[32] Robinson, M. R.; O'Regan, M. B.; Bazan, G. C., *Chem. Comm*. **2000**, 1645-1646.

[33] Roos, B. O.; Lindh, R.; Malmqvist, P.; Veryazov, V.; Widmark, P.-O.; Borin, A. C., *J. Phys. Chem. A*, **2008**, *112*, 11431-11435.

[34] Adamo, C.; Maldivi, P., *J. Phys. Chem. A,* **1998**, *102*, 6812-6820.

[35] Di Bella, S.; Gulino, A.; Lanza, G.; Fragala, I.; Stern, D.; Marks, T. J., *Organometallics,* **1994**, *13*, 3810-3815.

[36] A. Gulino, I. Fragalà, E. Scamporrino and D. Vitalini, *J. Phys. Chem.* C, **2007**, *111*, 14125.

[37] (a) J. Demel, P. Kubat, F. Millange, J. Marrot, I. Cisarova, K. Lang, *Inorg. Chem*., **2013**, *52*, 2779-2786. (b) X. Wu, W. Lv, Q. Wang, H. Wang, X. Zhang, J. Jiang, *Dalton Trans*., **2011**, *40*, 107-113. (c) G. Lu, Y. Chen, Y. Zhang, M. Bao, Y. Bian, X. Li, J. Jiang, *J. Am. Chem. Soc*. **2008**, *130*, 11623-11630. (d) K.-H. Schweikart, V. L. Malinovskii, A. A. Yasseri, J. Li, A. B. Lysenko, D. F. Bocian, J. S. Lindsey, *Inorg. Chem*. **2003**, *42*, 7431-7446. (e) D.-J. Qian, H.-G. Liu, K.-Z. Yang, H. Nakahara, K. Fukuda, *Mol. Cryst. Liq. Cryst. Sci. Technol. A: Mol. Crys. Liq. Crys.*, **1997**, *294*, 213-216. (f) N. B. D. Lima, S. M. C. Gonçalves, S. A. Jùnior, A. M. Simas, *Scientific reports*. **2013**, *3*, 2395.

[38] C. C. A. Ng, A. Magenau, S. H. Ngalim, S. Ciampi, M. Chockalingham, J. B. Harper, K. Gaus, Gooding, J. *J. Angew. Chem. In. Ed*. **2012**, 51, 7706-7710, S7706/1-S7706/18.

[39] A. Lannes, M. Intissar, Y. Suffren, C. Reber, D. Luneau, *Inorg. Chem.* **2014**, *53*, 9548-9560.

[40] D. A. Cristaldi, S. Millesi, P. Mineo, A. Gulino, *Journal of Luminescence*, **2016**, *169*, 348–352.

[41] M. W. Urban, Handbook of Stimuli-Responsive Materials. Wiley-VCH 69469 Weinheim, Germany, 2011. Printed in Singapore.

[42] A. Gulino, P. Dapporto, P. Rossi, G. Anastasi, I. Fragalà, *J. Mater. Chem.* **2004**, *14*, 2549-2553.

[43] A. Gulino, P. Dapporto, P. Rossi, I. Fragalà, *Chem. Mater.* **2003**, *15*, 3748-3752.

[44] A. Gulino, P. Dapporto, P. Rossi, I. Fragalà, *Chem. Mater.* **2002**, 14, 4955-4962.

[45] A. Gulino, P. Dapporto, P. Rossi, I. Fragalà, *Chem. Mater.* **2002**, *14*, 1441-1444.

[46] A. Gulino, F. Castelli, P. Dapporto, P. Rossi, I. Fragalà, *Chem. Mater.* **2002**, *14*, 704-709.

[47] A. Gulino, F. Castelli, P. Dapporto, P. Rossi, I. Fragalà, *Chem. Mater.* **2000**, *12*, 548-554.

[48] Y. Uwamino, A. Tsuge, T. Ishizuka, H. Yamatera, *Bull. Chem. Soc. Jpn.* **1986**, *59*, 2263-267.

[49] D. J. Johnson, D. T. Amm, T. Laursen, S. K. Gupta, *Thin Solid Films*,**1993**, *232*, 245-251.

[50] R. P. Vasquez, *J. Electron Spectrosc. Relat. Phenom.*, **1990**, *50*, 167-170.

[51] Y. Uwamino, Y. Ishizuka, H. Yamatera, *J. Electron Spectrosc. Relat. Phenom.*,**1984**, *34*, 67-68.

[52] A. Cristaldi, G. Impellizzeri, F. Priolo, T. Gupta, A. Gulino, *J. Phys. Chem. C.*, **2012**, *116*, 3363-3368.

[53] A. Gulino, I. Fragalà, *J. Mater. Chem.*,**1999**, *9*, 2837-2841.

[54] L. Babel, T. N. Y Hoang, H. Nozary, J. Salamanca, L. Guénée, C. Piguet, *Inorg. Chem.*,**2014**, *53*, 3568-3578.

[55] A. ZaÏm, H. Nozary, L. Guénée, C. Besnard, J.-F. Lemonnier, S. Petoud, C. Piguet, *Chem. Eur. J.*, **2012**, *18*, 7155-7168

.

Chapter 4

Electroactive Inorganic Substrates

In the previous chapters of this thesis it has been shown how the properties of molecular monolayers covalently assembled on inorganic substrates are strongly dependent on the inherent properties of the substrate itself. For example, we demonstrated that porphyrin molecules inject electrons on the surface of conducting oxides thus resulting systems suitable for the DSSC technology.

It is well known that TCOs (ITO, ZnO, CdO, etc.) combine optical transparency in the visible region with a high electrical conductivity and as a consequence they are key components in flat panel liquid crystal displays, organic light-emitting diodes, photovoltaics, solar cells, optical waveguides, and other optoelectronic devices.[1–6]

In this context, we tried to synthesise CdO thin films as potential electroactive substrates for SAM application.

4.1 CdO Thin Films

Although Sn-doped In_2O_3 is currently the most important TCO, thin films of CdO, the first TCO to be discovered,[7-8] show electrical and optical properties which are still of interest, with potential applications as photosensitive anode materials for photochemical cells, phototransistors, photodiodes, window electrodes in liquid crystal displays, IR detectors, antireflection coatings, gas sensors and in other solar energy applications.[9-12] They also show a high reflectivity in the infrared region and this behaviour renders them useful as heat reflectors.[13] CdO adopts face centred cubic rocksalt structure. The different parities of p and d orbitals within this centrosymmetric system prevents mixing of the shallow core Cd 4d states with O 2p valence band states at the Γ point, but mixing is allowed away from the zone centre. This results in upward dispersion of the top of the valence band along Γ-L and Γ-K directions. The conduction band is of dominant Cd 5s atomic character and has a minimum at the Γ point. The lowest bandgap is therefore indirect. A fundamental indirect gap as low as 0.55 eV at room temperature has been suggested, although a value of around 0.89-0.99 eV now seems more plausible.[14-16]

The direct allowed optical onset is found at about 2.18 eV.[17-18] Both direct and indirect absorption edges show a very strong blue shift with degenerate n-type doping due to the occupation of states at the bottom of the conduction band which blocks off the lowest energy transitions. This ensures that despite the relatively low values of the indirect and direct electronic gaps for undoped CdO, the highly doped material remains essentially transparent throughout the visible region. At the same time the very low value for the fundamental indirect gap coupled with strong dispersion in the conduction band ensures that the mid gap level integrated over all k-space – the so-called charge neutrality level (CNL) - lies well above the conduction band minimum. The position of the CNL provides a rough guideline as to the intrinsic dopability. CdO has a much lower fundamental gap than alternative TCO host materials In_2O_3 and SnO_2, where the direct forbidden gaps are respectively 2.9 eV[19-20] and 3.6 eV.[21]

Therefore the CNL lies less high above the conduction band minimum than in CdO. In addition, undoped CdO has a high refractive index (n_0 = 2.49) and a large third-order optical nonlinearity in the non-resonant region.[11-12] As the particle size decreases down to the nanometre scale, its nonlinear optical response is further enhanced due to the quantum size effect.[22]

The properties of CdO are strongly influenced by native donor defects arising from non-stoichiometry, which is in turn strongly dependent on the synthetic procedure adopted. In fact native donors can take CdO through a transition from a semiconductor to a degenerate metallic material.[14,23] There has been on-going debate about the nature of native donors. Recent *Density Functional Theory* calculations of Scanlon and Watson have shown that the formation energy of oxygen vacancies (V_o) is much lower than the formation energy of the Cd interstitials (Cd_i) under all growth conditions.[15] Moreover, both V_o and Cd_i were found to act as shallow donors in CdO, meaning that the behaviour of V_o in CdO is very different from that reported for V_o in other wide band gap n-type TCOs, i.e., ZnO, SnO_2, Ga_2O_3, and In_2O_3.[24-27] In these n-type TCOs, V_o was found stable only in the 0 and +2 charge states, meaning it is a negative-U defect (U is the Hubbard correlation energy). In CdO however, V_o is stable only in the + 2 state and does not display negative-U character.[15] In addition, H-related (hydrogen) impurities have been found to have very low formation energies in CdO under all growth conditions and to also act as shallow donors.[15] These theoretical results are in tune with the recent experiments of King et al. who found that both intrinsic defects and H-related impurities act as shallow donors in CdO.[28] These properties have stimulated the synthesis of CdO films using different chemical as well as physical methods.[29-33] As part of this activity, the doping of CdO with different trivalent cations has been explored.[14,23] For example, thin CdO films grown on glass and MgO (100) with 1.2 - 1.3 % Y doping were shown to exhibit maximum conductivities of 8540 and 17800 $\Omega^{-1}cm^{-1}$ respectively.[10]

Therefore, in our study we fabricated CdO films through an optimized metal organic chemical vapour deposition (MOCVD) method using the

$Cd(C_5F_6HO_2)_2{\cdot}CH_3(OCH_2CH_2)_2OCH_3$ (hereafter referred to as $Cd(hfa)_2{\cdot}$diglyme) liquid precursor (Figure 4.1.1) that assures constant evaporation rates for fixed temperatures.[33]

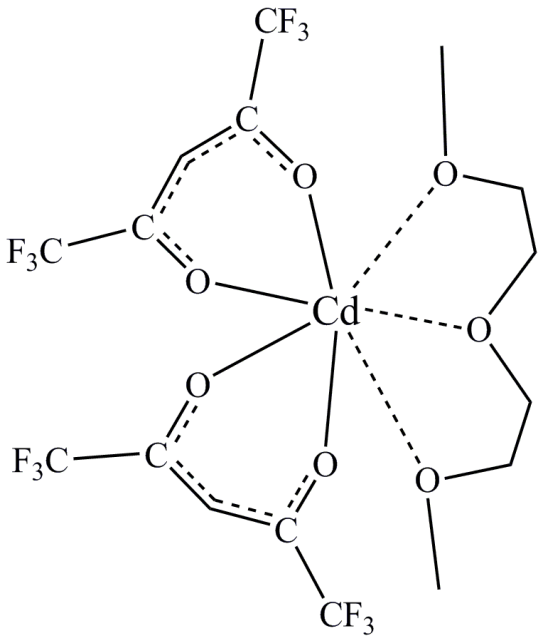

Figure 4.1.1. Structure of the $Cd(hfa)_2{\cdot}$diglyme precursor.

4.1.1 Synthesis of CdO Thin Films

The $Cd(hfa)_2{\cdot}$diglyme, (mp = 45 °C) precursor was synthesized from stoichiometric amounts of CdO, $C_5F_6H_2O_2$ (1,1,1,5,5,5,-hexafluoro-2,4-pentanedione, abbreviated H-hfa) and diglyme (bis(2-methoxyethyl)ether**)**.[33]MOCVD experiments were performed using a horizontal hot-wall reactor under reduced pressure. In brief, the reactor system consists of a gas-handling line, a tube furnace, a quartz reactor tube (total length = 80 cm and inner diameter = 2.4 cm), two quartz inlet tubes for Ar and O_2 and a vacuum system. The precursor was contained in an alumina boat and maintained at 90 °C. Fused SiO_2 plates mounted in the centre of the heated zone (400 °C) were used as substrates after cleaning in an ultra-sonic bath with isopropyl alcohol. 100 standard cubic centimetres per minute (sccm) of pure Ar carrier gas was used to transport the precursor to the substrate. The reactant gas consisted of water-saturated oxygen (100 sccm) introduced directly into the reactor close to the substrate. The

deposition time was 135 min. The total pressure was kept in the 2-4 Torr range. The CdO, formed during the deposition time settled on the quartz substrate, appears as a pale-yellow film.

4.1.2 Characterization of CdO Thin Films

The crystal structure of the synthesized CdO film was studied by X-ray Diffraction (XRD) measurements using a Bruker D-5005 diffractometer operating in a θ-2θ geometry (Cu Kα radiation, 30 mA and 40 kV) over an angular range 20° < 2θ < 80° (0.05° step-size) with a 10 s/channel dwell time. The XRD crystal parameter was obtained using the UNIT CELL programm.[34]

Figure 4.1.2 shows the XRD pattern for a representative CdO film. Only the (002) reflection is evident thus indicating a film oriented along the (001) direction and confirming that CdO is in a single cubic phase.

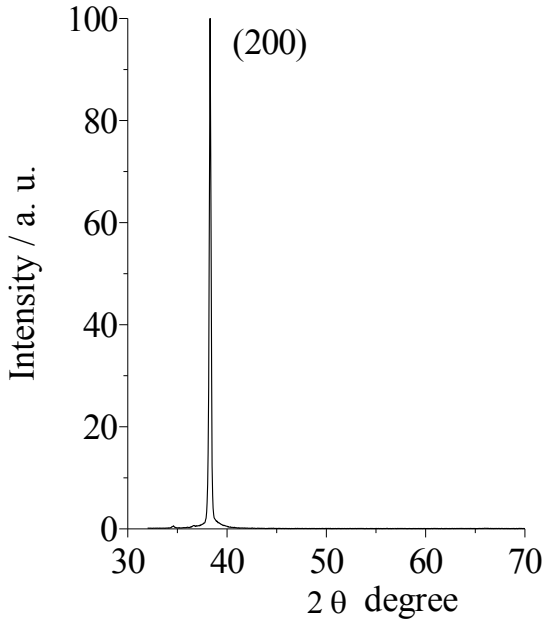

Figure 4.1.2. θ - 2θ x-ray diffraction profile for a CdO film.

The **a** value is 0.46983 nm for the as-synthesized CdO in good agreement with the ASTM=5-0640 data. Domain sizes of 21 nm for this CdO films were obtained from XRD data using the Debye Scherrer equation:

$$S = 0.9 \lambda / (B \cos \theta_B)$$

where:

-λ = 0.154056 nm;

-θ is Bragg angle of the (200) reflection;

-B is the full width at half maximum (FWHM) obtained as follows:

$$B^2 = B^2_f - B^2_s$$

B^2_f refers to the FWHM line broadening of the film and B^2_s refers to the FWHM line broadening of the standard (α-Al_2O_3).

The surface morphology investigated by AFM revealed that the surface mainly consists of grains joined each other with lateral dimensions of order 80 nm - 400 nm (Figure 4.1.3). The root mean square roughness of the films is typically around 6.2 ± 0.7 nm and with a total range of 16.9 ± 0.8 nm in the images.

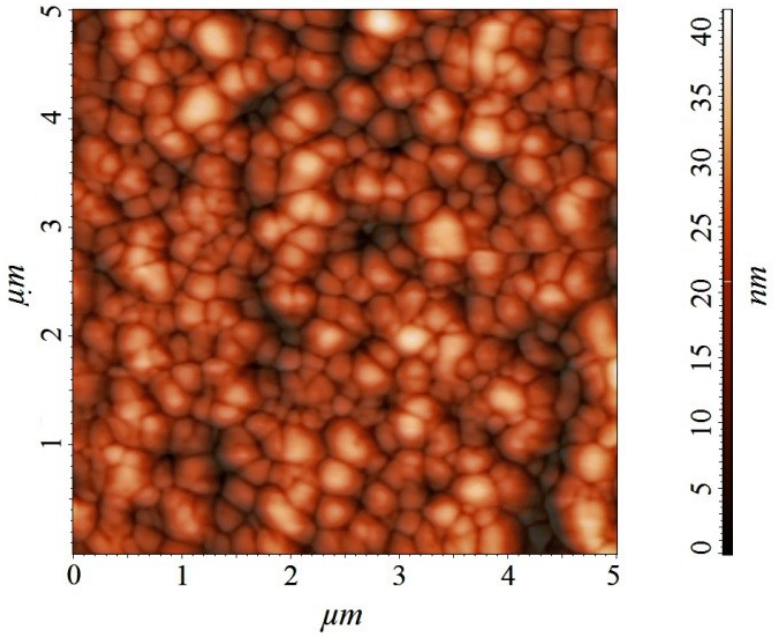

Figure 4.1.3. AFM image of a representative CdO film in a 5 x 5 μm area range.

The monochromatized Al Kα XPS spectrum for a typical CdO film in the Cd 3d binding energy region shows the well resolved Cd 3d spin-orbit doublet (Figure 4.1.4(a)) with peaks maxima at 404.6 ($3d_{5/2}$) and 411.3 ($3d_{3/2}$) eV.[33] Figure 4.1.4(b) shows the fitting of the asymmetric experimental Cd $3d_{5/2}$ peak by means of two

pseudo-Voigt functions whose characteristics are listed in Table 4.1.1.

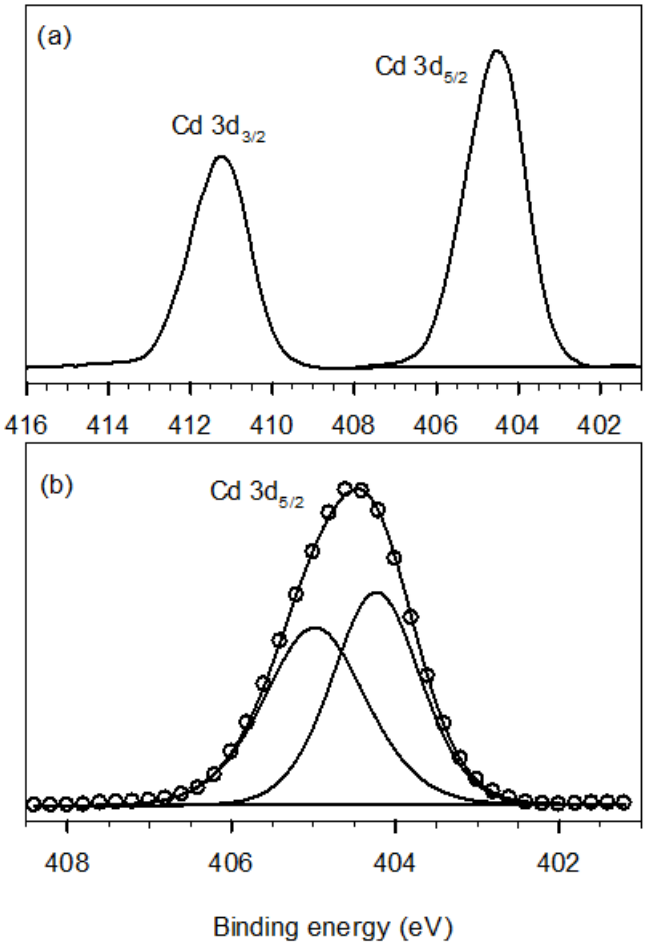

Figure 4.1.4. (a) Monochromatized Al-Kα excited XPS at 45° photoelectron take-off angle of the CdO film in the Cd 3d binding energy region. (b) Curve fit to the experimental data (open circles) is performed using two pseudo-Voigt functions.

Table 4.1.1. Parameters derived from curve fits to Cd $3d_{5/2}$ and O 1s core lines in XPS of CdO thin film. S, U and C refer to screened, unscreened and contaminant components and G and L to Gaussian/Lorentzian contributions to the lineshape.

Peak	Binding energy (eV)	FWHM (eV)	Relative Area	G:L ratio
Cd $3d_{5/2}$ (S)	404.23	1.26	0.51	0.63:0.37
Cd $3d_{5/2}$ (U)	404.98	1.46	0.49	0.55:0.45
O 1s (S)	529.04	1.28	0.56	0.74:0.26
O 1s (U)	529.75	1.63	0.42	0.26:0.74
O 1s (C)	532.06	1.42	0.02	0.50:0.50

Table 4.1.1 also lists the parameters related to the fitting of the O 1s spectrum (Figure 4.1.5). Even the O 1s spectral profile of the CdO thin film is dominated by two

Voigt components although in this case it is necessary to add a third very weak component to high binding energy of the two dominant components.

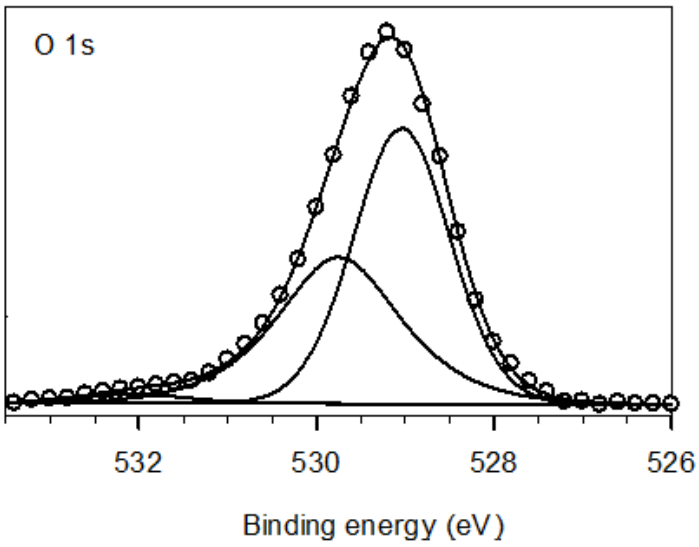

Figure 4.1.5. Monochromatized Al-Kα excited XPS at 45° photoelectron take-off angle for a CdO film in the O 1s binding energy region. The experimental spectral data points (open circles) are fitted with two dominant pseudo-Voigt components, with a third much weaker component at higher binding energy.

Two different models have been proposed to account for core photoemission spectra in so-called narrow-band metallic oxides of the sort studied here.[35] The first model, introduced by Wertheim to account for core the sodium tungsten bronzes Na_xWO_3 recognises that when the Coulomb lineshapes in interaction between a core hole and an orbital contributing to the conduction band exceeds the occupied conduction bandwidth, the potential associated with the core hole will create a localised state on the ionised atom.[36-40] Two different finals states are then accessible, depending on whether the localised state becomes occupied to give a screened final state or remains empty to give an unscreened final state. Within this model the probability of finals state screening should increase with increasing carrier density. The alternative model treats the low binding energy component as the "main" peak, while the higher binding energy peak is a strong plasmon satellite.[41-43] For a number of systems closely related to that under investigation such as Sb-doped SnO_2,[44] PbO_{2-x},[45] and Sn-doped In_2O_3[38] it has been shown that satellite energies are indeed close to

plasmon energies measured by infrared reflectance spectroscopy or electron energy loss spectroscopy.[14,16,19,46]

These two apparently distinct models produce rather similar qualitative conclusions i.e. increased intensity of the low binding energy component with increasing carrier density, and a lifetime broadened and dominantly Lorentzian lineshape for the high binding energy component. Therefore, the curve fit of Figure 4.1.4(b) indicates that the two components in the curve fit for the Cd $3d_{5/2}$ region at 404.23 eV and 404.98 eV are due to the screened (or main peak) and unscreened (plasmon satellite) states, respectively. A plasmon energy of 0.75 eV derived from the parameters in Table 4.1.1 for the Cd $3d_{5/2}$ curve fit may be used to estimate the carrier density *n* by reference to plasmon energies measured in earlier work by electron energy loss spectroscopy.[47] Taking account of linear variation in the electron effective mass with carrier density we obtained $n = 7 \times 10^{20}$ cm^{-3}, in qualitative agreement with carrier densities derived from Hall effect measurements to be discussed below. Similar carrier densities have been found for In-doped CdO films.[6]

4.1.3 Optical and Electrical properties of CdO thin films

The optical characterization of the film was performed by recording transmission spectra of the samples (Figure 4.1.6(a)). The film has optimal transparency in the 75-85% range in the visible region and the transmission spectrum shows interference fringes typical of films with thicknesses of same order as the wavelength of visible light. The data in the region of the band edge were replotted in Figure 4.1.6(b) in the form $(\alpha h\nu)^2$ versus photon energy $h\nu$, where α is the absorption coefficient (transmittance % / thickness). From this plot it was possible to estimate a direct allowed optical absorption onset of about 2.91 eV. This is strongly blue shifted from the direct allowed onset found at about 2.18 eV in CdO with very low carrier densities.[17,48-49] The shift is due to occupation of states at the bottom of the conduction band which block the direct allowed transitions at lowest energy, partially offset by shrinkage or renormalization of the fundamental gap. In addition, by taking into

account the eventual contribution of the reflectance, the measured optical bandgap of the CdO thin films could further increase. Comparison with measurements of direct onsets in a series of films with different doping levels let to estimate a carrier density of about 6×10^{20} cm^{-3}, in reasonable agreement with the estimate from core satellite structure discussed earlier.[18]

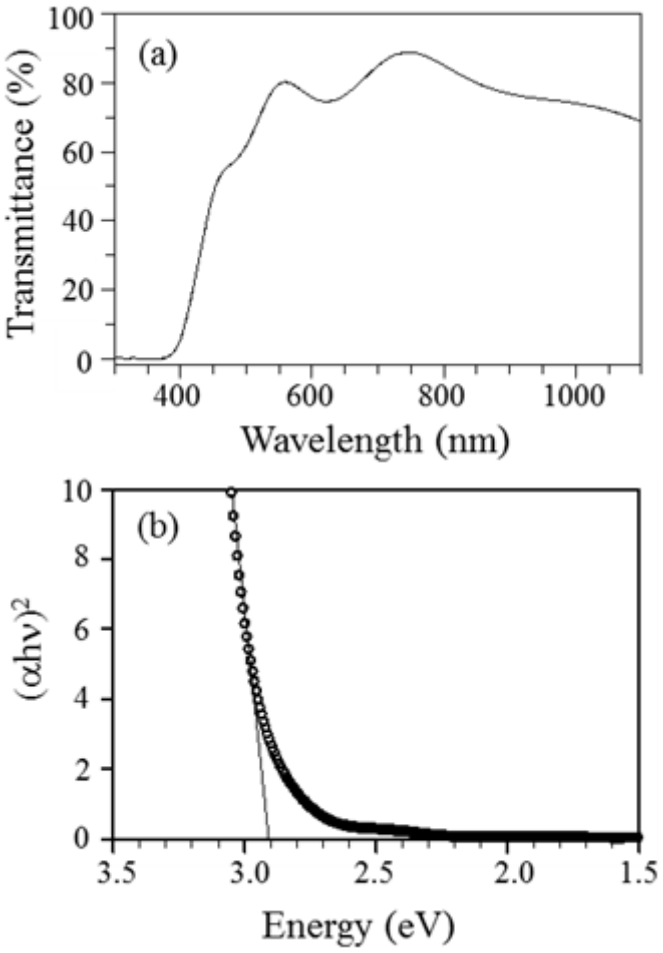

Figure 4.1.6. (a) Transmittance spectrum of a representative CdO thin film; (b) Tauc plot of $(\alpha h\nu)^2$ versus photon energy $h\nu$, where α is the absorption coefficient in the region of the direct allowed optical absorption onset.

Further investigations were carried out to study photoluminescence properties of the CdO films. Indeed, CdO films exhibit a broad photoluminescence peak (Figure 4.1.7) extending from about 560 nm (2.21 eV) to 435 nm (2.85 eV), with a peak at 493 nm (2.51 eV) and a shoulder which develops into a second peak at 521 nm (2.38 eV) upon decrease of exciting photon energy. The low energy onset at 2.21 eV corresponds

roughly to the direct allowed optical gap in undoped CdO and therefore corresponds to transitions from the bottom of the conduction band into a hole in the valence band at the Γ point.

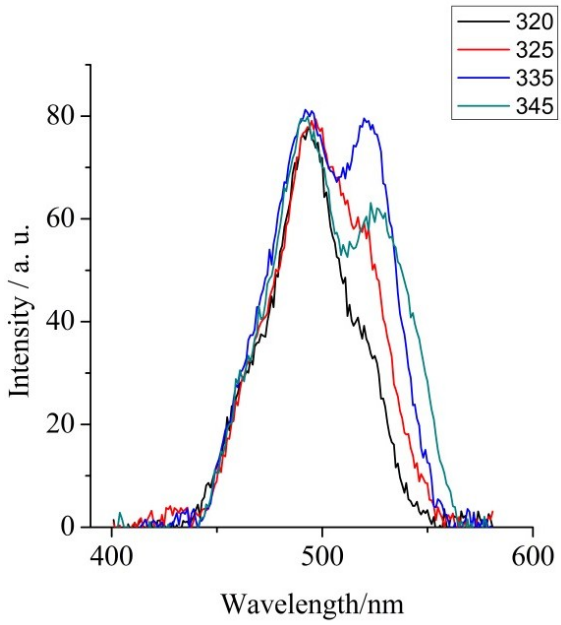

Figure 4.1.7. Photolominescence spectrum of the CdO thin film, in the 400-600 nm range or 3.1 - 2.1 eV range, as a function of excitation wavelength reported in the inset.

These transitions can arise if initial excitation is from the downward dispersing valence band states found along the Γ-X into empty conduction band states above the Fermi energy. Phonon-assisted relaxation will allow the valence band hole to move upwards within the valence band, eventually reaching the Γ point. The two peak structure is most likely to be associated with lifting of the degeneracy of the topmost valence band states in moving along the Γ-X direction.[15,50]

The electrical characterization was carried out in the dark by means of four-point probe resistivity and Hall effect measurements in the temperature range between 80 K and 460 K using a BioRad HL5560 rig.[39,51] The applied magnetic field was 0.322 T. Samples with dimensions 1 cm × 1 cm were simply contacted by four Au tips in a Van der Pauw geometry. This technique allows the determination of the resistivity, the carrier concentration and the mobility (the latter determined by the first two

quantities). The electrical measurements were repeatable to within 5% on independent samples. Temperature dependence of resistivity, carrier concentrations and Hall mobility are shown in Figure 4.1.8. The data show that the resistivity and mobility vary slightly with the temperature whereas the carrier concentration is temperature invariant, indicative of a degenerate semiconductor. In fact, transport measurements confirm that these films are n-type material with free-electron concentrations in the range between 7.4 x 10^{20} - 8.5 x 10^{20} cm^{-3} provided by native donors (Figure 4.1.8).[34,49]

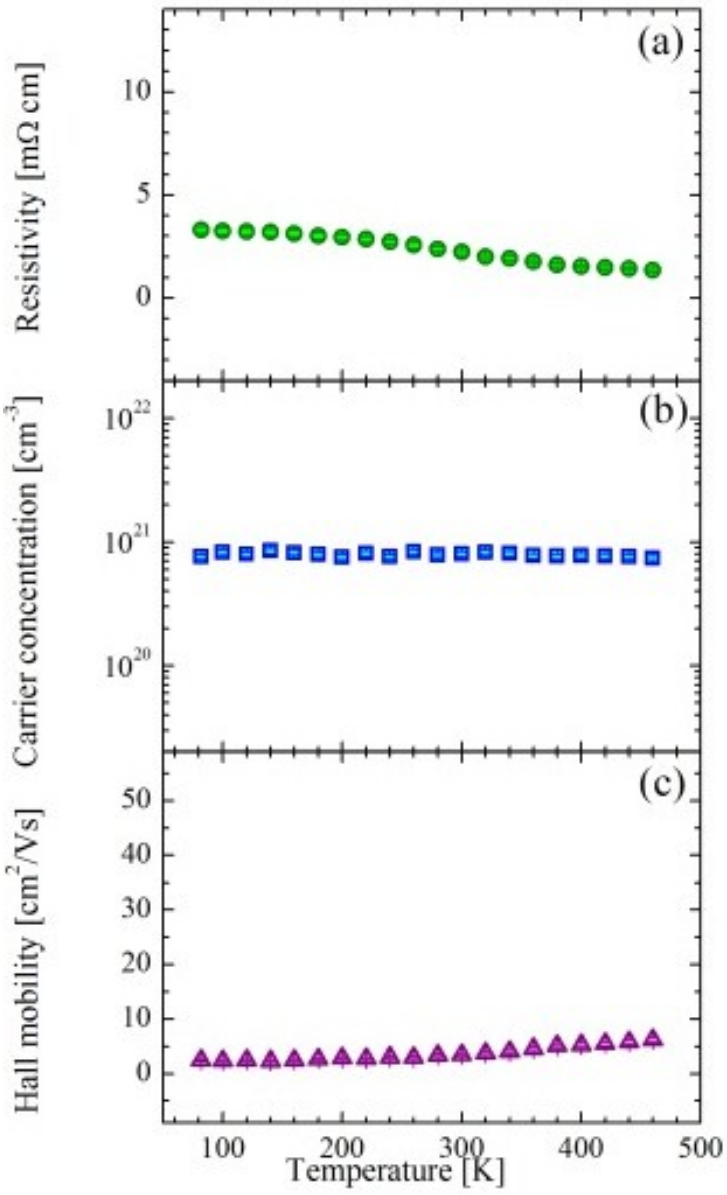

Figure 4.1.8. Resistivity (a), carrier concentration (b) and mobility (c) as a function of the temperature for CdO films.

Remarkably these values are interestingly larger than those recently estimated by Scanlon et al. in a density functional study. The procedure adopted was to use the calculated maximum Moss-Burstein shift and the effective mass at the conduction band minimum, to predict that the maximum carrier concentration would be ~4.34 x 10^{20} and ~5.25 x 10^{20} cm^{-3} for Cd-poor/O-rich and Cd-rich/O-poor conditions, respectively.[15] However these estimates assumed parabolic dispersion in the conduction band and ignored the effects of bandgap renormalization. The variation of the effective mass within the conduction band leads to a placement of the Fermi level at a lower value than expected from extrapolation from the behaviour at the bottom of the band for a given carrier density, so that both effects will lead to an underestimation of the limiting native carrier density.[46]

The carrier concentration is also much higher than the large majority of experimental values reported in literature[17,52] this is probably due to both the MOCVD technique and to the particular $Cd(hfa)_2$·diglyme precursor that is liquid at 45°C and guarantees this carrier concentration at the chosen deposition conditions. Worthy of note, our results are in tune with data obtained by Marks et al. for other MOCVD of CdO thin films.[53] Therefore, it can be stressed that the MOCVD technique is well suited to obtain CdO films with such high carrier concentrations.

The mobility values range from 2.3 to 6.2 cm^2 / Vs, increasing with increasing temperature above 100 K. The values are considerably lower than those reported for CdO samples with lower carrier densities. This can be due to the high carrier concentration responsible for an increased scattering from ionized impurities and/or grain boundaries.[54-55] The best fit of the experimental data in the high temperature regime showed that the mobility trend is $\propto T^{1.04}$. These results, in terms of carrier concentration and mobility, are somewhat different to those observed by Farahani *et al.*[17] who found that the mobility decreased with increasing temperature above 100 K. It was found that the resistivity of the CdO film slightly decreases from 3.3 x 10^{-3} to 1.4 x 10^{-3} Ω cm as the temperature increases from 80 to 460 K due to the increased mobility.[55]

In order to evaluate the electron transport character of these CdO films, we investigated the temperature dependence of the conductivity, σ, calculated from the resistivity measurements. Figure 4.1.9 shows the Arrhenius plot of the conductivity (σ versus 1 / kT). It can be noticed that σ remains rather constant up to a critical temperature, T_c, beyond which it increases with increasing temperature.

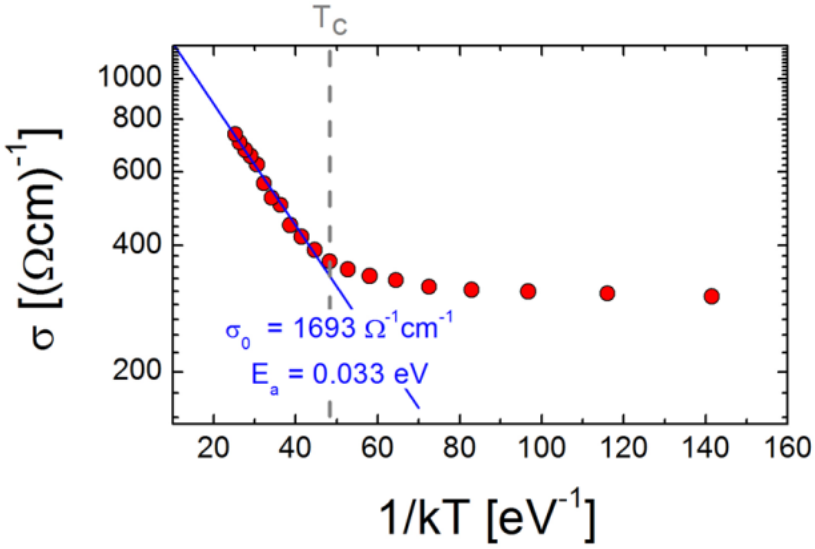

Figure 4.1.9. Dark conductivity vs. temperature for the CdO film. The solid line represents the best-fit analysis (Eq. 1) for temperatures above T_c. The corresponding extracted σ_0 and E_a values are 1693 Ω^{-1} cm^{-1} and 0.033 eV, respectively.

This variation of the conductivity upon the temperature suggests that more than one conduction mechanisms are involved in CdO. In the low temperature regime CdO behaves as a degenerate semiconductor and the conductivity is almost temperature independent. Above T_c, CdO shows semiconducting properties and the conduction takes place with an activated process described by the following relation:

$$\sigma(T) = \sigma_o \exp\left(-\frac{E_\sigma}{kT}\right)$$

where k denotes the Boltzmann's constant, T is the absolute temperature, E_a is the activation energy, and σ_0 represents the pre-exponential factor. Following this relation, E_a and σ_0 values of 0.033 eV and 1693 $\Omega^{-1}cm^{-1}$, respectively, were obtained. This rather low activation energy can be associated with hopping of carriers between quasi-

localized states at grain boundaries.[56]

It is important to point out that this study does not really allow us to identify the nature of compensating defects as cation vacancies, interstitial oxygen or more complex defect clusters. In addition, it is not possible to exclude the role of defects at the grain boundaries as partially responsible for the high carrier concentration found in the present CdO films.

Nowadays sensing and treatment of toxic and harmful compounds is of primary importance. In this context, different procedures have been experimented for water treatment,[57-60] and among them, the photocatalytic method seems the most promising technique to remove contaminants from aqueous solutions. In this field semiconductor nanomaterials already demonstrated to be effective for water treatment.[61-62] The most used semiconductor materials are based on ZnO and TiO_2 metal oxides.[63-68] Much lower data have been reported for the CdO system.[69-70] Thus, after synthesizing conducting CdO thin films, we exploited their ability to act as photocatalysts for water treatments.[71]

4.1.4 CdO Thin Films as Photocalysts for Water Treatments

The potential photocatalytic activity of the CdO thin films was evaluated towards the selected methyl orange model dye (Figure 4.1.10).[63]

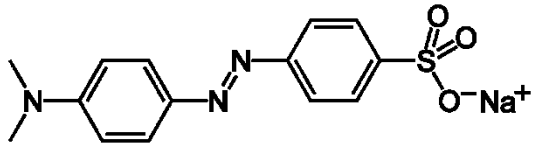

Figure 4.1.10. Methyl orange.

Photocatalytic experiments were carried out in a photoreactor of 50 mL using two 365 nm lamps of 8 W per each (Helios Italquartz). A CdO film of 0.8 cm^2 was used as catalyst. All the experiments were performed using the methyl orange model dye with an initial concentration of 4.2 x 10^{-5} M. The solution was prepared by dissolving the

dye in water CHROMASOLV Plus (Aldrich). The total solution volume was 20 mL and the duration of each irradiation experiment was 20 min. 3.5 x 10^{-4} mol of H_2O_2 was added in the starting solution and no pH adjustment was performed. UV-vis measurements of the reacting solution were performed every 5-20 min.[64] During the irradiation the solution was stirred using a Vortex VELP SCIENTIFICA 50 rpm. The overall irradiation time needed to totally decolorize the solution was 380 min (Figure 4.1.11).

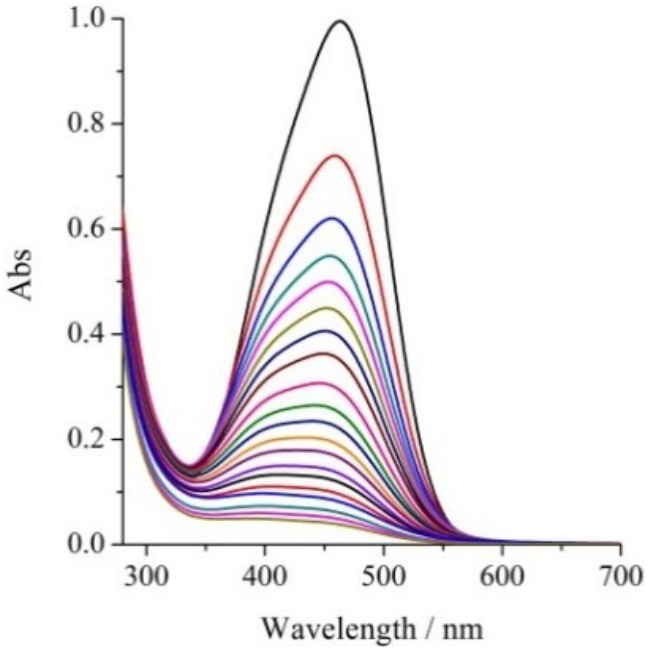

Figure 4.1.11. UV-vis spectra of the starting 20 mL 4.2 x 10^{-5} M methyl orange water solution and after cycles of 20 min irradiation, in presence of a CdO film of 0.8 cm^2, followed by UV-vis measurement. The total irradiation time was 380 min.

Figure 4.1.12 shows the absorbance variation of the band maximum at 463 nm vs. the irradiation time. After 1 h irradiation the absorbance was the 54% of its initial value. This result demonstrates a good performance of the CdO photocatalyst to remove the methyl orange dyes by illumination.

The decolorizing efficiency can be defined as follows: $[(C_i - C_t)/C_i] \times 100$ where C_i represents the starting solution concentration and C_t represents the dye concentration at the time t.[70] After 380 min irradiation the remaining dye was only the 3.8 % (Figure 4.1.13).

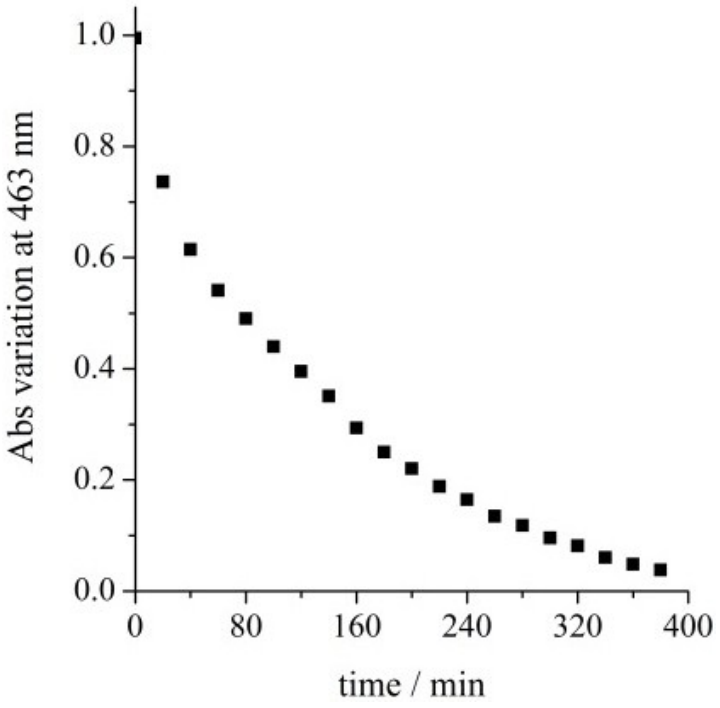

Figure 4.1.12. Absorbance variation of the 20 mL 4.2 x 10^{-5} M methyl orange water solution, in presence of a CdO film of 0.8 cm^2, vs the irradiation time.

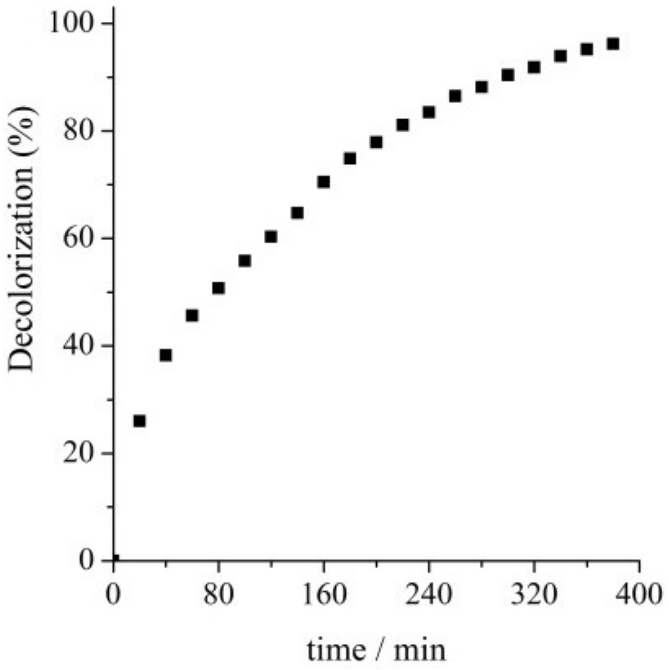

Figure 4.1.13. Decolorizing efficiency of the 20 mL 4.2 x 10^{-5} M methyl orange water solution, in presence of a CdO film of 0.8 cm^2, vs the irradiation time.

It emerges that the CdO thin film catalyzes the almost total decomposition of the

methyl orange solution after 4 h light irradiation. It is important to bear in mind that these experiments have been performed using a CdO film having an area of just 0.8 cm^2. As a consequence the required time to decolorize the starting methyl orange water solution is due to this small reacting surface-solution interface. The reactivity of the CdO photocatalysts depends on the number of electron/hole pairs generated in the conduction/valance bands respectively when the catalyst surface is irradiated. Therefore the reactive species are the superoxide anion O_2^- and the hydroxyl radical $OH^{\cdot}$ obtained on the surface of the CdO film.

Figure 4.1.14 shows the behaviour of $\ln(C_i/C_t)$ vs. the irradiation time. A first order kinetics was observed and the evaluated rate constant was found 0.0079 min^{-1}.[70]

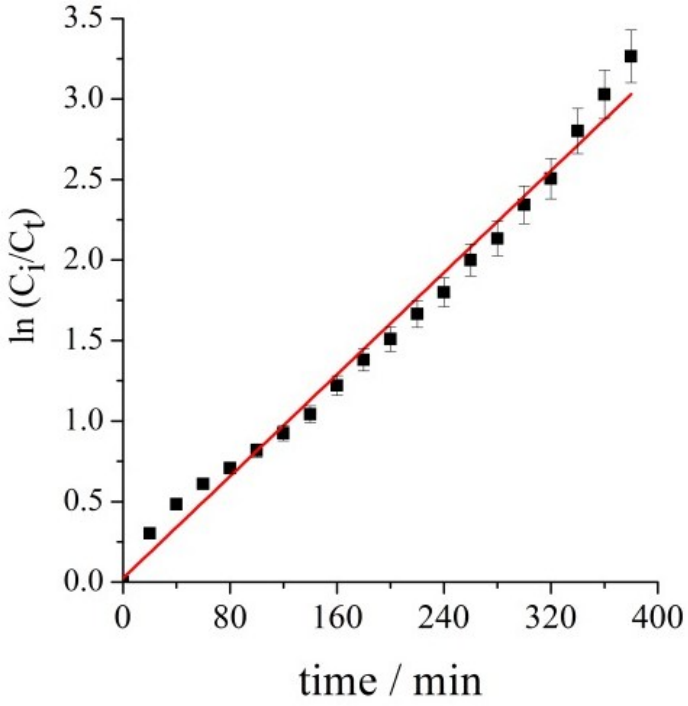

Figure 4.1.14. Decolorizing efficiency of the 20 mL 4.2 x 10^{-5} M methyl orange water solution vs the irradiation time. R^2 of the fit = 0.99.

In order to check on the photolysis of the methyl orange without catalyst in the same experimental conditions, we irradiated with a 365 nm lamp 20 mL of a 4.2 x 10^{-6} M methyl orange water solution (pH = 4.43) containing 14 µL H_2O_2 30%. Experimental evidences no doubt indicate that after 20 min irradiation the

photocatalytic activity of the CdO film results in a 100 % increase in the decolorizing efficiency (Figure 4.1.15).

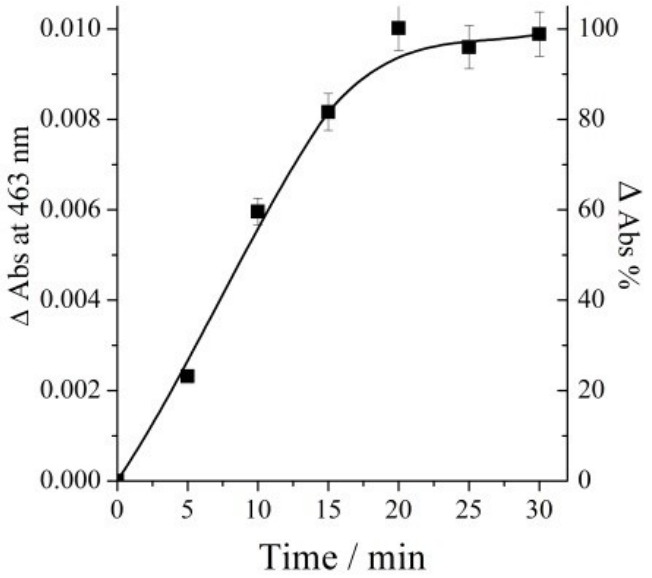

Figure 4.1.15. Difference of the decolorizing efficiency, in presence and absence of catalyst, of 20 mL 4.2 x 10^{-6} M methyl orange water solution vs the irradiation time.

In the light of the obtained results it is possible to state that these synthesized CdO thin films could have considerable potential for application as materials for water treatment.

Conclusions

We exploited the properties of CdO thin films that show both good transparency in the visible region with a transmittance that reaches over 85% and a high free-electron concentration. XRD measurements confirmed the presence of a single cubic rocksalt phase, although a grain structure with typical lateral dimensions of order 80−400 nm was found in AFM. Electrical characterization and the direct allowed optical absorption onset evaluated from the optical spectra both indicate that these CdO films behave as highly degenerate semiconductors, with a Fermi level well above the bottom of the conduction band. The carrier density is estimated to be about $7-8 \times 10^{20}$ cm^{-3}. This is further confirmed by the presence of very strong satellite structure associated with conduction electron plasmon satellite excitation in core XPS. The presently found carrier concentration, according to other previously reported data, is larger than the maximum carrier concentration predicted by recent quantum mechanical calculations, and we gave a rationale for this. All the present results were highly repeatable. The films studied in the present work are suitable for self-assembly of molecular building-blocks for solar cells applications.

Finally, CdO thin films also showed interesting properties as catalyst in the field of water treatment.

References

[1]D. A. Cristaldi, S. Millesi, I. Crupi, G. Impellizzeri, F. Priolo, R. M. J. Jacobs, R. G. Egdell, A.Gulino *J. Phys. Chem. C*, **2014**, 118, 15019-15026.

[2] Ingram, B. J.; Gonzalez, G. B.; Kammler, D. R.; Bertoni, M. I.; Mason, T. O. *J. Electroceram*. **2004**, *13*, 167–175.

[3] Granqvist, C. G.; Hultaker, A. *Thin Solid Films* **2002**, *411*, 1-5.

[4] Ginley, D. S.; Bright, C. *MRS Bull.* **2000**, *25*, 15-21.

[5] Gordon, R. G. *MRS Bull.* **2000**, *25*, 52-57.

[6] Yu, K.M.; Mayer, M. A.; Speaks, D. T.; He, H.; Zhao, R,; Hsu, L.; Mao, S.S.; Haller, E.E.; Walukiewicz, W. *J. Appl. Phys.* **2012**, *111*, /1-123505/5.

[7] Hiesinger, L.; Konig, H.; Festschr. W. C. *Heraeus* **1951**, 376-392.

[8] Helwig, G. Zeitschr. *Phys.* **1952**, *132*, 621-642.

[9] Schumm, B.; Wollmann, P.; Fritsch, J.; Grothe, J.; Kaskel, S. *J. Mater. Chem.*, **2011**, *21*, 10697-10704.

[10] Yang, Y.; Jin, S.; Medvedeva, J. E.; Ireland, J. R.; Metz, A. W.; Ni, J.; Hersam, M. C.; Freeman, A. J.; Marks, T. J. *J. Am. Chem. Soc.* **2005**, *127*, 8796-8804.

[11] Gulino, A.; Tabbi, G. *App. Surf. Sc.* **2005**, *245*, 322-327.

[12] Li, X.; Gessert, T. A.; Coutts, T. *App. Surf. Sci.* **2004**, *223*, 138-143.

[13] Maity, R.; Chattopadhyay, K. K. *Sol. Energy Mater. Sol. Cells* **2006**, *90*, 597-606.

[14] McGuinness, C.; Stagarescu, C. B.; Ryan, P. J.; Downes, J. E.; Fu, D.; Smith, K. E.; Egdell R. G. *Phys. Rev. B* **2003**, *68*, 165104/1-165104/10.

[15] Burbano, M.; Scanlon, D. O.; Watson, G. W. *J. Am. Chem. Soc.* **2011**, *133*, 15065–15072.

[16] Dou, Y.; Egdell, R. G.; Law, D. S. L.; Harrison, N. M.; Searle, B. G. *J. Phys.: Condens. Matter.* **1998**, *10*, 8447–8458.

[17] Vasheghani Farahani, S. K.; Muñoz-Sanjosé, V.; Zúñiga-Pérez, J.; McConville, C. F. Veal, T. D. *App. Phys. Lett.* **2013**, *102*, 022102-022106.

[18] Zhu, Y.; Mendelsberg, R. J.; Zhu, J.; Han, J.; Anders, A. *J. Phys. D: Appl. Phys.* **2013**, *46*, 195102-195107.

[19] Walsh, A.; Da Silva, J. L. F.; Wei, S-H.; Körber, C.; Klein, A.; Piper, L. F. J.; DeMasi, A.; Smith, K. E.; Panaccione, G.; Torelli, P.; Payne, D. J.; Bourlange, A.; Egdell, R. G. *Phys. Rev. Lett.* **2008**, *100*, 167402/1-4.

[20] King, P. D. C.; Veal, T. D.; Fuchs, F.; Wang, C. Y.; Payne, D. J.; Bourlange, A.; Zhang, H. L.; Bell, G. R.; Cimalla, V.; Ambacher, O.;. Egdell, R. G.; Bechstedt, F.; McConville, C. F. *Phys. Rev. B* **2009**, *79*, 205211/1-10.

[21] Froehlich, D.; Kenklies, R.; Helbig, R. *Phys. Rev. Lett.* **1978**, *41*, 1750-1751.

[22] Gulino, A.; Compagnini, G.; Scalisi, A. A. *Chem. Mater.* **2003**, *15*, 3332-3336.

[23] Dou, Y.; Fishlock, T.; Egdell, R. G.; Law, D. S. L.; Beamson, G. *Phys. Rev. B* **1997**, *55*, R13381-R13384.

[24] Clark, S. J.; Robertson, J.; Lany, S.; Zunger, A. *Phys. Rev. B* **2010**, *81*, 115311/1-115311/5.

[25] Singh, A. K.; Janotti, A.; Scheffler, M.; Van de Walle, C. G. *Phys. Rev. Lett.* **2008**, *101*, 055502/1-055502/4.

[26] Varley, J. B.; Weber, J. R.; Janotti, A.; Van deWalle, C. G. *Appl. Phys. Lett.* **2010**, *97*, 142106/1-142106/3.

[27] Lany, S.; Zunger, A. *Phys. Rev. Lett.* **2011**, *106*, 069601/1.

[28] King, P. D. C.; Veal, T. D.; Jefferson, P. H.; Zúñiga Pérez, J.; Muñoz Sanjosé, V.; Mc-Conville, C. F. *Phys. Rev. B* **2009**, *79*, 035203/1–035203/5.

[29] Jin, S.; Yang, Y.; Medvedeva, J. E.; Wang, L.; Li, S.; Cortes, N.; Ireland, J. R.; Metz, A. W.; Ni, J.; Hersam, M. C.; Freeman, A. J.; Marks, T. *J. Chem. Mater.* **2008**, *20*, 220–230.

[30] Bhosale, C. H.; Kambale, A. V.; Kokate, A. V.; Rajpure, K. Y. *Mater. Sci. Eng. B* **2005**, *122*, 67-71.

[31] Ristic, M.; Popovic, S.; Music, S. *Mater. Lett.* **2004**, *58*, 2494-2499.

[32] Han, X.; Liu, R.; Xu, Z.; Chen, W.; Zheng, Y. *Electrochem. Commun.* **2005**, *7*, 1195-1198.

[33] Gulino, A.; Castelli, F.; Dapporto, P.; Rossi, P.; Fragalà, I. *Chem. Mater.* **2002**, *14*, 704-709.

[34] Cristaldi, A.; Impellizzeri, G.; Priolo, F.; Gupta, T.; Gulino, A. *J. Phys. Chem. C.* **2012**, *116*, 3363-3368.

[35] Beatham, N.; Cox, P. A.; Egdell, R. G.; Orchard, A. F. *Chem. Phys. Lett.* **1980**, *69*, 479-482.

[36] Campagna, M.; Wertheim, G. K.; Shanks, H. R.; Zumsteg, F.; Banks E. *Phys. Rev. Lett.* **1975**, *34*, 738-741.

[37] Chazalviel, G. W. J. N.; Campagna, M.; Shanks, H. *Phys. Rev. B* **1977**, *16*, 697-705.

[38] Egdell, R. G.; Rebane, J.; Walker, T. J.; Law, D. S. L. *Phys. Rev. B* **1999**, *59*, 1792-1799.

[39] Payne, D. J.; Egdell,R. G.; Hao, W.; Foord, J. S.; Walsh, A. Watson, G. W. *Chem. Phys. Lett.* **2005**, *411*, 181-185.

[40] Piper, L. F. J.; Jefferson, P. H.; Veal, T. D.; McConville, C. F.; Zúñiga-Pérez, J.; Muñoz-Sanjosé V. *Superlattices and Microst.* **2007**, *42*, 197–200.

[41] Steiner, P.; Hoechst, H.; Hufner, S. *Photoemission in Solids II* , **1979**, 26.

[42] Chang, J. J.; Langreth, D. C. *Phys. Rev. B: Solid State* **1972**, *5*, 3512-3522.

[43] Langreth, D. C. Proceedings of Nobel Symposium 24 in Medicine and Natural Science, edited by B. Lundqvist and S. Lundqvist Academic Press, New York and London, 1973, 210.

[44] Egdell, R. G.; Walker, T. J.; Beamson, G. J. *Electr. Spectr. Rel. Phen.* **2003**, *128*, 59-66.

[45] Payne, D. J.; Egdell, R. G.; Law, D. S. L.; Glans, P-A.; Learmonth, T.; Smith, K. E.; Guo, J.; Walsh, A.; Watson, G. W. *J. Mater. Chem.* **2007**, *17*, 267 – 277.

[46] Körber, C.; Krishnakumar, V.; Klein. A.; Panaccione, G.; Torelli, P.; Walsh, A.; Da Silva, J.L.F.; Wei, S.-H. *Phys. Rev. B.* **2010**, *81*, 165207/1-165207/9.

[47] Dou, Y.; Egdell, R. G.; Walker, T.; Law, D. S. L.; Beamson, G. *Surf. Sci*. **1998**, *398*, 241-258.

[48] Jefferson, P. H.; Hatfield, S. A.; Veal, T. D.; King, P. D. C.; McConville, C. F.; Zúñiga-Pérez, J.; Muñoz-Sanjosé V. *Appl. Phys. Lett.* **2008**, *92*, 022101/1022101/3.

[49] Haul, R.; Just, D. J*App. Phys.* **1962**, *33*, 487-493.

[50] Hanamura, E. *J. Phys. Soc. Jpn.* **1970**, *28*, 120-127.

[51] Van Der Pauw L. J. *Philips Tech. Rev.* **1958**, *20*, 220-224.

[52] Yan, M.; Lane, M.; Kannewurf, C. R.; Chang, R. P. H. *Appl. Phys. Lett.* **2001**, *78*, 2342-2344.

[53] Metz, A. W.; Ireland, J. R.; Zheng, J-G.; Lobo, R. P. S. M.; Yang, Y.; Ni, J.; Stern, C. L.; Dravid, V. P.; Bontemps, N. Kannewurf, C. R.; Poeppelmeier, K. R.; Marks, T. J. *J. Am. Chem. Soc*. **2004**, *126*, 8477-8492.

[54] Seeger, K. Semiconductor Physics, Springer-Verlag, Berlin, 1985, 3rd ed., 160.

[55] Kammler, D. R.; Harder, B. J.; Hrabe, N. W.; McDonald, N. M.; Gonzalez, G. B.; Penake, D. A.; Mason, T. O. *J. Am. Ceram. Soc*. **2002**, *85*, 2345–2352.

[56] Bottger, H.; Bryksin V. V. Hopping Conduction in Solids, VCHVerlagsgesellschaft, Weinheim, Germany, 1985.

[57]K.A. Verma, R.R. Dash, P. Bhunia, *J. Environ. Manag.* **2012**, *93*, 154.

[58] Sh. Cheng, D.L. Oatley, P.M. Williams, Ch.J. Wright, *Water. Res* **2012**, *46*, 33.

[59] R. Rahimi, H. Kerdari, M. Rabbani, M. Shafiee, *Desalination* **2011**, *280*, 412.

[60] A. Afkhami, R. Moosavi, *J. Hazard. Mater.* **2010**, *174*, 398.

[61] S.T. Hung, C.J. Chang, M.H. Hsu, *J. Hazard. Mater.* **2011**, *198*, 307.

[62] D.P. Agatino, E. García-López, G. Marcí, L. Palmisano, *J. Hazard.* Mater **2012**, *3*, 211–212.

[63] M. Huang, C. Xu, Z. Wu, Y. Huang, J. Lin, J. Wu, *Dyes and Pigments* **2008**, *77*, 327-334.

[64] J. Fernández, J. Kiwi, J. Baeza, J. Freer, C. Lizama, H.D. Mansilla *Applied Catalysis B: Environmental* **2004**, *48*, 205–211.

[65] S. Baruah, S.K. Pal, J. Dutta *Nanoscience & Nanotechnology-Asia*, **2012**, *2*, 90-102.

[66] Y. Abdollahi, A.H. Abdullah, Z. Zainal, N.A. Yusof, *Int. J. Mol. Sci.* **2012**, *13*, 302-315.

[67] I.T. Peternel, N. Koprivanac, A.M. Lončarić Božić, H.M. Kušić. *J. Hazard. Mater.* 2007, *148*, 477–484.

[68] P. Sathishkumar, R. V. Mangalaraja, O. Rozas, H. D. Mansilla, M. A. Gracia-Pinilla, S. Anandan, *Ultrasonics sonochemistry* **2014**, *21*, 1675-1681.

[69] A. Yousef, N.A.M. Barakat, T. Amna, A.R. Unnithan, S.S. Al-Deyabe, H.Y. Kim, *J. Lumin* **2012**, *132*, 1668-1677.

[70] T. Azadeh, I. Mina, K. Hamed. Materials Research Bulletin **2013**, *48*, 935-942.

[71] **S. Millesi**, M. Schilirò, F. Greco, I. Crupi, G. Impellizzeri, F. Priolo, R.G. Egdell, A. Gulino *Materials Science in Semiconductor Processing*, In Press.DOI: 10.1016/j.mssp.**2015**.08.005.

Chapter 5

SAMs for Catalytic Applications

The methodology of the covalent assembly can be adopted also for molecular entities showing catalytic properties thus obtaining heterogeneous catalytic materials. In fact, often the catalyst heterogenization enhances the catalytic performance as a consequence of the major acquired stability, activity, selectivity, recover and recycle,[1-11]. In this chapter we show the synthesis of a nanostructured system based on the covalent bonding of some (salen)Mn(III) molecules on the surface of glass beads.

5.1 Synthesis and Characterization of a (salen)Mn(III) Complex

The asymmetric epoxidation of unfunctionalized prochiral olefins, catalysed by homogeneous chiral (salen)Mn(III) complexes, is an important viable route to obtain chiral epoxides.[12] In fact, the obtained chiral epoxides contain two new stereocentres and can be easily transformed into a large variety of compounds active in many other technological fields.[8,13-22]

A recent paper showed that the trend in the catalytic performance in the asymmetric epoxidation of some alkenes using some (salen)Mn catalysts immobilized inside nanopores was dependent on the different rigidity of the catalyst-substrate linkage.[23] In fact, it seems that for immobilised (salen)Mn catalysts, a rigid linkage connecting active centres to the support is essential to obtain activity and enantioselectivity as high as those obtained in homogeneous systems. It emerges that the immobilisation strategy plays a fundamental role in this field.[24] In the same context, it has been reported that a covalent monolayer of (salen)Mn(III) molecules with two pendant amino functionalities on flat silica substrates acts as an active heterogeneous catalyst for enantioselective epoxidation of a selected alkene with huge turnover values.[25] Moreover, the experimental photoelectron evidences confirmed the formation of the surface confined $O=Mn^{V}$(salen) oxene active species for the substrate epoxidation reaction.[25]

In this context, a new (salen)Mn(III) complex (Scheme 5.1.1) with only one pendant amino group was grafted on the surface of some glass beads (Scheme 5.1.2) with the aim to test the catalytic activity upon grafting on a large surface area.

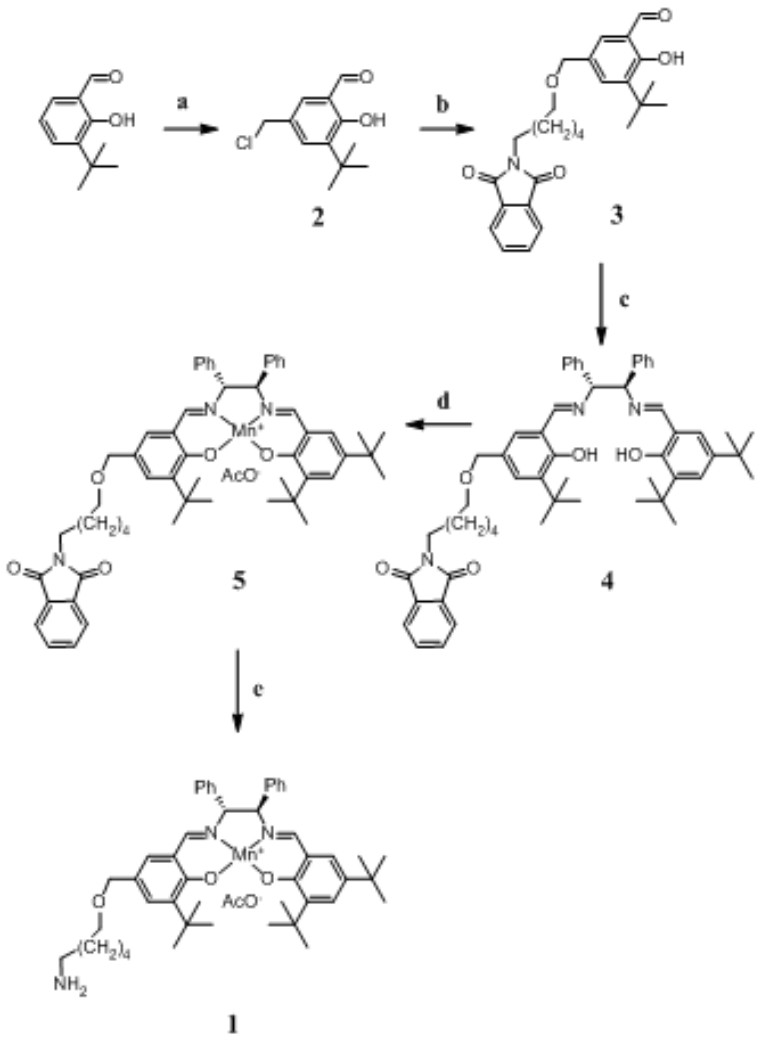

Scheme 5.1.1. Synthetic pathway for the (salen)Mn(III) catalyst.

5.1.1 Synthesis of SAMs of (salen)Mn(III) Complex

Glass beads having a 3 mm diametre, underwent the typical silanization. After silanization these were immersed in a freshly prepared 9.5 $\times 10^{-4}$ M toluene solution of the (salen)Mn(III) and kept at 90 °C for 72 h while stirring to obtain the covalent grafting of the (salen)Mn(III) molecules on the substrate surface. The (salen)Mn(III) monolayers on glass beads (hereafter Mn_MGB) thus formed were left to cool to room temperature and then sonicated (two times) 10 min with toluene to remove any residual unreacted Mn complex (Scheme 5.1.2). The final systems resulted robust and the grafted molecules were found to be insoluble in toluene, MeCN, THF and EtOH.

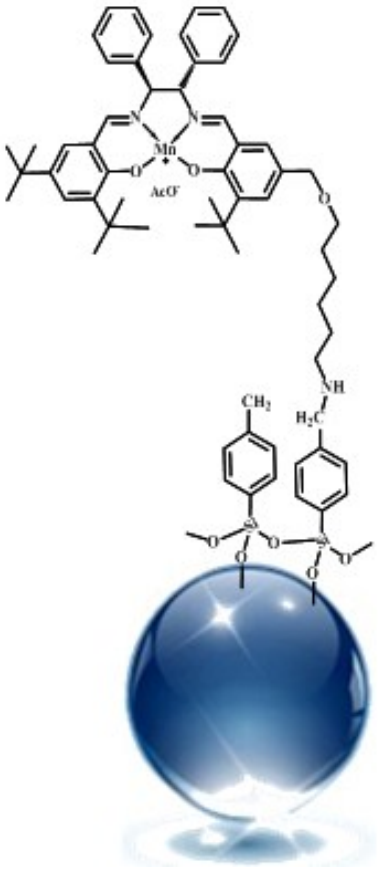

Scheme 5.1.2 Schematic representation of the Mn_MGB

5.1.2 Characterization of the (salen)Mn(III) Complex SAMs

The Mn_MGB system was characterised by UV-Vis measurements and Figure 5.1.1 shows the absorption spectra of a toluene (salen)Mn(III) 5.7 x 10^{-6} M solution (black line) and of a representative Mn_MGB (red line).

The solution UV-Vis shows two bands: the first centred at 296.4 nm with two weak bands at 286.2 and 306.4 nm and the second at 374.2 nm with a shoulder at 393.0 nm. These two bands are consistent with the $\pi \rightarrow \pi^*$ and $n \rightarrow \pi^*$ transitions of the (salen)Mn(III) complex, respectively.[25] The Mn_MGB UV-Vis spectrum closely resembles that of the solution with two features at 287.4 and 302.8 and another band at 366.1 nm with a shoulder at 388.6 nm. The calculated molecule surface coverage is 7.8 x 10^{13} molecules/cm^2.[26] This value is almost two times larger than that already

reported for its parent system with two pendant groups and confirms the main objective of this new synthetic design.[12] The resulting footprint is 128 $Å^2$ per molecule.

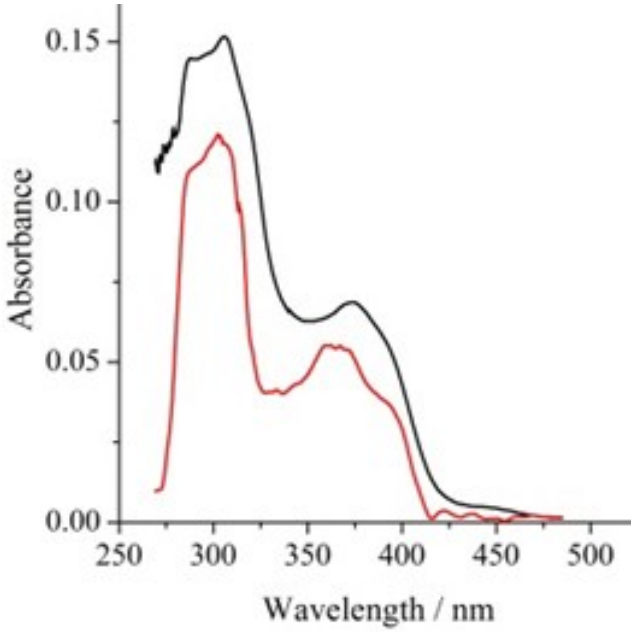

Figure 5.1.1. UV-Vis spectra of a 5.7 x 10^{-6} M toluene solution (black line) of (salen)Mn(III) complex and of a representative Mn_MGB (red line).

The electronic structure of the Mn_MGB, stacked on an appropriate double side scotch tape (Figure 5.1.2), was investigated by XPS technique.

Figure 5.1.2. Set-up for XPS measurements of Mn_MGB.

XPS measurements were acquired at 45° take-off angle and spectra were excited with monochromatized Mg-Kα radiation. Figure 5.1.3 shows the XP spectrum of the Mn_MGB system in the Mn 2p binding energy region and the presence of the two spin-orbit components at 641.8 and 653.7 eV, partially overlapped with the high energy shake-up satellites, is typical of Mn(III) species.[25,27]

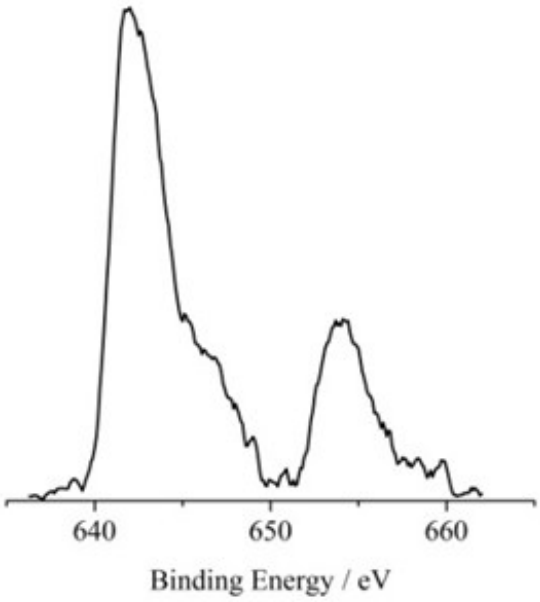

Figure 5.1.3. Monochromatised Mg Kα excited XPS of a representative Mn_MGB in the Mn 2p binding energy region.

Figure 5.1.4 shows the XPS of Mn_MGB in the N 1s binding energy region. On the basis of a localized bonding scheme, the (salen)Mn(III) shows two imine and one amine nitrogens in the formula unit. The photoelectron spectrum of the grafted complex shows a rather symmetric N 1s signal at 400.0 eV as a consequence of some electronic level reorganization of the imine functionalities upon the Mn(III) complexation.[25] On the basis of the XPS atomic concentration analysis a surface coverage of 5.7 x 10^{13} was estimated and this value is rather close to that obtained by UV-Vis measurements.[28]

Moreover the molecular size of (salen)Mn(III) on the surface was estimated using an MM^{+} calculation (HyperChem 7.5) and Figure 5.1.5 shows the geometry arrangement.

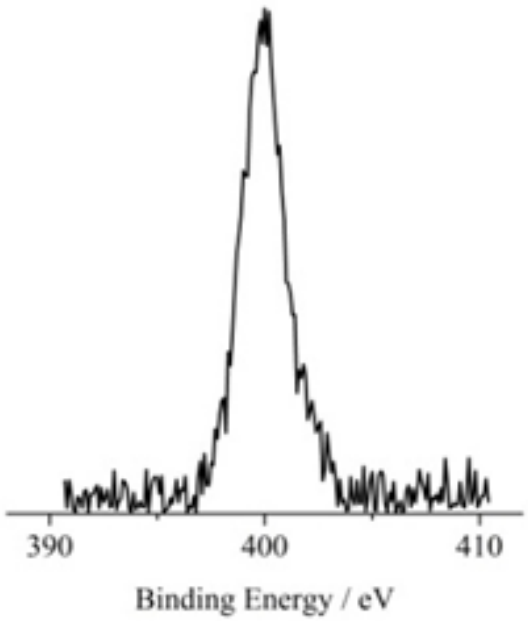

Figure 5.1.4. Mg Kα excited XPS of the Mn_MGB in the N 1s binding energy region.

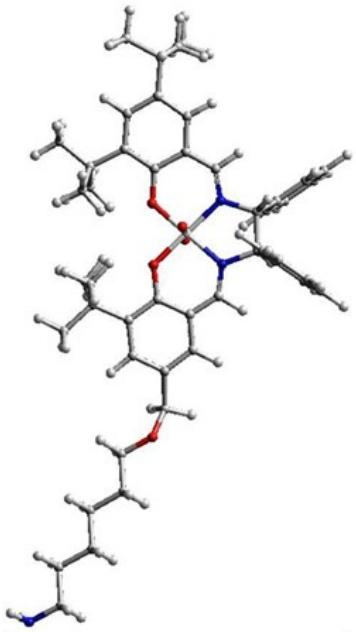

Figure 5.1.5. MM^{+} optimization of the size of (salen)Mn(III) complex.

On the basis of these calculations the occupied area on the substrate is of 134.7 $Å^2$ per molecule. This value is strongly reminiscent of that obtained with UV-Vis measurements and confirms the high density of (salen)Mn(III) on the bead surfaces.

Finally, the surface morphology of the functionalised glass beads was investigated by AFM measurements. Figure 5.1.6 shows Mn_MGB system surfaces mainly consisting of grains with lateral dimensions of order 300-700 nm. The average roughness of the films is typically around 13.9 nm and with a total range of 97.0 nm in the images.

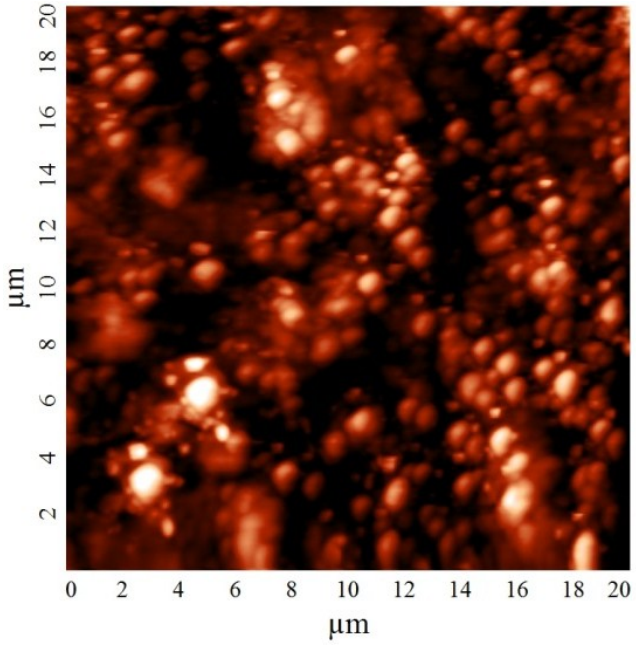

Figure 5.1.6. AFM micrograph of a representative Mn_MGB.

5.1.3 Catalytic Properties of the (salen)Mn(III) Complex SAMs for Olefin Epoxidation

In order to test the activity of the Mn_MGB system as catalyst in epoxidation reactions the following four alkenes 6-cyano-2,2-dimethylchromene, *cis*-β-ethylstyrene, 1,2-dihydronapthalene and indene were selected. Moreover, the epoxidation measurements were carried out both in solution and with the Mn_MGB system. In particular, for solution experiments (Table 5.1.1) the (salen)Mn(III) catalyst shows a naphthylamide group to protect the amino functionality (catalyst **5** in Scheme 5.1.1). Results indicate that for Mn_MGB the reaction time for the total conversion decreases as the number of glass beads used in the reaction media increases. The enantiomeric excess values (85-91%) are slightly higher than the corresponding ones

(80%) obtained in solution. As expected, TON and TOF values are in the range 10^4 – 10^5 and 10^2 – 10^3 respectively. Table 5.1.2 also shows that the addition of 4-phenylpyridine n-oxide (PPNO) does not significantly influence the e. e. and conv. values.

Table 5.1.1. Results obtained for the solution epoxidation of selected alkenes using the catalyst **5** at 25°C. In all these experiments 0.081 mmol of alkene and 5% of catalyst **5** were dissolved in 1 mL of CH_2Cl_2; NaClO was 0.81 mmol and the total volume of the reacting solutions, buffered with 1 mL 0.05 M Na_2HPO_4 at pH = 11.2, was 3 mL. [a]determined by GC on a specific chiral column. [b]TON= mmol of the overall products/mmol of the catalyst. [c] TOF = TON/reaction time (h).[d]*cis/trans* = 5.

Alkene	Time (h)	Conv (%)[a]	*e.e.*(%)[a]	TON[b]	TOF[c]
6-cyano-2,2-dimethylchromene	2	100	80	20	10
Cis-β-ethylstyrene	7	100	70 (cis) 80 (trans)[d]	18	3
1,2-dihydronapthalene	2	100	78	20	10
Indene	2	100	95	20	10

Table 5.1.2. Results for the epoxidation of the 6-cyano-2,2-dimethylchromene into 3,4 epoxy-6-cyano-2,2,-dimethylchromene using the Mn_MGB. In all these experiments 0.081 mmol of 6-cyano-2,2-dimethylchromene were dissolved in 1 mL of CH_2Cl_2; NaClO was 0.81 mmol and the total volume of the reacting solutions, buffered with 1 mL 0.05 M Na_2HPO_4 at pH = 11.2, was 3 mL. [a]determined by GC on a dimethyl-pentyl-beta (DIMEPEBETA-086) chiral column, (25 m x 0.25 mm ID, 0.25 µm film). [b] TON = mmol of the overall products/mmol of the catalyst. [c] TOF = TON/reaction time (h).

Number of glass bead Catalyst	Reaction Time / h	e. e %[a]	Conv. %[a]	TON[b]	TOF[c] (h^{-1})
10	7	88	5	6202	886
	24	86	15	18606	775
	48	85	35	43415	904
	72	87	55	68224	948
	96	85	75	93032	969
	130	86	100	124043	982
30	7	89	12	5036	719
	24	88	25	10492	437

	48	87	50	20984	437
	72	88	75	31477	437
	96	87	100	41969	437
60	7	87	30	6183	883
	24	89	45	9275	386
	48	87	77	15870	331
	72	85	100	20611	286
60 + PPNO	7	90	29	5977	854
	24	91	47	9687	404
	48	91	78	16076	335
	72	90	100	20611	286

In order to check on the robustness of the Mn_MGB the above epoxidation process was repeated 7 times for 24 h. After each cycle, the beads were washed with water and dichloromethane and then reused for the next cycle. Figure 5.1.7 shows that both enantiomeric excess values and conversion % remained almost unaltered thus confirming the high stability of the present heterogeneous catalyst.

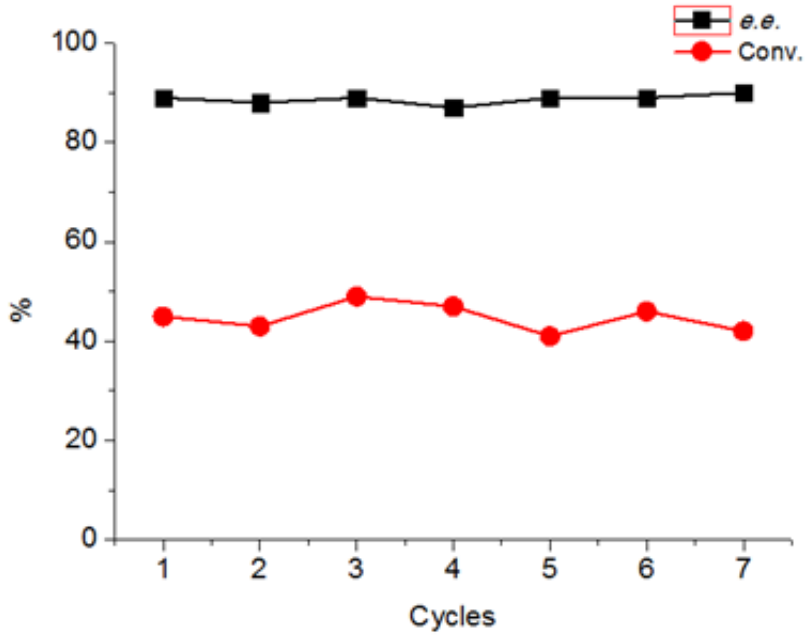

Figure 5.1.7. Variations of e.e. and conv. after reusing of 60 spheres (beads) in the epoxidation of 6-cyano-2,2-dimethylchromene for 24 h with the Mn_MGB.

Table 5.1.3 shows the epoxidation data obtained using the cis-β-ethylstyrene as substrate. Reaction times are similar to those previously observed for the 6-cyano-2,2-dimethylchromene, and also in this case the detected enantiomeric excesses are higher with respect to those observed in solution (Table 5.1.1). However, an inversion of the

cis/*trans* ratio was observed: in solution, the catalyst leads mainly to the *cis* isomer (*cis*/*trans* = 5), while Mn_MGB predominantly generates the *trans* isomer (90%).

Table 5.1.3. Results for the epoxidation of cis-β-ethylstyrene at 25°C using the Mn_1_MGB. In all these experiments 0.081 mmol of cis-β-ethylstyrene were dissolved in 1 mL of CH_2Cl_2; NaClO was 0.81 mmol and the total volume of the reacting solutions, buffered with 1 mL 0.05 M Na_2HPO_4 at pH = 11.2, was 3 mL. [a]determined by GC on a DiAcTBuSiliBETA-ov-1701 chiral column, (25 m x 0.25 mm ID, 0.25 μm film), *[trans]/[cis]* = 7. [b]TON = mmol of the overall products/mmol of the catalyst. [c] TOF = TON/reaction time (h).

Number of glass bead Catalyst	Reaction Time / h	e. e cis %[a]	e. e. trans %[a]	Conv. %[a]	TON[b]	TOF[c] (h^{-1})
10	7	80	89	17	20958	2994
	24	80	90	29	35556	1482
	48	83	89	56	69275	1443
	72	84	90	73	91095	1265
	96	84	91	100	124043	1292
30	7	80	88	29	12106	1729
	24	81	90	54	22798	950
	48	83	91	89	37454	780
	72	84	88	100	41969	583
60	7	72	88	40	8310	1187
	24	81	86	70	14433	601
	48	85	88	94	19355	403
	72	85	87	100	20611	286
60 + PPNO	7	89	91	49	10051	1436
	24	88	92	77	15951	665
	48	88	91	93	19245	401
	72	89	91	100	20611	286

Very recently Zhang and Wang reported that for immobilized (salen)Mn catalysts, a rigid linkage connecting active centres to the support is essential to obtain activity and enantioselectivity as high as obtained in homogeneous systems.[23] In fact, the immobilised catalyst with a flexible linkage gave lower chemical selectivity, enantioselectivity and inverted *cis*/*trans* ratio compared to the homogeneous Jacobsen catalyst and to the immobilized catalyst with a rigid linkage. This is possible because of the rotation of the C-C bond in radical intermediates that affects the *cis*/*trans* ratio. In our case as well as in the Zhang's and Wang's case, the linkages are connected to the 6-position in the salen ligand, which is far from the Mn(III) atoms. Moreover, the only difference between the catalyst we used for homogeneous solution reactions and

the catalyst anchored onto the glass beads (Mn_MGB) is the naphthylamide group used to protect the amino group and this is unlikely to result in the different chemical selectivity to epoxides, *cis*/*trans* ratio and e. e. values. Therefore, the inversion of the *cis*/*trans* ratio we observed from homogeneous to heterogeneous media must be due to the rigid silane linker used to functionalize the glass bead surfaces for the successive grafting of the (salen)Mn(III) molecules.[23] Noteworthy, it was also observed a better e. e. excess with Mn_MGB than in solution.

Similar epoxidation reactions have been performed with the Mn_MGB using the 1,2-dihydronaphtalene and indene as substrates and Tables 5.1.4 and 5.1.5 show relevant results, respectively.

Table 5.1.4. Results for the epoxidation of 1,2-dihydronapthalene using the Mn_MGB. In all these experiments 0.081 mmol of 1,2-dihydronapthalene were dissolved in 1 mL of CH_2Cl_2; NaClO was 0.81 mmol and the total volume of the reacting solutions, buffered with 1 mL 0.05 M Na_2HPO_4 at pH = 11.2, was 3 mL. [a]determined by GC on a dimethyl-pentyl-beta (DMePeBETACDX) chiral column, (25 m x 0.25 mm ID, 0.25 μm film). [b]TON= mmol of the overall products/mmol of the catalyst. [c] TOF = TON/reaction time (h).

Number of glass bead Catalyst	Reaction Time / h	e. e %[a]	Conv. %[a]	TON[b]	TOF[c] (h^{-1})
10	7	80	23	33108	4730
	24	78	49	61073	2545
	48	80	77	103718	2161
	72	80	100	124043	1723
30	7	81	27	9640	1377
	24	80	55	20664	861
	48	79	84	32209	671
	72	80	100	41969	583
60	7	79	31	6363	909
	24	81	84	17293	721
	48	80	100	20611	429
60 + PPNO	7	80	38	7790	1113
	24	79	93	19222	801
	48	81	100	20611	429

Table 5.1.5. Results for the epoxidation of indene using the Mn_MGB. [a]In all these experiments 0.081 mmol of indene were dissolved in 1 mL of CH_2Cl_2; NaClO was 0.81 mmol and the total volume of the reacting solutions, buffered with 1 mL 0.05 M Na_2HPO_4 at pH = 11.2, was 3 mL. [a]determined by GC on a dimethyl-pentyl-beta (DMePeBETACDX) chiral column, (25 m x 0.25 mm ID, 0.25 μm film). [b]TON = mmol of the overall products/mmol of the catalyst. [c]TOF = TON/reaction time (h).

Number of glass bead Catalyst	Reaction Time / h	e. e %[a]	Conv. %[a]	TON[b]	TOF[c] (h^{-1})
10	7	80	28	34657	4951
	24	78	72	89302	3721
	48	80	100	124043	2584
30	7	78	31	13105	1872
	24	81	88	36976	1541
	48	80	100	41969	874
60	7	75	24	4852	693
	24	78	91	18758	782
	48	78	100	20611	429
60 + PPNO	7	77	29	6067	867
	24	78	97	20004	833

Notably, reaction times for the total conversion of the 1,2-dihydronapthalene and indene are shorter than those observed for the *cis*-β-ethylstyrene and 6-cyano-2,2-dimethylchromene. In fact, the total conversion of the 1,2-dihydronaphtalene was achieved in 72 h, using 10 and 30 spheres, and in 48 h using 60 spheres. Indene was completely converted into the respective epoxides in 48 h using 30 spheres. The observed different reaction times for the total conversion of the above alkenes can find a rationale on the basis of the different geometric structures of the substrates. Both indene and 1,2-dihydronaphtalene have planar structures, while *cis*-β-ethylstyrene and 6-cyano-2,2-dimethylchromene are slightly more bulky, due to the freedom in γ-position in the *cis*-β-ethylstyrene, and the two methyl groups in the 6-cyano-2,2-dimethylchromene. Planar alkenes seem more suited than bulky substrates to interact with the surface confined Mn_MGB catalyst (Figure 5.1.5). In these cases enantiomeric excesses are similar to our data obtained in solution (Table 5.1.1) and similar to recently reported results.[29-31]

An interesting observation is the high present value of the turnover frequencies under heterogeneous conditions (1.24×10^5 using 10 spheres) with respect to the solution (20) after the total olefin transformation.[7,9,30] Obviously, the highest TON values were observed for the lowest number of beads used in the reaction media (Tables 5.1.2-5.1.5). The TOF parameter displays a similar trend on passing from homogeneous (10) to heterogeneous (4951 highest TOF for indene epoxidation after 7

h reaction) conditions.[30] Evidently, these large TOF values (Tables 5.1.2-5.1.5) are due to the covalent nature of the active catalyst that precludes any leaching as measured in the reacting solution by inductively coupled plasma mass spectrometry.

The present increase in enantioselectivity from solution (80 %, Table 5.1.1) to heterogeneous (85-91 %, Tables 3.2-3.3) catalysis observed for the first two alkenes may be consistent with the grafting geometry of this (salen)Mn(III) catalyst that is always appropriate for the epoxidation reaction. It is possible to assume that the $O=Mn^{V}$ group of the $O=Mn^{V}$(salen) points outside from the monolayer.[23,25] A similar conclusion has been arrived at by Milstein who reported on improved TON values in catalytic reactions using molecular ordered Langmuir-Blodgett catalyst films.[31]

Thus, the present study demonstrates the possibility to heterogenize the (salen)Mn(III) catalyst with improving of the performance with respect to the solution reactions. In fact, the enantiomeric excess values are better than those obtained in homogeneous media because of the (salen)Mn(III) catalyst, supported on the present glass beads, probably assumes the most appropriate conformation to promote an efficient enantioselective oxygen transfer towards some substrates.

Conclusions

A novel (salen)Mn(III) robust monolayer was covalently fabricated on glass beads substrates and resulted an active catalyst for the asymmetric epoxidation of four different alkenes. High enantioselectivity and high TON and TOF values were measured. No observable leaching of the catalyst as well as no performance variation was noted after 7 reaction cycles. According to studies of Zhang and Tu the rigid silane group used to graft the present (salen)Mn(III) complex to the glass bead surfaces was advantageous to attain high activity and e.e. values.[32]

Thus, in this chapter it was shown how the heterogenizatn of the (salen)Mn(III) catalyst allows the improving of its performance with respect to the solution reaction, as a consequence of a more appropriate catalyst conformation on the surface of the glass beads.

References

[1] (a) L. Canali and D. C. Sherrington, *Chem. Soc. Rev.*, **1999**, *28*, 85–93; b) C. E. Song and S. G. Lee, *Chem. Rev.*, **2002**, *102*, 3495 – 3524; c) E. M. McGarrigle and D. G. Gilheany, *Chem. Rev.*, **2005**, *105*, 1563 –1602; d) K. Yu, Z. Gu, R. Ji, L. L. Lou, F. Ding, C. Zhang and S. X. Liu, *J. Catal.*, **2007**, *252*, 312– 320; e) R. Luo, R. Tan, Z. Peng, W. Zheng, Y. Kong and D. Yin, *J. Catal.*, **2012**, *287*, 170– 177.

[2] (a) P. McMorn and G. J. Hutchings, *Chem. Soc. Rev.*, **2004**, *33*, 108– 122; (b) C. Li, *Catal. Rev. Sci. Eng.*, **2004**, *46*, 419– 492; c) A. Corma, *Catal. Rev. Sci. Eng.*, **2004**, *46*, 369 –417; d) D. J. Macquarrie, *Top.Catal.*, **2009**, *52*, 1640 –1650.

[3] J. M. Thomas, R. Raja, *Acc.Chem. Res.*, **2008**, *41*, 708-720.

[4] S. Bell, B. Wustenberg, S. Kaiser, F. Menges, T. Netscher, A. Pfaltz, *Science*, **2006**, *311*, 642–644.

[5] M. Wills, *Science*, **2006**, *311*, 619–620.

[6] R. Raja, J. M. Thomas, M. D. Jones, B. F. G. Johnson, D. E. W. Vaughan, *J. Am. Chem. Soc.*, **2003**, *125*, 14982–14983.

[7] C. Bianchini, P. Barbaro, *Topics Catal.*, **2002**, *19*, 17–32.

[8] T. P. Yoon and E. N. Jacobsen, *Science*, **2003**, *299*, 1691-1693.

[9] J. M. Fraile, J. I. García, C. I. Herrerías, J. A. Mayoral, E. Pires, *Chem. Soc. Rev.*, **2009**, *38*, 695–706.

[10] A. Corma, H. Garcia, *Chem. Soc. Rev.*, **2008**, *37*, 2096–2126.

[11] B. M. Rossbach, K. Leopold, R. Weberskirch, *Angew. Chem. Int. Ed.*, **2006**, *45*, 1309-1312.

[12] Gulino, A.; Millesi, S.; Trusso Sfrazzetto, G.; Toscano, R. M.; Ballistreri, F. P; Tomaselli, G. A; Pappalardo, A. *Catalysis Science & Technology*, **2015**, *5*, 673-679.

[13] J. Lisowski, *Inorg. Chem*., **2011**, *50*, 5567-5576.

[14] G. Haberhauer, *Angew. Chem. Int. Ed.*, **2010**, *49*, 9286-9289.

[15] A. Gonzalez-Alvarez, I. Alfonso, J. Cano, P. Diaz, V. Gotor, V. Gotor-Fernandez, E. Garcia-Espana, S. Garcia-Granda, H. R. Jimenez and F. Lloret, *Angew. Chem. Int. Ed.*, **2009**, *48*, 6055-6058.

[16] E.N. Jacobsen, in Catalytic Asymmetric Synthesis, ed. I. Ojima, VCH, Weinheim, 1993, ch. 4.2, pp. 159–202.

[17] K.Matsumoto and T. Katsuki, in Catalytic Asymmetric Synthesis, ed.I. Ojima, J. Wiley & Sons, Inc., New Jersey, 3rd edn, 2010, pp. 839–890.

[18] A. F. Trindade, P. M. P. Gois, C. A. M. Afonso, *Chem. Rev.*, **2009**, *109*, 418–514.

[19] I. W. E. E. Arends, *Angew. Chem. Int. Ed.*, **2006**, *45*, 6250-6252.

[20] D.-Y. Xie, S. B. Sharma, N. L. Paiva, D. Ferreira, R. A. Dixon, *Science*, **2003**, *299*, 396-399.

[21] Q.-H. Xia, H.-Q. Ge, C.-P. Ye, Z.-M. Liu and K.-X. Su, *Chem. Rev.*, **2005**, *105*, 1603-1662.

[22] M. L. Merlau, M. Del Pillar Mejia, S. T. Nguyen and J. T. Hupp, Angew. Chem. Int., **2001**, 40, 4239-4242.

[23] H. Zhang, Y. Zou, Y.-M. Wang, Y. Shen, X. Zheng, *Chem. Eur. J.*, **2014**, *20*, 1 – 13.

[24] (a) F. Cozzi, *Adv. Synth. Catal.*, **2006**, *348*, 1367 –1390; b) C. Li, H. D. Zhang, D. M. Jiang, Q. H. Yang, *Chem. Commun.*, **2007**, 547–558; c) J. M. Thomas, R. Raja, D. W. Lewis, *Angew. Chem.*, **2005**, *117*, 6614 –6641; J. M. Thomas, R. Raja, D. W. Lewis, *Angew. Chem. Int. Ed.*, **2005**, *44*, 6456 –6482.

[25] V. La Paglia Fragola, F. Lupo, A. Pappalardo, G. Trusso Sfrazzetto, R. M. Toscano, F. P. Ballistreri, G. A. Tomaselli, A. Gulino, *J. Mater. Chem.*, **2012**, *22*, 20561-20565.

[26] D. Q. Li, B. I. Swanson, J. M. Robinson, M. A. Hoffbauer, *J. Am. Chem. Soc.*, **1993**, *115*, 6975-6980.

[27] I. Bar-Nahum, H. Cohen, R. Neumann, *Inorg. Chem.*, **2003**, *42*, 3677-3684.

[28] D. A. Cristaldi, A. Motta, S. Millesi, T. Gupta, M. Chhatwalb, A. Gulino, *J. Mater. Chem. C.*, **2013**, *1*, 4979-4984.

[29] D. Feichtinger, D. A. Plattner, *Angew. Chem. Int. Ed.*, **1997**, *36*, 1718-1719.

[30] R. L. Paddock, S. T. Nguyen, *J. Am. Chem. Soc.*, **2001**, *123*, 11498-11499.

[31] K. Töllner, R. Popovitz-Biro, M. Lahav, D. Milstein, *Science*, **1997**, *278*, 2100-2102.

[32] X. B. Tu, X. K. Fu, X. Y. Hu, Y. D. Li, *Inorg. Chem. Commun*., **2010**, *13*, 404– 407.

Conclusions and Perspectives

The aim of this PhD thesis was the fabrication of nanostructures showing optical, electrical or catalytic properties in the perspective of their applications in different fields of the nanotechnology.

All the systems result from a *bottom-up* approach that involves the self-assembly of appropriate molecules on inorganic surfaces. In all synthesized systems the coupling agent is represented by a silane layer that allowed fabricating covalent nanostructures maintaining single-molecule properties and showing homogeneous surfaces.

In fact, this method allowed obtaining robust porphyrin nanostructures on Si(100) with a such high order degree for their integration in microelectronic devices.

Porphyrin monolayers on flat and transparent substrates proved to be useful for chemical communication with external inputs thus giving readable optical outputs valuable for memory storage materials.

Furthermore, we obtained tin and titanium oxide crystal grains covered with a porphyrin monolayer. These systems show an enhanced electron injection property and can be of great utility in the photovoltaic field.

Interesting optical properties have also been observed for an Europium(III) complex self-assembled on polystyrene nanostructures or on a porphyrin monolayer. In the last case the unique optical properties resulted from a mutual Eu-complex_porphyrin interaction.

A really advantage of the covalent assembly is represented by the robustness of the obtained nanostructures and, sometimes, unicity of their properties. As an example, the catalytic properties of the (salen)Mn(III) complex monolayer resulted in huge turnover numbers for epoxidation of unfunctionalised prochiral olefin reactions.

We demonstrated that single-molecules properties are affected by the substrate nature. Therefore we plane to fabricate nanostructures on our CdO thin films. In fact,

the coupling of molecular optical properties with highly conducting and transparent substrates will produce systems useful for optoelectronics.

In summary a major goal of this thesis was the combination of molecule-inorganic substrate properties. Thus the covalent bond of suitable molecules on appropriate inorganic surfaces allows the synthesis of molecular architectures showing unique properties appealing for future optoelectronic, microelectronic and catalysis technologies.

Appendix

X-Ray Photoelectron Spectroscopy

X-ray photoelectron spectroscopy (XPS) is a widely used technique to investigate the chemical composition of surfaces. It was developed in the mid-1960's by Kai Siegbahn and his research group at the University of Uppsala, Sweden. The XPS technique is used to measure:

- elemental composition of surfaces (top 0–10 nm usually)
- empirical formula of pure materials
- chemical or electronic state of each element in the surface
- uniformity of elemental composition across the surface (or line profiling or mapping)
- uniformity of elemental composition as a function of ion beam etching (or depth profiling)

The phenomenon is based on the photoelectric effect, outlined by Einstein in 1905, where the concept of the photon was used to describe the ejection of electrons from a surface when photons impinge upon it (Figure 1).

$$A + h\nu \rightarrow A^{+} + e^{-}$$

Irradiation causes the emission of photoelectrons whose energy is proportional to the incident radiation frequency, while their number is proportional to the radiation intensity.

A typical XPS instrument has an analysis chamber kept at ultra-high vacuum, ca. 10^{-8} Pa and the X-ray sources typically used are Al (1486.6 eV) or Mg (1253.6 eV) Kα radiations that induce the emission of electrons from the inner energetic levels (core electrons) of each element present on the surface of the analysed material.

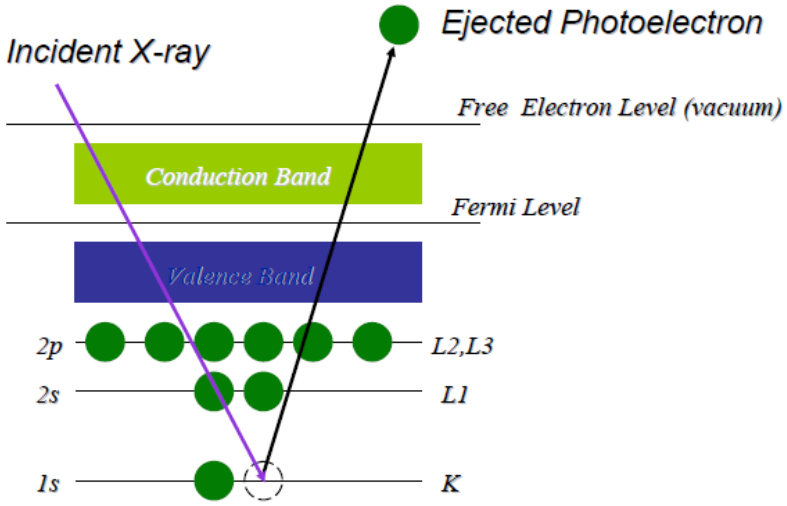

Figure 1. Scheme of the photoemission process.

The vacuum is essential to maximize the path of the electrons out of the material, without collision with other gaseous substances present in the chamber, allowing thus they reach the detector. Moreover, it reduces the probability of finding contaminants absorbed on the surface of the sample, such as water and oxygen. X-ray photoelectron spectra are thus collected by measuring the kinetic energy and number of electrons that escape from a few tens of angstroms of the surface.

In detail, when X-rays illuminate an area of a sample cause ejection of electrons with a range of energies and directions. The electron optics, which may be a set of electrostatic and/or magnetic lens units, collect a proportion of these emitted electrons defined by those rays that can be transferred through the apertures and focused onto the analyser entrance slit. Electrostatic fields within the hemispherical analyser (HSA) are established to only allow electrons of a given energy (the so called Pass Energy PE) to arrive at the detector slits and onto the detectors themselves. Electrons of a specific initial kinetic energy are measured by setting voltages for the lens system that both focus onto the entrance slit the electrons of the required initial energy and retards their velocity so that their kinetic energy after passing through the transfer lenses matches the pass energy of the hemispherical analyser. To record a spectrum over a

range of initial excitation energies it is necessary to scan the voltages applied to these transfer lenses and the prescription for these lens voltages is known as the set of lens functions. These lens functions are typically stored in some configuration file used by the acquisition system. Thus, known the energy of the incident beam and the kinetic energy of the families of ejected photoelectrons, it is possible to measure the Binding Energy value (B.E.) using the following equation:

$$E_K = h\nu - B.E. - W$$

where:

-hν: energy of the incident photon;

-E_k: kinetic energy of the ejected electron;

-B.E.: binding energy of the ejected electron;

-W: work function depending on both the spectrometer and the material.

According to Koopman's theorem, the measured B.E. corresponds to the energy difference between the initial state of an atom with "n" electrons and the final state with "n-1" electrons:

$$B.E. = E_{final}\,(n-1) - E_{initial}\,(n)$$

This is true only if the "frozen orbit" hypothesis (frozen or sudden approximation), is valid (no relaxation phenomenon after photoemission). In fact according to this theorem it is believed that the atomic orbitals remain unchanged upon the ionization. However, it is easy to understand that as a result of ionization there is an electronic rearrangement, whereby the B.E. will be calculated differently. Moreover, being different the number of electrons of the ion compared to the neutral atom also the correlation energy will certainly be different.

To identify the chemical species present in a sample it should be first performed an analysis at low resolution or "survey", encompassing a wide range of energies (generally from 1200 eV to 0 eV).

For each element of the periodic table many characteristic peaks at different B.E. values can be obtained, depending on the orbital from which the electron is ejected.

Therefore, the different atomic species can be identified by their B.E. which depend on the oxidation state and chemical environment of the analysed atom (*chemical shift*). In fact, with the decrease of the number of outer electrons, the core electrons experience a greater nuclear charge and thus it will take a greater energy to remove them away from their levels. A similar effect is observed when an atom is bound to a more electronegative one.

Furthermore electrons from p, d or f orbitals give two signals (due to the coupling between the spin angular momentum (s) and the orbital angular momentum (l)) with separation energy characteristic of the atom (*spin-orbit coupling*), while the intensity ratio between the respective areas of the peaks remains the same for all atomic species, differing only as a function of the type of orbital from which the peaks arise. For the identification of the elements it can thus be exploited also their spin-orbit separation.

In a second step it is possible to acquire a more detailed or "multiplex" spectrum by setting a finer resolution and scanning over only the energy regions of interest.

In addition, it should be outlined that the XPS is a technique for the study of surfaces since the thickness from which the signals arise typically ranges from 0 to 100 Å, although the X-radiation penetrates into the solid for about 10^4 Å. This means that the depth of X-ray beam penetration is not decisive for the technique sensitivity. In fact, XPS sensitivity depends on the probability of the generated photoelectrons to leave the surface. In fact the electrons ejected from core orbitals in the ionization process can be subjected to impact (inelastic scattering) within the solid, which determines an energy loss not allowing these to reach the surface and be expelled. Therefore the sampling depth from which the 95% of the emitted electrons originate is defined as:

$$d = 3\lambda \cdot \text{sen}\theta$$

where:

-λ: electron mean free path within the solid (about 30 Å);

-θ: take-off angle between the sample surface and the analyser direction;

It results evident that the higher the take-off angle the higher the sampling depth.

Interestingly, to carry out structural and electronic characterization of self-assembled molecular nanoarchitectures or films too thin to be analysed by conventional depth profiling techniques, is useful the Angle Resolved XPS (AR-XPS). AR-XPS measurements provide information about ordering and thickness of layers, distribution of elements and chemical states within the film or nanostructure (depth profile reconstruction).

In the context of nanostructured systems based on organic or inorganic molecules covalently assembled on inorganic substrates (Si(100) or SiO_2) the AR-XPS is used to measure the thickness of the molecular monolayer bound to the substrate. In detail, AR-XP spectra are measured at different take-off angles (for example, 5°, 15°, 45° and 80°) and the angular dependence of the I_C/I_{Si} intensity ratios (I_C and I_{Si} are the total intensities of carbon and silicon, respectively) vs. the photoelectron take-off angle is plotted. The I_C/I_{Si} intensity ratio is modelled as follows:

$$\frac{I^C}{I^{Si}} = \frac{I_\infty^C (1 - e^{\frac{-d}{\lambda_{C1s}^C sen\theta}})}{I_\infty^{Si} e^{\frac{-d}{\lambda_{Si2p}^C sen\theta}}}$$

where:

- $\lambda^C_{Si\ 2p}$: mean free path of Si 2p photoelectrons;
- λ^C_{C1s}: mean free path of C 1s photoelectrons in a carbon overlayer;
- $I^C\infty/I^{Si}\infty$: ratio of Wagner sensitivity factors.

By using this equation the thickness *d* is obtained.

Finally, with XPS technique it is possible to perform quantitative analyses. In particular the XPS peak intensity I(εi) is correlated to the number of emitted photoelectrons and depends on several factors:

$$I(\varepsilon_i) = I_0 \cdot \eta_i \cdot \sigma(\varepsilon_i) \cdot \lambda(\varepsilon_i) \cdot D(\varepsilon_i)$$

-I_0: X-ray flux intensity;

- ηi: atomic density of the i element;

-σ (εi): cross section for the photoelectron extraction;

-λ (εi): mean free path of photoelectrons in the sample;

-D (εi): detector and analyser efficiency.

From the intensities of the peaks it is possible to obtain the atomic concentrations in the sample studied by means of the formula:

$$C_x = \frac{\eta_x}{\Sigma \eta_i} = \frac{I_x}{S_x} \times \frac{1}{\Sigma \frac{I_i}{S_i}}$$

where:

-η: atomic density of the element per volume unit (cm^3);

-S: atomic sensitivity factor;

-I: peak intensity.

Before using the intensities of the peaks for the quantitative analysis it is necessary the removal of the bottom (background) determined from all those photoelectrons that lose energy before reaching the detector. Methods to be used for this correction are:

-Linear subtraction;

-Shirley;

-Tougaard.

The main components of an XP spectrometer system include a source of X-rays, an ultra-high vacuum (UHV) stainless steel chamber with UHV pumps, an electron energy analyser, an electron detector system, a moderate vacuum sample introduction chamber, sample mounts, a sample stage and a set of stage manipulators (Figure 2).

Source: X-ray tube consisting of a tungsten cathode and a copper anode coated by aluminium on a face and magnesium on the other face. These materials are chosen for two reasons:

- energy of the X-ray beam sufficiently high to allow the excitation of the core electrons;

-Full Width at Half Height (FWHM) of the peak usually between 0.7-0.8 eV, since the resolution of the instrument is inversely proportional to the bandwidth of the

incident beam. The electrons produced at the cathode by thermionic effect are accelerated by a potential of 15 keV and directed towards the anode: as a result of this collision X photons will be emitted.

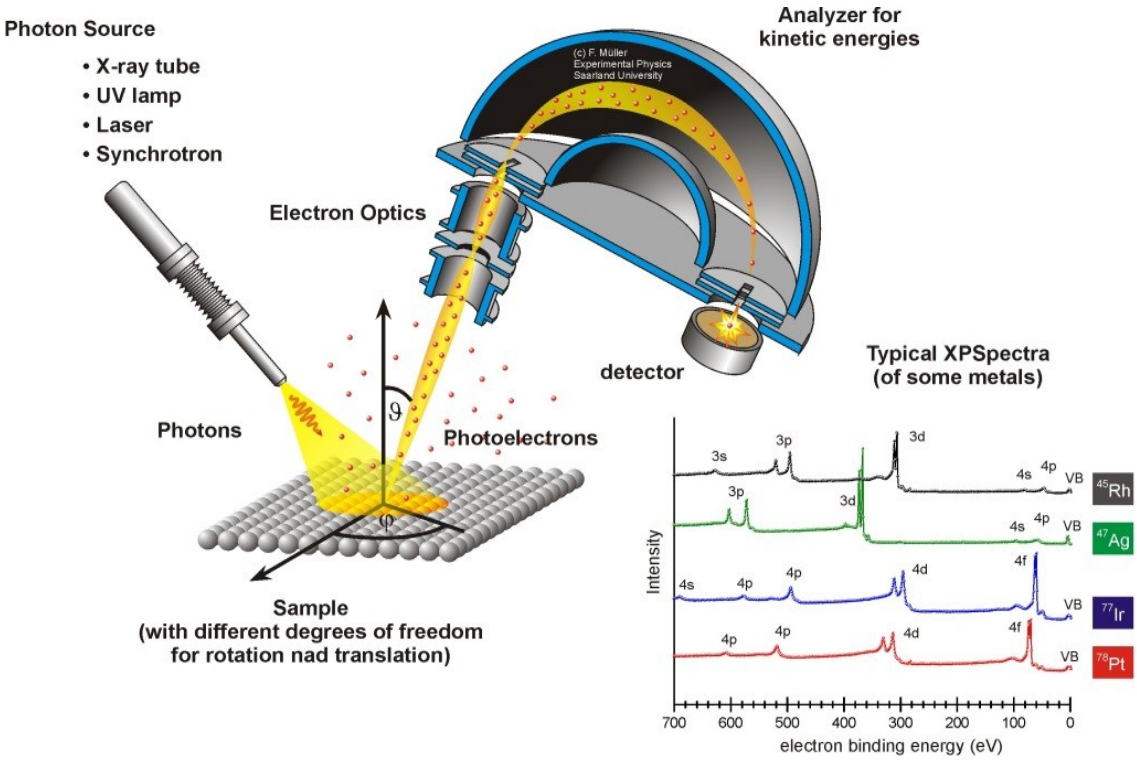

Figure 2. Main components of an XP spectrometer and XP spectra typical of some elements.

Analyser: consisting of two concentric metal hemispheres (electrostatic plates) between which a ddp is applied. As a function of the potential applied to the grid of entrance (Pass Energy) electrons will be deflected in a different way according to their kinetic energy and only those having the desired E_k will arrive at the detector.

Vacuum System: allows obtaining UHV conditions by means of a turbomolecular pump and an ionic pump. Moreover, the system is also equipped with a titanium sublimation pump.

The instrument used to perform XPS measurements is PHI 5600 Multi Technique System which gives good control of the electron take-off angle (base pressure of the main chamber 3 x 10^{-10} Torr).[1-2] The spectra were excited with monochromatized Al-

Kα or Mg-Kα radiation. XPS peak intensities were obtained after Shirley background removal.[3] Spectra calibration was achieved by fixing the main C 1s peak at 285.0 eV. Experimental uncertainties in binding energy (B.E.) are ≤ 0.4 eV. The experimental profiles were fitted with symmetrical Gaussian peaks after subtraction of the background. This process involves data refinement, based on the method of the least squares fitting, carried out until there was the highest possible correlation between the experimental spectrum and the theoretical profile. The R-factor (residual or agreement factor), $R = [\Sigma(F_o - F_c)^2/\Sigma(F_o)^2]^{1/2}$, after minimization of the function $\Sigma(F_o - F_c)^2$ converged to R values ≤ 0.030 – 0.035.

By taking into account all the advantageous aspects of the X-ray photoelectron spectroscopy it is fair to say that it is an important technique for an in-depth chemical and structural characterization of nanoscopic systems. In fact, it is suitable for probing thicknesses and immediately obtaining qualitative and quantitative data, film thickness, surface coverage,[4] molecule footprint, oxidation states, and presence of functional groups. [5]

References

[1] Briggs D, Grant JT (2003) Surface analysis by Auger and X-ray photoelectron spectroscopy. IMP, Chichester

[2] Cattaruzza, F.; Llanes-Pallas, A.; Marrani, A. G.; Dalchiele, E. A.; Decker, F.; Zanoni, R.; Prato, M.; Bonifazi, D. *J. Mater. Chem*. **2008**, 18, 1570.

[3] Repoux, M. *Surf. Interface Anal.* **1992**, 18, 567.

[4] Killampalli AS, Ma PF, Engstrom JR. *J Am Chem Soc.* **2005**, *2*,6300–6310.

[5] A. Gulino, *Anal Bioanal Chem*.**2013,** 405,1479–1495.

List of Publications of Salvatrice Millesi

11) **S. Millesi**, R. Lo Nigro, M. Pedroni, A. Speghini, A. Gulino
Photoexcited Self-Assembled Porphyrins Functionalizing TiO_2 and SnO_2 Nanocrystals.
J. Phys. Chem. C, **2015**, *119*, 23743-23751.

10) D. A. Cristaldi, **S. Millesi**, P. Mineo, A. Gulino.
A Chemical Address for the Morse Code.
J. Lumin., **2016**, *169,*348-352.

9) **S. Millesi**, M. Schilirò, F. Greco, I. Crupi, G. Impellizzeri, F. Priolo, R.G. Egdell, A. Gulino
Nanostructured CdO Thin Films for Water Treatments.
Materials Science in Semiconductor Processing, In Press.
DOI: 10.1016/j.mssp.**2015**.08.005.

8) **S. Millesi**, G. Maccarrone, A. Gulino
Solid Nanoarchitecture – Solution: Dynamics of the Chemical Communication.
Physical Chemistry Chemical Physics, **2015**,*17*,6612-6617.

7) K. Barbera, P. Lanzafame, D. Montalto, A. Pistone, **S. Millesi**, G. Malandrino, A. Gulino, S. Perathoner, G. Centi
How the acidic sites localization induces unconventional diffusion effects in sulphated ZrO_2-SBA-15 catalysts.
Journal of Catalysis, **2015**, 323, 19-32.

6) F. Pappalardo, D. A. Cristaldi, I. L. Fragalà, **S. Millesi**, M. De Bonis, A. Gulino
Spectroscopic and Morphological Characterization of Inflow Cannulas of Left Ventricular Assist Devices.
ASAIO Journal, **2015**,*61*,150-155.

5) G. Trusso Sfrazzetto, **S. Millesi**, A. Pappalardo, R. M. Toscano, F. P. Ballistreri, G. A. Tomaselli and A. Gulino.

Olefin epoxidation by a (salen)Mn(III) catalyst covalently grafted on glass beads.
Catal. Sci. Technol,. **2015**, *5*, 673-679.

4) D. A. Cristaldi, **S. Millesi**, I. Crupi, G. Impellizzeri, F. Priolo, R. M. J. Jacobs, R. G. Egdell, A.Gulino.
Structural, Electronic and Electrical Properties of an Undoped n-Type CdO Thin Film with High Electron Concentration.
J. Phys. Chem. C, **2014**, *118*, 15019-15026.

3) **S. Millesi**, A. Gulino.
Optical Logics by means of Porphyrin-Eu-b-Diketonate Supramolecular Nanostructures.
J. Mater. Chem. C, **2014**, *2*, 5924-5930.

2) D. A. Cristaldi, **S. Millesi**, P. Mineo, A. Gulino.
Europium Complex Covalently Grafted on Si(100) Surfaces, Engineered with Covalent Polystyrene Nanostructures.
J. Phys. Chem. C, **2013**, *117*, 16213−16220.

1) D. A. Cristaldi, A. Motta, **S. Millesi**, T. Gupta, M. Chhatwalb, A. Gulino
Long Range Order in Si(100) Surfaces Engineered with Porphyrin Nanostructures.
J. Mater. Chem. C, **2013**, *1*, 4979-4984.

List of Communications of Salvatrice Millesi

5) **S. Millesi**, A. Gulino, , S. Pappalardo, C. Capici, G. Gattuso, A. Notti, M.F. Parisi
Selective Sensing of Alkaline Cations by Calixarene Monolayers
13th International Conference on Calixarenes (Calix 2015)
Giardini Naxos, Italia, 5-9 Luglio **2015**.

4) **S. Millesi**, I. Crupi,b G. Impellizzeri, F. Priolo, R. M. J. Jacobs, R. G. Egdell, A. Gulino
Electronic and Electrical Properties of CdO Thin Films
E-MRS Spring Meeting,
Lille, France, 11 -15 Maggio **2015**.

3) **S. Millesi**, G. Condorelli, A. Gulino
X-Ray Photoelectron Spectroscopy of Nanostructures
E-MRS Spring Meeting,
Lille, France, 26 -30 Maggio **2014**.

2) **S. Millesi**, A. Cristaldi, A. Gulino
Molecular recognition of biological systems using calixarene monolayers
IX convegno nazionale INSTM sulla scienza e tecnologia dei materiali,
Bari, 30 Giugno-3 Luglio **2013**, P059.

1) D.A. Cristaldi, **S. Millesi**, I.L. Fragalà, A. Gulino
Covalent Polymer Chains on Siloxane-Functionalised Si Substrate
IX convegno nazionale INSTM sulla scienza e tecnologia dei materiali,
Bari, 30 Giugno-3 Luglio **2013**, P025.

Acknowledgements

Ringrazio il mio tutor, il Professore Antonino Gulino, per avermi accolta come se fossi una persona di famiglia, facendomi sentire a casa. Grazie a lui ho imparato tantissimo professionalmene e umanamanente. Ho vissuto una bellissima esperienza.

Un ringraziamento va al Dr. Andrea Cristaldi che mi è stato di fondamentale aiuto durante il mio primo anno di dottorato.

Ho, inoltre, conosciuto degli splendidi compagni di viaggio, dai professori, ai colleghi per finire coi tesisti Matteo, Francesco e Luca.

Ringrazio i miei suoceri Maria e Santo che mi hanno sempre dato un po' del loro tempo quando ne ho avuto bisogno, i miei cognati Lidia ed Enzo e i miei adorati nipotini Ginevra e Mario.

Ringrazio le mie amiche Carolina, Fabiola, Valentina e Giusy per essere "le amiche di sempre che non mi abbandonano mai".

Ringrazio Katia per essere sempre presente e premurosa.

Ringrazio mamma Rosa e papà Salvo per aver sempre sopportato i miei sfoghi nei momenti meno facili e per avermi dato la possibilità di arrivare oggi fino a questo punto.

Ringrazio il Signore per avermi dato la fortuna di ritrovare una meritata serenità con mio fratello Giuseppe, mia cognata Ivana e le loro due principesse Giulia e Aurora.

Ringrazio i miei nonni Antonino e Piera che sin dai tempi della scuola sono i miei più fedeli sostenitori.

Ringrazio con affetto e nostalgia i cari nonni Giuseppe e Salvatrice il cui ricordo è costante nel mio cuore.

Ringrazio mio marito Niki, che in questi tre anni mi è stato vicino supportandomi nei momenti più difficili, suggerendomi di non perdere mai la fiducia in me stessa "perché sono importante".

Ringrazio il mio successo più grande, la mia piccola Anita, che ogni giorno mi fa provare emozioni che non credevo possibili dandomi la forza di affrontare con coraggio le difficoltà, e facendomi sentire meno il peso dei sacrifici che nella vita quotidiana si fanno.